NAVAL POSTGRADUATE SCHOOL

MONTEREY, CALIFORNIA

THESIS

VARIABILITY IN HURRICANE BOUNDARY LAYER CHARACTERISTICS OBSERVED IN A LONG-TERM NOAA DROPSONDE ARCHIVE

by

Robert D. T. Wendt

June 2014

Thesis Advisor:	Patrick Harr
Co-Advisor:	Qing Wang

Approved for public release; distribution is unlimited

REPORT DOCUMENTATION PAGE	*Form Approved OMB No. 0704-0188*

1. AGENCY USE ONLY *(Leave blank)*	**2. REPORT DATE** June 2014	**3. REPORT TYPE AND DATES COVERED** Master's Thesis

4. TITLE AND SUBTITLE VARIABILITY IN HURRICANE BOUNDARY LAYER CHARACTERISTICS OBSERVED IN A LONG-TERM NOAA DROPSONDE ARCHIVE	**5. FUNDING NUMBERS**
6. AUTHOR(S) Robert D. T. Wendt	
7. PERFORMING ORGANIZATION NAME(S) AND ADDRESS(ES) Naval Postgraduate School Monterey, CA 93943-5000	**8. PERFORMING ORGANIZATION REPORT NUMBER**
9. SPONSORING /MONITORING AGENCY NAME(S) AND ADDRESS(ES) N/A	**10. SPONSORING/MONITORING AGENCY REPORT NUMBER**

11. SUPPLEMENTARY NOTES The views expressed in this thesis are those of the author and do not reflect the official policy or position of the Department of Defense or the U.S. Government. IRB Protocol number ____N/A____.

12a. DISTRIBUTION / AVAILABILITY STATEMENT Approved for public release; distribution is unlimited	**12b. DISTRIBUTION CODE** A

13. ABSTRACT (maximum 200 words)

The statistical properties of five boundary layer height definitions were examined in 6,593 NCAR GPS dropsonde observations of the hurricane environment. Based on similar composite analysis studies, these boundary layer height estimates were divided into two categories based on their analytical characteristics. Three dynamical methods of estimating the boundary layer height were combined with two thermodynamical methods of estimating the mixed layer depth to numerically interrogate the physical properties of hurricanes within two primary modes of variability: azimuthal and geographic region.

The results confirmed the vertical bifurcation of dynamical and thermodynamical height estimates and indicated a consistent distinction in the radial variability of each class. Moreover, the tangential wind field was well-described by the modified Rankine vortex. A characteristic decrease in boundary layer height with decreasing radius to the storm center was expressed in four of the five definitions. The non-uniform azimuthal distribution of relative radial winds and ill-behaved inflow layer depths precluded meaningful comparisons of boundary layer height in the rear storm-relative semicircle. While boundary layer height estimates failed to exhibit any significant regional variability, the right-front storm-relative quadrant appeared to exhibit non-trivial increases in mean boundary layer height.

14. SUBJECT TERMS Tropical Cyclone, Hurricane Boundary Layer, Boundary Layer Height, Long-Term NOAA Dropsonde Hurricane Archive, Revised Atlantic Hurricane Database, Composite Analysis Technique	**15. NUMBER OF PAGES** 97
	16. PRICE CODE

17. SECURITY CLASSIFICATION OF REPORT Unclassified	**18. SECURITY CLASSIFICATION OF THIS PAGE** Unclassified	**19. SECURITY CLASSIFICATION OF ABSTRACT** Unclassified	**20. LIMITATION OF ABSTRACT** UU

NSN 7540-01-280-5500

Standard Form 298 (Rev. 2-89)
Prescribed by ANSI Std. 239-18

THIS PAGE INTENTIONALLY LEFT BLANK

VARIABILITY IN HURRICANE BOUNDARY LAYER CHARACTERISTICS OBSERVED IN A LONG-TERM NOAA DROPSONDE ARCHIVE

Robert D. T. Wendt
Lieutenant, United States Navy
B.S., University of Illinois at Urbana-Champaign, 2003
M.S., University of Illinois at Urbana-Champaign, 2005

Submitted in partial fulfillment of the
requirements for the degree of

MASTER OF SCIENCE IN METEOROLOGY AND PHYSICAL OCEANOGRAPHY

from the

NAVAL POSTGRADUATE SCHOOL
June 2014

Author: Robert D. T. Wendt

Approved by: Patrick Harr
Thesis Advisor

Qing Wang
Co-Advisor

Wendell Nuss
Chair, Department of Meteorology

THIS PAGE INTENTIONALLY LEFT BLANK

ABSTRACT

The statistical properties of five boundary layer height definitions were examined in 6,593 NCAR GPS dropsonde observations of the hurricane environment. Based on similar composite analysis studies, these boundary layer height estimates were divided into two categories based on their analytical characteristics. Three dynamical methods of estimating the boundary layer height were combined with two thermodynamical methods of estimating the mixed layer depth to numerically interrogate the physical properties of hurricanes within two primary modes of variability: azimuthal and geographic region.

The results confirmed the vertical bifurcation of dynamical and thermodynamical height estimates and indicated a consistent distinction in the radial variability of each class. Moreover, the tangential wind field was well-described by the modified Rankine vortex. A characteristic decrease in boundary layer height with decreasing radius to the storm center was expressed in four of the five definitions. The non-uniform azimuthal distribution of relative radial winds and ill-behaved inflow layer depths precluded meaningful comparisons of boundary layer height in the rear storm-relative semicircle. While boundary layer height estimates failed to exhibit any significant regional variability, the right-front storm-relative quadrant appeared to exhibit non-trivial increases in mean boundary layer height.

THIS PAGE INTENTIONALLY LEFT BLANK

TABLE OF CONTENTS

THIS PAGE INTENTIONALLY LEFT BLANK

LIST OF FIGURES

THIS PAGE INTENTIONALLY LEFT BLANK

LIST OF TABLES

THIS PAGE INTENTIONALLY LEFT BLANK

LIST OF ACRONYMS AND ABBREVIATIONS

ABL	atmospheric boundary layer
ATCF	Automated Tropical Cyclone Forecasting system
AVAPS	Airborne Vertical Atmospheric Profiling System
AXBT	airborne expendable bathythermograph
CAPE	convective available potential energy
CRB	Caribbean Sea region
DOD	Department of Defense
ECN	East Coast North region
ECS	East Coast South region
EOL	Earth Observing Laboratory
EPAC	Eastern Pacific Ocean region
GOM	Gulf of Mexico region
GPS	global positioning system
HRD	Hurricane Research Division
IQR	interquartile range
MAE	mean absolute error
MDR	Main Development Region
NOAA	National Oceanographic and Atmospheric Administration
NSF	National Science Foundation
NWP	numerical weather prediction
NHC	National Hurricane Center
PBL	planetary boundary layer
RMSE	root-mean-square error
RMW	radius of maximum winds
SEM	standard error of the mean
SSHS	Saffir-Simpson hurricane scale
STL	Subtropical Atlantic Ocean region
TKE	turbulent kinetic energy
UTC	coordinated universal time
WISHE	wind-induced surface heat exchange

THIS PAGE INTENTIONALLY LEFT BLANK

ACKNOWLEDGMENTS

I am tremendously grateful for all of the support I received in completing this research. I owe much to the distributed efforts of those who have gone before me and, in no small measure, to the community of like-minded individuals in search of a deeper understanding of nature.

To this end, I would like to thank my thesis advisor, Dr. Patrick Harr, for his innumerable contributions to my work. Distilling balanced portions of practical and theoretical guidance, his inexhaustible patience and robust understanding of tropical cyclones were instrumental to the successful execution of this study. I would also like to thank my co-advisor, Dr. Qing Wang, for sharing her knowledge of the planetary boundary layer; in this regard, as with her kindness, generosity, and skill in the classroom, she is virtually without peer.

Similarly, I would like to thank LCDR Dave Roberts (Ret.) for his sustained commitment to my education in tropical cyclone forecasting. Moreover, I would like to thank CDR Elizabeth Sanabia for the rare opportunity to sample the hurricane environment with the 53rd Weather Reconnaissance Squadron. I would also like to thank Louie Beuschlein for introducing me to the ineffable beauty of science and mathematics all those years ago.

To my friends and fellow naval officers, for all of their support and encouragement, on calm days or in rough seas, I offer a sincere word of thanks. I will treasure our fellowship forever.

Finally, I would like to thank my family for their unique and irreplaceable roles in my life and work. To Emily, Cordelia, Eleanor, and Alfred: you mean everything to me. To Cheryl, Dale, and Carol: you have nurtured my hopes and dreams from the very beginning. I am truly fortunate to have all of you in my life.

I. INTRODUCTION

A. MOTIVATION

Tropical cyclones are a powerful demonstration of the laws of nature. Representing an impressive mechanical departure from the quiescent normal modes of the tropical atmosphere, where subsidence warming and trade inversions lead to the vertical bifurcation of convection and moisture in the troposphere, tropical cyclones are ephemeral heat engines of environmental change. While often comprised of mesoscale convective elements, they operate on time and length scales that are distinct from most structures in the mesoscale atmosphere. In this way, tropical cyclones are an important component in the tropical weather system. However, they also provide an important mechanism for the meridional transport of energy from the thermal equator to the geographic poles (Emanuel 2001). As a result, tropical cyclones play a non-trivial role in the energy balance of the coupled ocean-atmosphere system and, by extension, the planet.

In his introductory paper on the steady-state maintenance of tropical cyclones, Emanuel (1986, henceforth E86) utilized an idealized conceptual model of the hurricane boundary layer to reinforce the importance of heat and moisture fluxes at the air-sea interface. Based on the earlier work of Riehl (1954) and Ooyama (1969), E86 hypothesized that the temporal endurance of an arbitrary tropical cyclone was uniquely dependent upon “anomalous fluxes of moist enthalpy from the sea surface with virtually no contribution from preexisting CAPE” (E86). To this end, E86 modeled the hurricane boundary layer environment with an atmospheric slab of uniform density and depth throughout an axisymmetric vortex.

Subsequent research (e.g., Smith et al. 2008; Smith et al. 2009; Bryan and Rotunno 2009) examined the validity of various assumptions in the E86 analytical model, and that of Emanuel’s attendant potential intensity theory, including gradient wind balance within the hurricane boundary layer environment, axisymmetric vortex intensification vis-à-vis wind-induced surface heat exchange (WISHE), and uniform boundary layer height. The latter consideration is particularly important to the physical processes that govern the spatial distribution of enthalpy, moisture, and momentum within a tropical cyclone (Zhang et al. 2011, henceforth Z11).

In this sense, the height of the hurricane boundary layer has become a focal point in hurricane research. Recent efforts (e.g., Smith and Montgomery 2010, henceforth S10; Z11) have examined various dynamical and thermodynamical definitions of boundary layer height and their relevance to prevailing theories of tropical cyclone development and steady-state maintenance. Moreover, these studies draw upon corresponding research (e.g., Nolan et al. 2009a,b; Smith and Thomsen 2009; Kepert 2010) to emphasize the importance of the boundary layer height in numerical simulations of tropical cyclone intensification. When convolved with a lack of consensus on an optimal definition for boundary layer height, these considerations support the need for additional investigations into the characteristics of the hurricane boundary layer (Z11).

While Z11 was both thorough and insightful, it emphasized the relative characteristics of competing definitions of boundary layer height in the context of storm intensity. In simple terms, the study was conditioned in such a way that no azimuthal or regional variability in boundary layer heights were expressed. Furthermore, Z11 utilized a comparatively limited number of dropsondes (i.e., 794 discrete observations); for contrast, a larger dataset, capturing a broader spatial and temporal sample of the North Atlantic hurricane environment, could provide a more robust composite analysis of the hurricane boundary layer. To this end, research attempting to quantify additional modes of boundary layer variability, with data conditioned within a more extensive dropsonde archive, could provide a meaningful extension of the Z11 study. More specifically, it might contribute to the identification of ideal boundary layer height definitions, optimal parameterization schemes, or, perhaps more importantly, enhance the skill of tropical cyclone intensity predictions.

B. OBJECTIVE

As a direct extension of the Z11 investigation, this observational study examines competing dynamical and thermodynamical definitions of boundary layer height within the statistical framework of composite analysis. Utilizing a well-populated hurricane dropsonde archive, it attempts to more fully characterize the hurricane boundary layer environment. Moreover, this research emphasizes changes in hurricane boundary layer structure conditioned by two primary modes of tropical cyclone variability: azimuthal and regional. In this way, the goals of this study were framed within the context of two principle research hypotheses.

The first hypothesis claims that regional variations in the coupled ocean-atmosphere systems of North Atlantic basins produce fundamental differences in the boundary layer structures of corresponding hurricanes. In particular, dropsonde data conditioned by geographic location will yield meaningful comparisons in the radial variability of boundary layer heights between six sub-regions (Figure 1): the Main Development Region (MDR), Caribbean Sea (CRB) region, Gulf of Mexico (GOM) region, East Coast North (ECN) region, East Coast South (ESC) region, and Subtropical North Atlantic (STL) region.

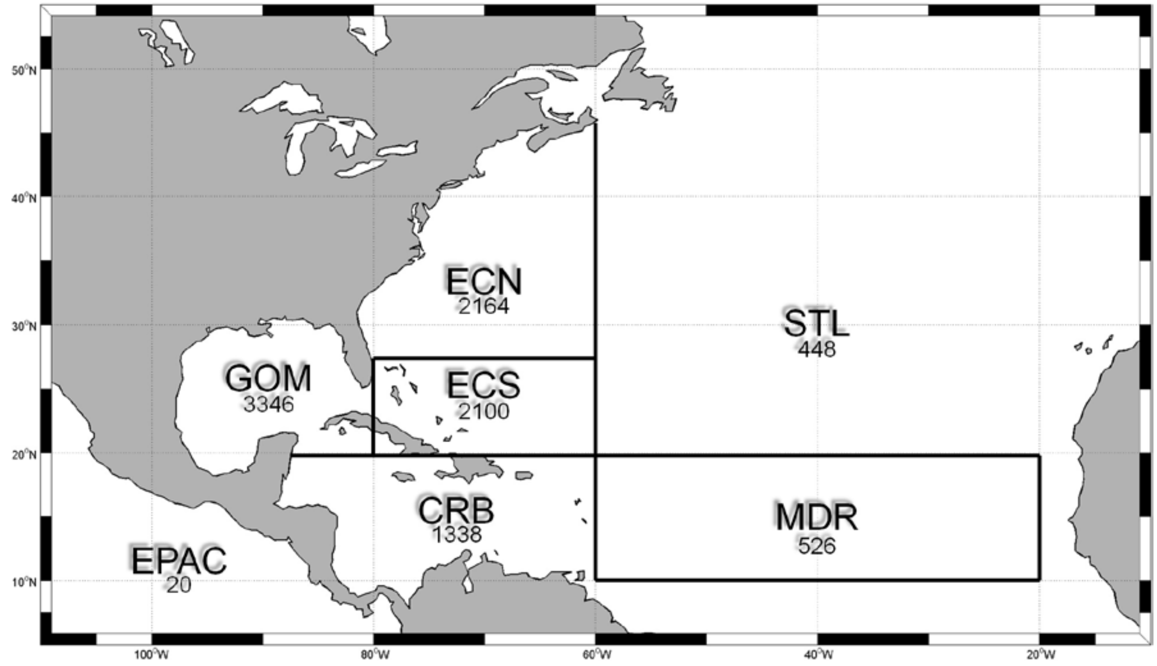

Figure 1. North Atlantic subregions referenced with the corresponding distribution of GPS dropsondes considered by this study.

The second hypothesis asserts that azimuthal variations in the physical components of the hurricane vortex, including the speed and height of the maximum relative tangential wind, the spatial distribution of relative inflow and outflow, and the depth of the mixed layer, produce quantifiable radial variability in hurricane boundary layer characteristics. To this end, material differences in boundary layer height might be identified for specific storm-relative regions (Figure 2) around a hurricane (e.g., front-right quadrant, rear quadrants, etc.).

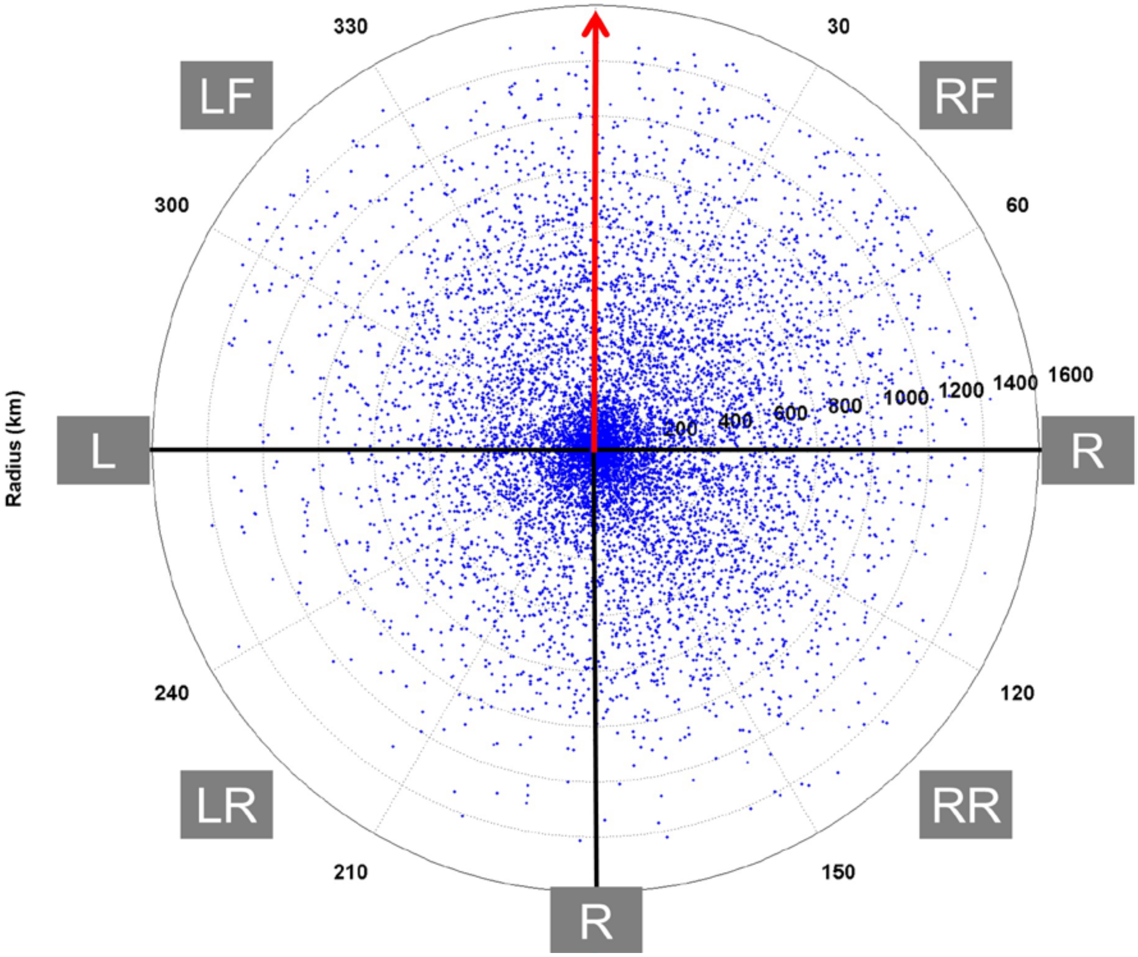

Figure 2. Azimuthal distribution of GPS dropsondes in storm-relative polar coordinates. Each point represents a discrete dropsonde released into a hurricane environment. A thick red vector indicates the universal storm heading (i.e., always coincident with storm motion). Thick black lines identify the boundaries between storm-relative quadrants that are labeled with two-character boxes according to left-right and front-rear positions.

Each hypothesis enhances the composite representation of the hurricane boundary layer environment in an explicit spatial and temporal expansion of the generalized results of the Z11 study. Similarly, each hypothesis is designed to investigate a new mode of boundary layer variability that has yet to be examined in related studies of tropical cyclones. Finally, this thesis will attempt to link relevant boundary layer processes and the hurricane environment to observed variations in the hurricane boundary layer height.

C. NAVAL RELEVANCE

While the scientific benefits of this study are primarily derived from potential improvements in our knowledge of the tropical cyclone environment, and in the dynamical and thermodynamical mechanisms governing the physical processes of the hurricane boundary layer, the practical relevance to naval forces is more prosaic. In simple terms, the United States Navy (USN) and, by extension, the Depart of Defense (DOD), require skillful predictions of tropical cyclone position and intensity to manage resource protection concerns while simultaneously optimizing the safety and continuity of Fleet operations.

The functional intersection of these considerations lies in numerical predictions of tropical cyclone intensity and their dependence on the analytical details of hurricane boundary layer parameterization schemes (Z11). In this way, a deeper understanding of the radial variability of boundary layer height may ultimately lead to improvements in the skill of hurricane forecasts. As a result, this thesis has implicit utility for future decision makers; hurricane forecasts that provide consistency, quality and value, vis-à-vis “forecast goodness,” more fully address the opportunity costs and planning uncertainty associated with tropical cyclone risk management (Murphy 1993). For these reasons, fundamental research into the hurricane boundary layer may provide a meaningful return on investment for military staffs seeking superior forecast guidance.

THIS PAGE INTENTIONALLY LEFT BLANK

II. BACKGROUND

A. THE PLANETARY BOUNDARY LAYER

As the portion of the atmosphere that facilitates the exchange of energy and momentum between the lower troposphere and the surface of the Earth, the atmospheric boundary layer (ABL), or planetary boundary layer (PBL), plays an important role in the evolution of sensible weather events like tropical cyclones (Holton 2004, henceforth H04). In analytical terms, one may characterize the PBL by the timescale of its response to surface forcing: typically one hour or less (Stull 1988). Alternatively, one may identify the PBL by the presence of turbulence; that is, by the turbulent eddies generated from wind shear and convection near the planet's surface (H04). A product of the canonical no-slip boundary condition in the viscous sublayer (Figure 3), vertical wind shear and surface buoyancy provide a meaningful source of turbulent kinetic energy (TKE) for the PBL (H04).

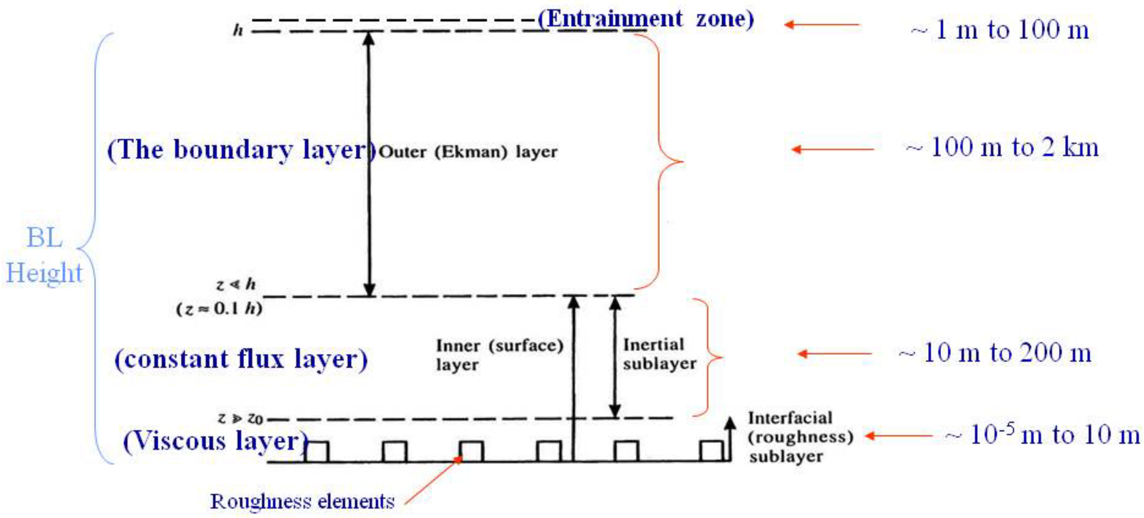

Figure 3. Sublayers of the atmospheric boundary layer and the range of their vertical extent (from Q. Wang 2013; after Garratt 1992).

The distribution of kinetic energy in all scales of disturbances is illustrated in Figure 4. This figure identifies the presence of an energy gap at the mesoscale between the mean flow, centered at synoptic scales, and small scale turbulent eddies. The most energetic turbulent eddies drive the energy cascade process that transfers TKE from large energy containing eddies, which are often defined by the properties of the mean flow, the surface forcing, and the physical dimensions of the PBL, to dissipation eddies at the Kolmogorov microscale (Moeng 1984). At these small length scales, turbulent eddies act as an energy sink that convert TKE into heat through molecular viscosity. In this sense, the PBL is generally distinguished from the rest of the troposphere by its stochastic flow properties involving turbulent mixing. While comparatively unassuming, the TKE contained at these small length scales is analytically significant to the energy and momentum budgets of the PBL (H04). As a result, the geostrophic approximation in the PBL is compromised; without a viable simplification in the governing physical equations, skillful predictions of PBL behavior are similarly degraded (H04).

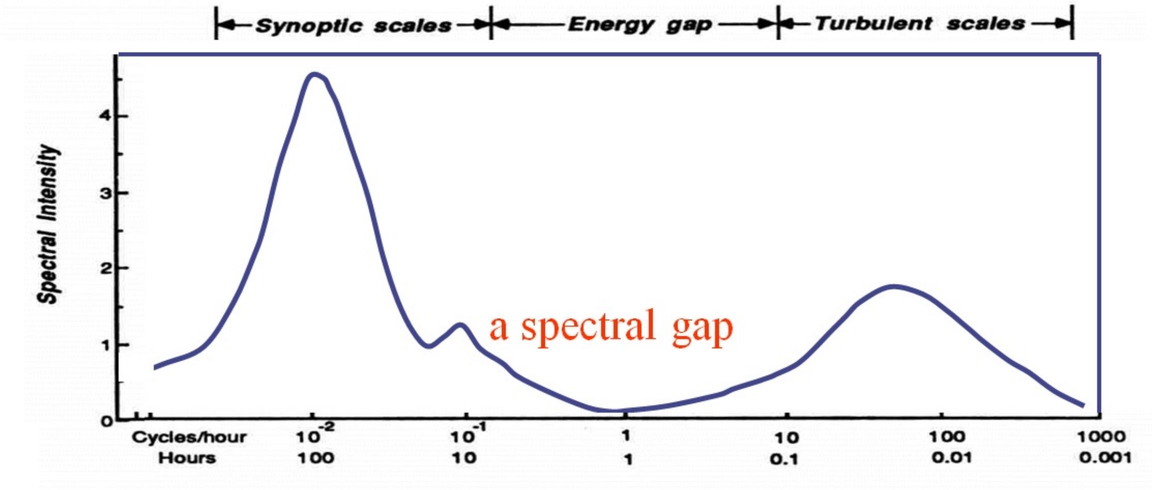

Figure 4. Schematic of the spectral energy density distribution of a near-surface wind field (from Q. Wang 2009; after Stull 1988).

The irregularity of turbulent flows necessarily precludes a closed-form, deterministic solution to the equations of motion that predict the behavior of fluids and, by extension, the atmosphere. In fact, this conceptual singularity is not isolated to PBL research. The Clay Mathematics Institute has identified the existence and smoothness of the Navier-Stokes equations as a Millennium Problem; that is, one of the six most significant unsolved problems in mathematics (Fefferman 2000). As a result, various methods of turbulence closure are employed to resolve the indeterminacy of the nonlinear perturbation terms in the Navier-Stokes equations.

While model closure provides a viable means of moving beyond the analytical difficulties of turbulence, it does not address practical considerations associated with empirical measurements of the PBL environment. Even with established methods of statistical estimation, such as the eddy correlation technique, there may be a practical limit to the sampling frequency available to fully resolve the desired length scales of turbulent motions (Dai et al. 2014, henceforth D14). Moreover, it may be difficult or impractical to directly measure turbulent fluxes in the atmosphere. These complications are of little direct consequence to the free atmosphere above the PBL, where scaling arguments and valid approximations to the Navier-Stokes equations make it possible to reliably describe the synoptic scale motions of the mean flow (H04). By comparison, the size of energy-containing turbulent eddies (Figure 4) has an important effect in the PBL; these motions are often too small to be spatially resolved within the network of available routine observations (H04). This is particularly true of atmospheric conditions inside of a tropical cyclone, where the ability to investigate the energetic hurricane environment is often constrained by non-trivial operational considerations such as crew safety, storm location, and cost. As demonstrated by Smith and Thomsen (2009), the sensitivity of tropical cyclone intensity predictions on boundary layer parameterization schemes communicates the impact of sparse turbulence-resolving observations on numerical simulations of the PBL environment. (Z11).

Nevertheless, alternative methods of characterizing the PBL have been developed to estimate important boundary layer properties. For example, a vertical sounding of the atmosphere may be compared to a posteriori spatial variability in sensible weather variables to estimate the depth of the PBL (D14). The utility of this approach lies in the ubiquitous availability of rawinsondes and dropsondes and, perhaps more importantly, the ability to capture turbulence-correlated parameters, such as humidity, temperature, and wind speed, without direct measurements of turbulent fluxes (D14). In this way, boundary layer height has become a focal point in research investigating the characteristic structure and physical processes of the PBL.

1. Depth of the Planetary Boundary Layer

Defining the PBL in terms of turbulence is conceptually meaningful, but it requires the spatial boundaries of turbulent fluxes to be clearly identified. That is, one must quantify the vertical decay of turbulence to determine where its influence becomes negligible. To this end, the depth of the PBL, or boundary layer height, provides a structural reference for turbulence in the troposphere (Figure 5). More specifically, it separates the PBL from the free atmosphere above and communicates the absence of turbulence-induced boundary layer processes (H04).

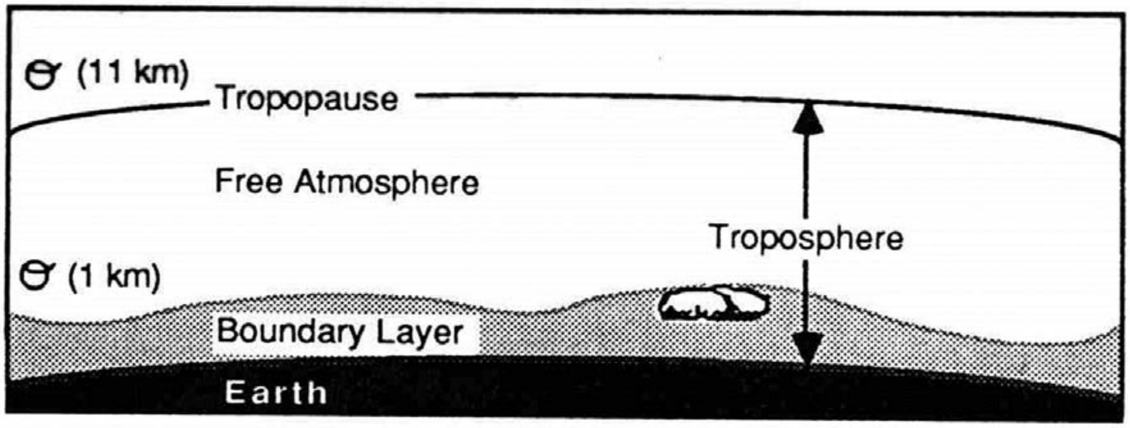

Figure 5. Schematic of the atmospheric boundary layer (from Stull 1988). The boundary layer height is identified by the depth of the hatched area.

While typical boundary layer heights for the midlatitude troposphere will reside on the order of one kilometer, this depth varies depending on factors such as aerodynamic drag, vis-à-vis surface roughness, surface temperature, the static stability of the atmosphere, and large-scale subsidence forcing (H04). Variability in these conditions can produce boundary layer heights as shallow as 30 meters or, with intense convection, as deep as three kilometers (H04). Moreover, diurnal variations in thermal forcing functions can produce large fluctuations in boundary layer depth. This is particularly true over land, where differential heating generally produces more PBL height variability.

The boundary layer height plays a key role in disparate numerical simulations of the atmosphere. Previous studies (e.g., Troen and Mahrt 1986; D14) have identified its impact in models of various aeolian processes, including soil moisture transport, air pollution, and, as it relates to this thesis, weather prediction. Moreover, Stull (1988) identified the importance of boundary layer height to physical processes within the PBL, which may be inferred from vertical profiles of variables such as energy, heat, and moisture (Z11). These physical processes, in turn, may affect the details of various PBL parameterizations. Furthermore, the depth of the PBL may be used to determine characteristic length scales for turbulent eddies and provide turbulence closure for various numerical weather prediction (NWP) models (D14). For these reasons, reliable methods of boundary layer height estimation are desired to quantify the impact of the PBL, and its depth, on relevant physical processes and structures in the troposphere.

2. Determining Boundary Layer Height

The established definition for boundary layer height is based on the vertical gradient of turbulent fluxes; that is, the height in the troposphere where continuous turbulent transport becomes negligible (D14). While this method is conceptually robust, it is not ideal for numerical applications. To this end, the height of the boundary layer is often estimated by a quantifiable decay in vertical momentum flux: typically down to 5% of its original surface value (Z11). While this method of boundary layer height estimation is analytically tractable, the aforementioned difficulty in sampling turbulent fluxes in the PBL degrades its value in many practical applications.

Another method of boundary layer height estimation relies on a non-dimensional parameter to characterize dynamic stability in fluid flows. The gradient Richardson number and, in finite-difference form, the bulk Richardson number (Equation 1) describe the production and dissipation of turbulent eddies through buoyancy and shear as

$$Ri_b = \frac{\left(\dfrac{g}{\overline{\overline{\theta}_v}}\right)\Delta\overline{\theta}_v \Delta z}{\left(\Delta\overline{U}\right)^2 + \left(\Delta\overline{V}\right)^2}, \tag{1}$$

where Ri_b is the bulk Richardson number between two layers separated by thickness Δz, g is the gravitational acceleration, θ_v is the virtual potential temperature, ΔU and ΔV

correspond to the vertical changes in horizontal winds between two layers separated by thickness Δz, and the overbar symbols indicate a mean quantity (AMS 2014a).

The bulk Richardson number may be used to diagnose the presence of continuous turbulence; when above a critical value, which is often chosen to between 0.15 and 0.55, the relative contributions of buoyancy and shear are such that dynamic stability is predicted (D14). Nevertheless, the real utility of the bulk Richardson number lies in its dependence on mean variables readily obtained from forecast model grids within or immediately above the PBL. Similar quantities, although not averaged, can be obtained from single profile measurements such as those from rawinsondes or dropsondes. In this sense, the discontinuous yet robust observing network of rawinsondes and dropsondes is ideally situated to produce frequent estimates of boundary layer height. This virtue is constrained, however, by the lack of consensus on an appropriate threshold for the critical Richardson number (D14).

Several other practical estimates of boundary layer height, each with a similar dependence on profile observations, may be broadly categorized as dynamical or thermodynamical by their corresponding analytical characteristics (Z11). Methods that rely on variability in the vertical profiles of wind speed or wind shear, as described by D14, may be identified as dynamical. Similarly, methods that quantify the temperature profile of the atmosphere, often in the context of a temperature inversion near the top of the PBL, may be classified as thermodynamical. In simple terms, the latter class of estimates describes the characteristic variability of the mixed layer depth through, for example, temperature anomalies with respect to a meaningful reference value or, alternatively, vertical gradients in the lapse rate of the atmosphere (Z11). In either case, these definitions seek to capture the layer of the troposphere "where virtual potential is appreciably well mixed" (S10).

Regardless of the method selected, the vast array of schemes available to estimate the height of the boundary layer, and their corresponding critical values, betray an intrinsic difficulty in such investigations. While several studies (e.g., S10; Z11; D14) have contributed to the resolution of this apparent ambiguity, additional research is needed to recover the analytical fidelity of various methods of determining boundary layer height in specialized environments such as hurricanes.

B. THE HURRICANE BOUNDARY LAYER

The importance of the boundary layer in tropical cyclone development and steady-state maintenance, both in the real atmosphere and in numerical simulations, has been well-documented (e.g., E86; Smith et al. 2008; Smith et al. 2009; S10; Z11). In simple terms, the hurricane boundary layer is the interface between the storm and its energy source: warm ocean waters. It provides a physical stage upon which the coupled ocean-atmosphere system acts to balance its sources and sinks of energy and momentum. This abstract relationship is personified by the spatial transport of physical properties, such as enthalpy, moisture, and momentum, both radially and vertically, within and beyond the PBL of a mature hurricane (Z11). In this way, the hurricane boundary layer governs the positive feedback loop of the canonical tropical cyclone heat engine, sustaining it against structural instability and physical decay.

As previously described, however, the tropical cyclone environment is not easy to sample. Radial arms of interleaving, intense convection combine with an energetic wind field to make direct measurements of turbulent fluxes both difficult and rare (Z11). As a result, several methods for estimating the height of the hurricane boundary layer have been investigated (e.g., S10, Z11). Reflecting the diversity of options, these specialized studies compared the validity of various height estimates against a posteriori knowledge of hurricane boundary layer behavior and variability. Moreover, they implicitly examined the potential for an optimal boundary layer height estimate in numerical predictions of tropical cyclone intensity. In the case of S10, specifically, several estimates of boundary layer height were investigated to reexamine the established role of the boundary layer in hurricane intensification.

Selecting several of the methods identified by D14, Z11 differentiated relevant characteristic heights scales into two basic categories: dynamical and thermodynamical. The dynamical definitions focus on aeolian components of the hurricane vortex; that is, on the height of the maximum total wind speed (h_{vmax}) and inflow layer depth (h_{infl}), as originally identified by Bryan and Rotunno (2009) and Smith et al. (2009), respectively. In this context, inflow layer depth is defined by the presence of significant storm-relative radial inflow (Smith et al. 2009). In the Z11 study, and for this thesis, inflow layer depth was quantitatively determined by the vertical decay of relative radial winds; that is, the height at which the radial inflow is 10% of the peak near-surface value.

By comparison, the thermodynamical definitions rely on the identification of the mixed layer depth, as first suggested by Moss and Merceret (1976) in their investigation of Hurricane Eloise (Z11). The first thermodynamical method utilized in the Z11 study, introduced by Anthes and Chang (1978), identifies the mixed layer depth by a virtual potential temperature anomaly; that is, when the virtual potential temperature departs from the mean of the lowest 150 meters of the troposphere by 0.5 K or more. The second thermodynamical method in Z11, established by Zeng et al. (2004), also examines a change in the virtual potential temperature profile; however, for this definition, a virtual potential temperature lapse rate greater than 3 K km^{-1} establishes the top of the boundary layer.

Finally, Z11 also includes the bulk Richardson number in their examination of the hurricane boundary layer. While not explicitly included in their list of dynamical and thermodynamical height estimates, its prevalence in various PBL parameterization schemes provides a motivation for additional investigation. As a result, Z11 considers a modified form of the bulk Richardson number as

$$Ri_b = \frac{\left(\dfrac{g}{\theta_{vs}}\right)\left(\theta_H - \theta_{vs}\right)\left(H - z_s\right)}{\left(U_H - U_s\right)^2}, \tag{2}$$

where Ri_b is the bulk Richardson number evaluated between an arbitrary height z_s and boundary layer height H, g is the gravitational acceleration, θ_v is the virtual potential temperature, and the subscripts s and H identify the levels of z_s and H, respectively (Z11).

For each class of methods, representing both dynamical and thermodynamical definitions, the relevant physical properties and corresponding thresholds tend to coincide with a height where turbulent fluxes become negligible (Z11). In this sense, they attempt to model the conceptual foundation of the true definition of boundary layer height. Nevertheless, the selection of appropriate critical values necessarily complicates the matter and introduces non-trivial uncertainty into the estimation process (D14). To this end, additional research is required to identify subtle variations in the behavior of these properties near the true boundary layer height and, if possible, determine if the observed variability is analytically or physically relevant to the hurricane environment.

THIS PAGE INTENTIONALLY LEFT BLANK

III. DATA AND METHODOLOGY

A. THE NCAR GPS DROPSONDE

Recent observational studies of tropical cyclones (e.g., Z11; Ziemba 2013) have utilized data collected from National Center for Atmospheric Research (NCAR) GPS dropsondes to evaluate the physical properties of hurricanes. In each case, these airborne measurement devices provided a reliable and accurate means of sampling the inimical, and sometimes remote, atmospheric conditions inside of a tropical cyclone. In a similar manner, this thesis relies on NCAR GPS dropsondes to examine the composite hurricane environment, identify its characteristic structures, and quantify meaningful radial variability in hurricane boundary layer depth.

Introduced as a part of the Airborne Vertical Atmospheric Profiling System (AVAPS) in 1996, the current generation of NCAR GPS dropsondes (Figure 6) was developed in a joint venture between the National Oceanic and Atmospheric Administration (NOAA), the German Aerospace Research Establishment (DLR), and the Atmospheric Technology Division at NCAR (Hock and Franklin 1999, henceforth H99). Utilized by civilian and military agencies alike, NCAR GPS dropsondes provide high-resolution, high-accuracy measurements (Table 1) of several important atmospheric properties (H99). This quality is particularly valuable over data-sparse regions, such as those typically required for tropical cyclone development and stead-state maintenance, where traditional observation networks are poorly distributed or entirely absent.

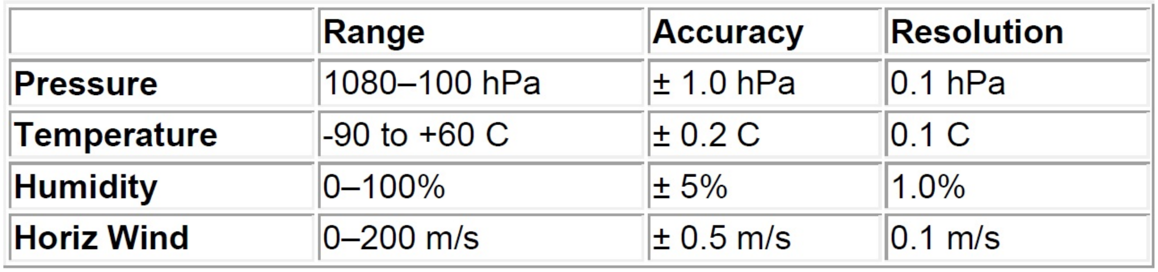

	Range	Accuracy	Resolution
Pressure	1080–100 hPa	± 1.0 hPa	0.1 hPa
Temperature	-90 to +60 C	± 0.2 C	0.1 C
Humidity	0–100%	± 5%	1.0%
Horiz Wind	0–200 m/s	± 0.5 m/s	0.1 m/s

Table 1. Specifications and estimated operational performance of the NCAR GPS dropsonde (from Ziemba 2013; after H99).

Data from two distinct GPS sensors were considered in this study. The GPS121 device provides a 2 Hz sampling frequency for all atmospheric variables (Young et al. 2013, henceforth Y13). While the UBLOX sensor delivers the same resolution for thermodynamic properties, wind data are available at a rate of 4 Hz (Y13). Moreover, the NCAR GPS dropsonde has a mean boundary layer descent rate between 12-14 m s^{-1} and typical sampling frequency of 2 Hz; this provides a coarse estimate for the vertical spatial resolution of the device: 6-7 meters (Z11). These considerations are more than academic; NCAR GPS dropsondes provide a non-trivial improvement in the accuracy of dynamical boundary layer height estimates when compared with the previous generation of Omega-based wind speed measurements (H99). A more detailed description of AVAPS features, specifications, and quality control measures, as originally introduced by H99, are examined by Z11 and Ziemba (2013).

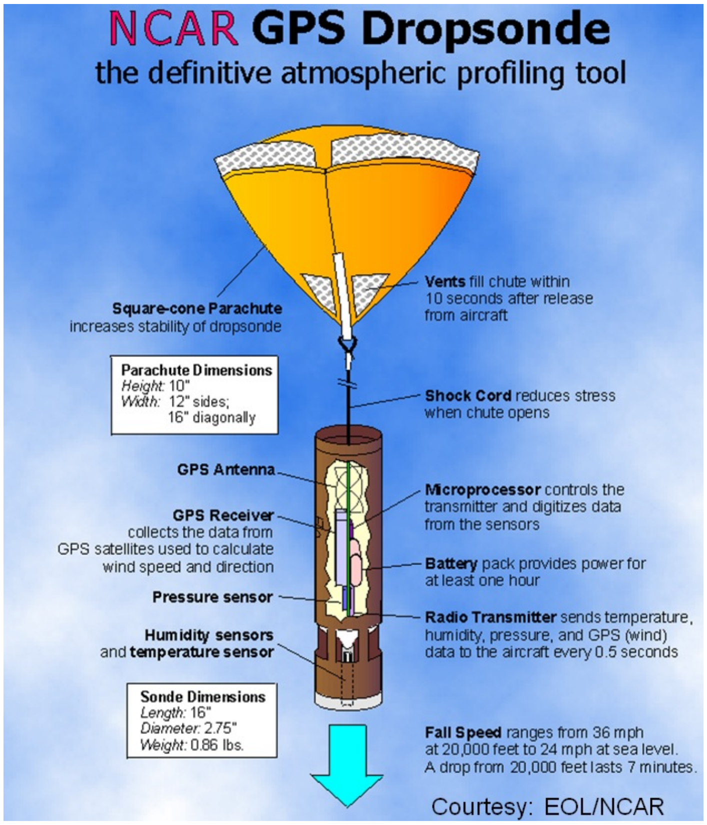

Figure 6. Schematic of the NCAR GPS dropsonde identifying vital capabilities, components, and subsystems (From EOL 2014a).

B. DATA

1. Long-Term NOAA Dropsonde Hurricane Archive

The Long-Term NOAA Dropsonde Hurricane Archive is a high-resolution, quality controlled dataset spanning 17 years of tropical cyclone observations between 1996 and 2012 (Y13). During this period, over 13,000 NCAR GPS dropsondes (Table 2) were released by National Hurricane Center (NHC) and Hurricane Research Division (HRD) aircraft into the disparate atmospheric conditions of 123 North Atlantic and East Pacific tropical cyclones (Figure 7). Curated by the Earth Observing Laboratory (EOL) for NCAR, the National Science Foundation (NSF), and NOAA, this dataset provides a robust numerical domain for the statistical interrogation of the canonical hurricane environment.

Year	# of Storms	Soundings in final archive
1996	7	68
1997	7	388
1998	7	1124
1999	11	1105
2000	8	311
2001	8	709
2002	7	948
2003	5	769
2004	5	1332
2005	13	2306
2006	5	470
2007	6	361
2008	8	1302
2009	5	540
2010	9	954
2011	9	278
2012	3	716
Total		**13681**

Table 2. Annual distribution of NCAR GPS dropsondes and storm events considered by this study (from Y13).

Designed to facilitate a broad range of research projects within the scientific community, the archive is reviewed and updated on a regular basis. As recently as December 2013, it was amended to include calculated estimates of radius, azimuth, and vertical wind for each dropsonde (Y13). The latest iteration provides 21 discrete fields of data in the ASCII text format (Figure 8). While a small number of categories are devoted to prosaic administrative details, such as the time, date, and location of the dropsonde, the majority of the fields are concerned with measured and calculated estimates of the physical properties of the atmosphere. Examples of importance in this study include geopotential altitude, total wind speed and direction, dry-bulb temperature, relative humidity, radius, and azimuth.

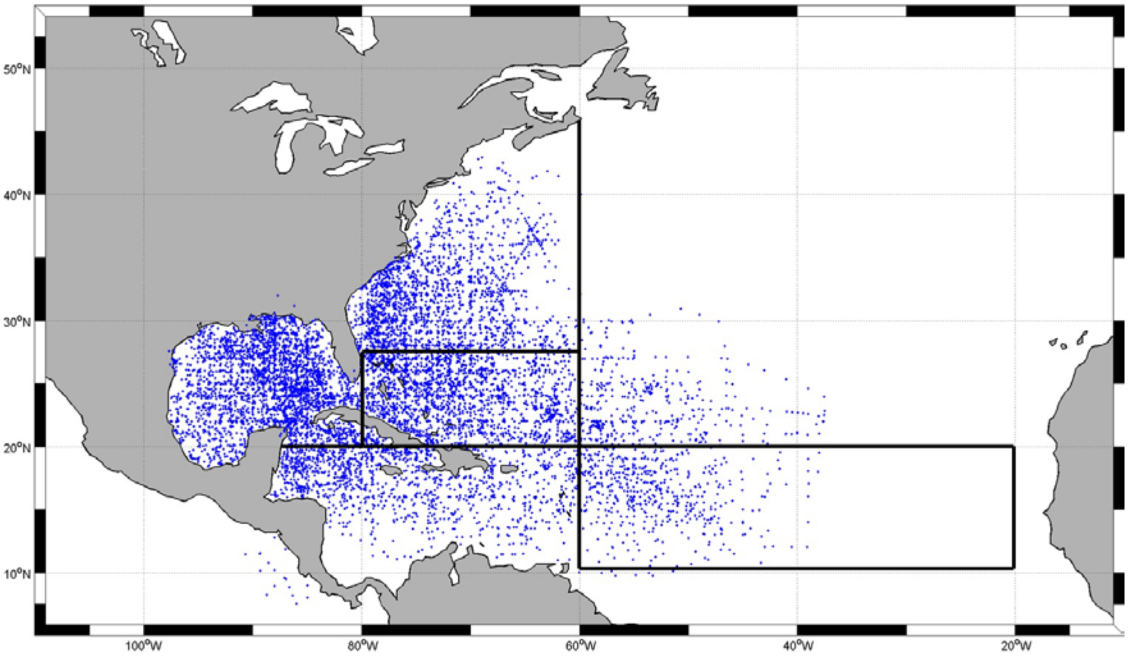

Figure 7. Spatial distribution of the Long-Term NOAA Dropsonde Hurricane Archive. Each point represents the location of an NCAR GPS dropsonde considered by this study. Black lines denote the boundaries between subregions.

However, the addition of radius and azimuth data is significant for another reason. While the NCAR dropsondes utilized in this archive are well-equipped to sample any atmosphere, they have no direct means of collecting so-called metadata about the storm into which they were dropped. Both hypotheses explored in this thesis, and indeed every dynamical and thermodynamical definition of boundary layer height, explicitly require each dropsonde be spatially referenced against the center of their temporally correlated tropical cyclone. In this way, the new radius and azimuth fields are essential to the successful execution of this study. However, even in this respect, they fail to supply all of the desired storm-specific information; the data contained in the Long-Term NOAA Dropsonde Hurricane Archive are arranged in an Earth-relative coordinate system. Since research into the hurricane environment routinely examines important atmospheric properties in a storm-relative sense, the Revised Hurricane Database (HURDAT2) is required to provide a numerical reference for storm-relative coordinate transformations.

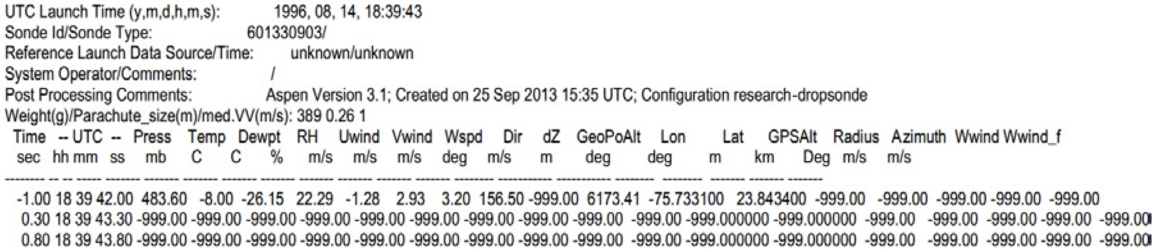

```
UTC Launch Time (y,m,d,h,m,s):          1996, 08, 14, 18:39:43
Sonde Id/Sonde Type:                    601330903/
Reference Launch Data Source/Time:      unknown/unknown
System Operator/Comments:               /
Post Processing Comments:               Aspen Version 3.1; Created on 25 Sep 2013 15:35 UTC; Configuration research-dropsonde
Weight(g)/Parachute_size(m)/med.VV(m/s): 389 0.26 1
 Time  -- UTC --  Press   Temp  Dewpt   RH    Uwind  Vwind  Wspd    Dir    dZ   GeoPoAlt   Lon        Lat      GPSAlt  Radius  Azimuth  Wwind Wwind_f
  sec  hh mm  ss    mb     C      C      %     m/s    m/s    m/s    deg    m/s     m        deg        deg      m       km      Deg    m/s    m/s
-------- -- -- ----- ------- ------- ------- ------- ------- ------- ------- ------- ------- -------- ---------- ---------- -------- -------- ------- ------- -------
  -1.00 18 39 42.00  483.60   -8.00  -26.15   22.29   -1.28    2.93    3.20  156.50 -999.00  6173.41 -75.733100  23.843400 -999.00  -999.00 -999.00 -999.00 -999.00
   0.30 18 39 43.30 -999.00 -999.00 -999.00 -999.00 -999.00 -999.00 -999.00 -999.00 -999.00  -999.00 -999.000000 -999.000000 -999.00  -999.00 -999.00 -999.00 -999.00
   0.80 18 39 43.80 -999.00 -999.00 -999.00 -999.00 -999.00 -999.00 -999.00 -999.00 -999.00  -999.00 -999.000000 -999.000000 -999.00  -999.00 -999.00 -999.00 -999.00
```

Figure 8. Example of the ASCII text format utilized by the Long-Term NOAA Dropsonde Hurricane Archive in EOL sounding files (from Y13).

2. Revised Atlantic Hurricane Database (HURDAT2)

In contrast to the Long-Term NOAA Dropsonde Hurricane Archive, the HURDAT2 database is specialized by NHC for tropical cyclone metadata. Incorporating all available observations, including those unavailable to forecasters in real-time, it provides a historical archive of post-storm analysis data compiled from so-called b-decks within the Automated Tropical Cyclone Forecasting (ATCF) system (Landsea et al. 2014). Each b-deck provides an operational record of tropical cyclone properties, such as position, status (Figure 9), maximum sustained surface wind, and central pressure. These data are furnished in a universal text format at synoptic time intervals (e.g., 0000, 0600, 1200, and 1800 UTC) or when a significant event, such as landfall, is recorded (Landsea et al. 2014). Beginning in 2004, the database also incorporated estimates for storm-relative wind radii at relevant intensity thresholds: 34, 50 and 64 knots (Ziemba 2013).

In this way, HURDAT2 provides georectification for every NCAR GPS dropsonde considered within the Long-Term NOAA Dropsonde Hurricane Archive. Each dropsonde may then be coupled to its temporally correlated storm and, more importantly, the physical properties of the hurricane boundary layer may be spatially referenced within a universal storm-relative coordinate system.

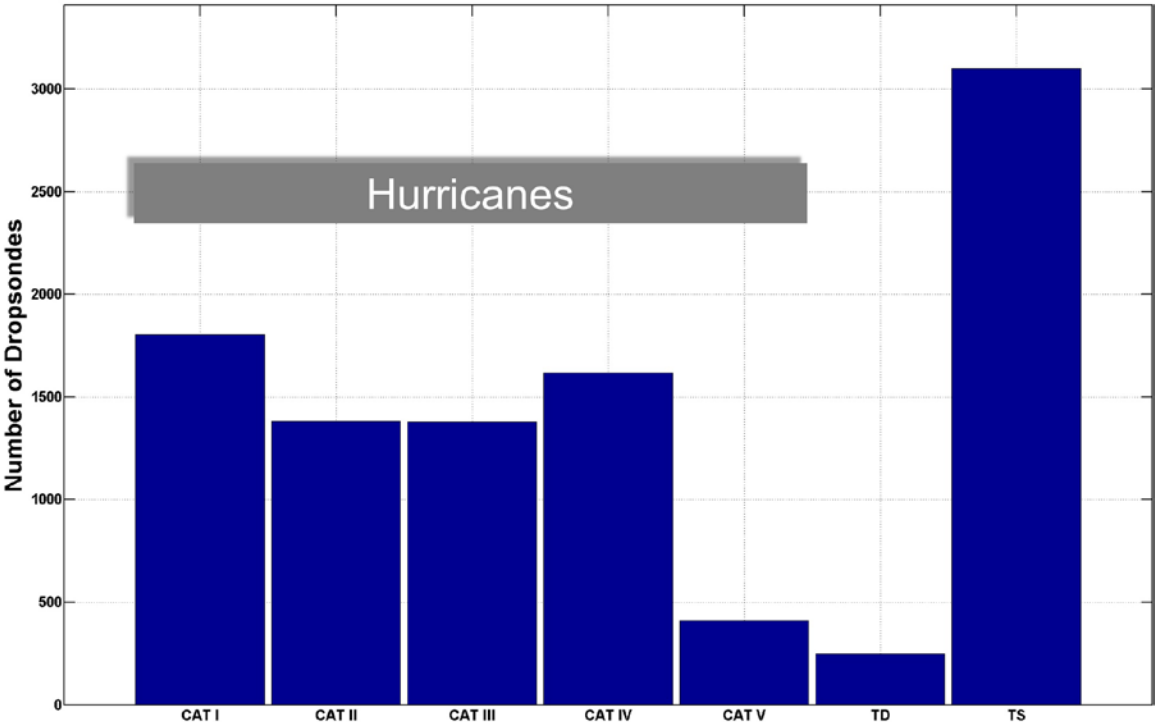

Figure 9. The relative frequency of tropical cyclone categories sampled in the Long-Term NOAA Dropsonde Hurricane Archive. The grey bar identifies the categories of the Saffir-Simpson hurricane scale (SSHS).

3. Data Coverage

The Long-Term NOAA Dropsonde Hurricane Archive contains over seven million atmospheric measurements of the hurricane environment. When combined with the HURDAT2 database, each observation was decomposed into 73 distinct fields of information; examples of importance include geopotential altitude, virtual potential temperature, radial and tangential wind speed, storm location and heading, storm-relative radius and azimuth, and storm quadrant (RF, LR, etc.). In this way, nearly 500 million pieces of data were categorized for numerical analysis and conditioning.

An examination of the spatial distribution of dropsonde observations reveals several noteworthy properties of the unified dataset. To begin, the majority of NCAR GPS dropsondes considered in the study were released over the GOM, ECN, and ECS subregions in close proximity to the contiguous United States (Figure 10). The MDR and STL subregions, by comparison, are undersampled by nearly an order of magnitude. Moreover, the two subregions with characteristically tropical atmospheres (i.e., the MDR and CRB) contain less than 20% of the dropsondes examined in this thesis. While these findings are reasonable when compared with the operational range of weather reconnaissance aircraft, and more specifically in relation to the airfields from which these aircraft operate, it nevertheless dilutes the confidence of composite analysis results obtained in the data-sparse MDR, CRB, and STL subregions. More importantly, these population disparities have the potential to complicate meaningful boundary layer height comparisons in the context of regional conditioning.

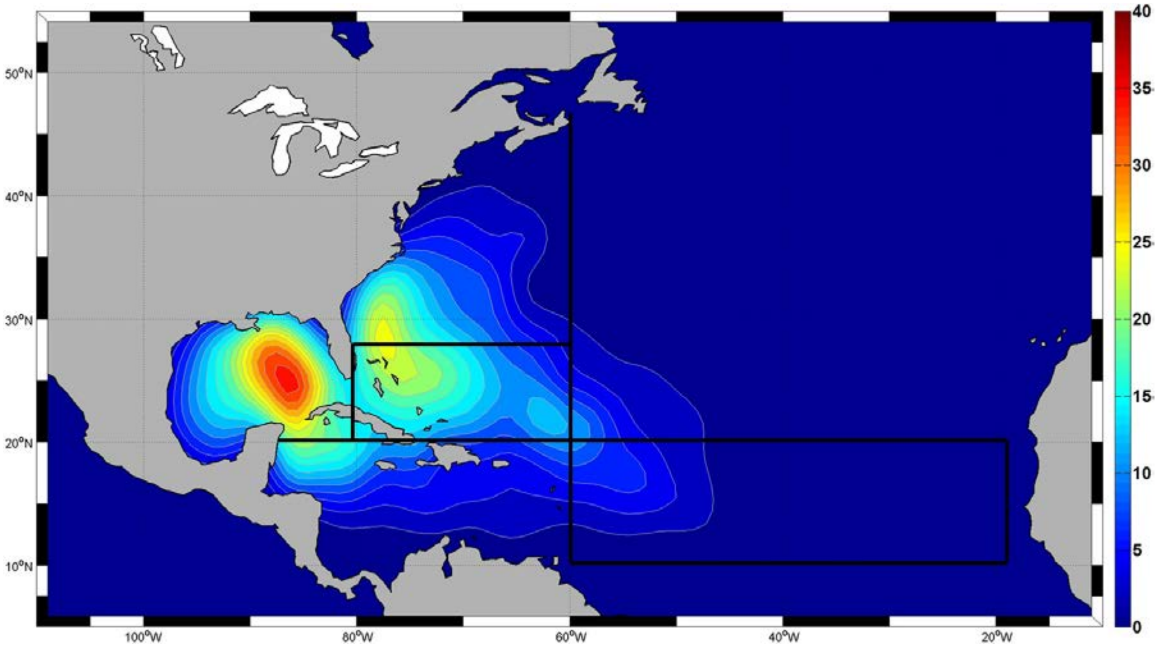

Figure 10. Spatial distribution of the Long-Term NOAA Dropsonde Hurricane Archive. Shaded contours correspond to the number density of NCAR GPS dropsondes grouped into 1^{o} latitude/longitude rectangular bins. Black lines denote the boundaries between subregions.

When a similar analysis of the azimuthal dropsonde distribution (Figure 11) is performed, the dataset reveals an additional spatial inclination. That is, a clear majority of dropsondes were released by NOAA aircraft over the right semicircle (i.e., the spatial combination of the right-front and right-rear quadrants) of their corresponding storms. Moreover, the dropsondes indicate a marginal, yet non-trivial sampling bias towards the right-front quadrant. A justification for this tendency lies with the convolution of the tropical cyclone forward motion with its characteristic cyclonic flow; that is, with respect to an Earth-relative coordinate system, this temporally unsteady superposition produces a stronger (weaker) wind field on the right (left) side of the canonical storm vortex. As a result, the right semicircle of a well-organized tropical cyclone typically provides a more dynamic environment for GPS dropsonde to investigate.

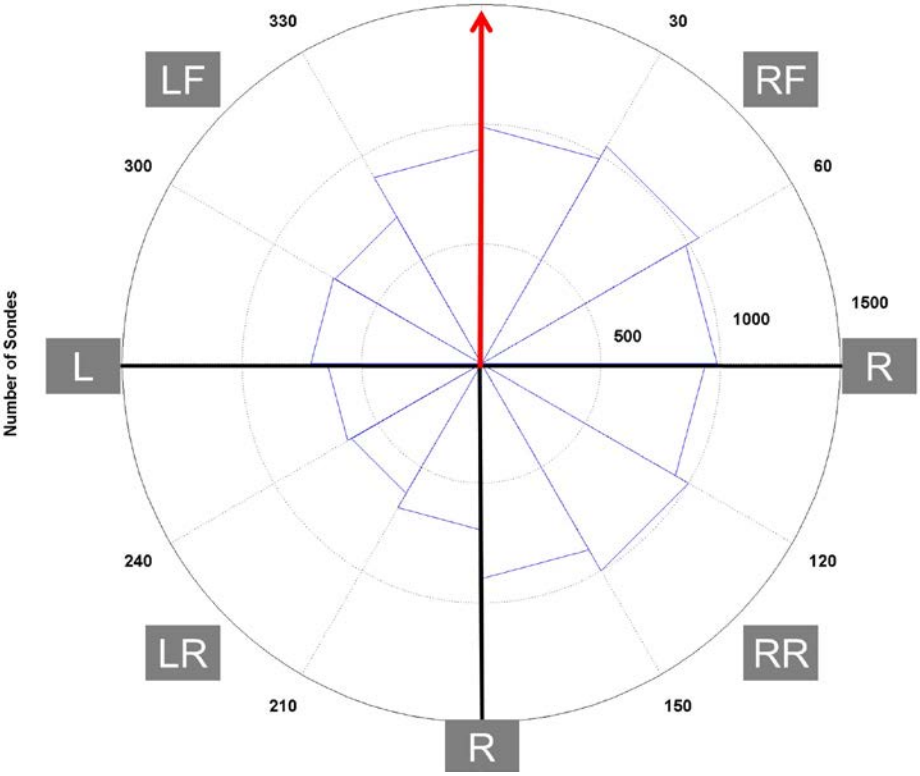

Figure 11. The azimuthal distribution of GPS dropsondes in a storm-relative coordinate system. Each blue box corresponds to a 30^{o} azimuthal bin. A thick red vector indicates the universal storm heading; thick black lines identify the boundaries between storm-relative quadrants.

If the unified dataset is further conditioned to produce azimuthal dropsonde distributions for various North Atlantic subregions (Figure 12), a notable distinction emerges. The GOM, ECN, ECS, and STL subregions indicate a shared bias for the front and right semicircles of a tropical cyclone. However, the tropical MDR and CRB subregions, disproportionally favor the left semicircle. While at first counterintuitive, this finding is consistent with weather reconnaissance aircraft searching for a closed surface circulation at formation time over regions such as the MDR and CRB. The presence of westerly flow in the tropics is often indicative of this feature, as it represents a characteristic flow anomaly from the easterly trade winds.

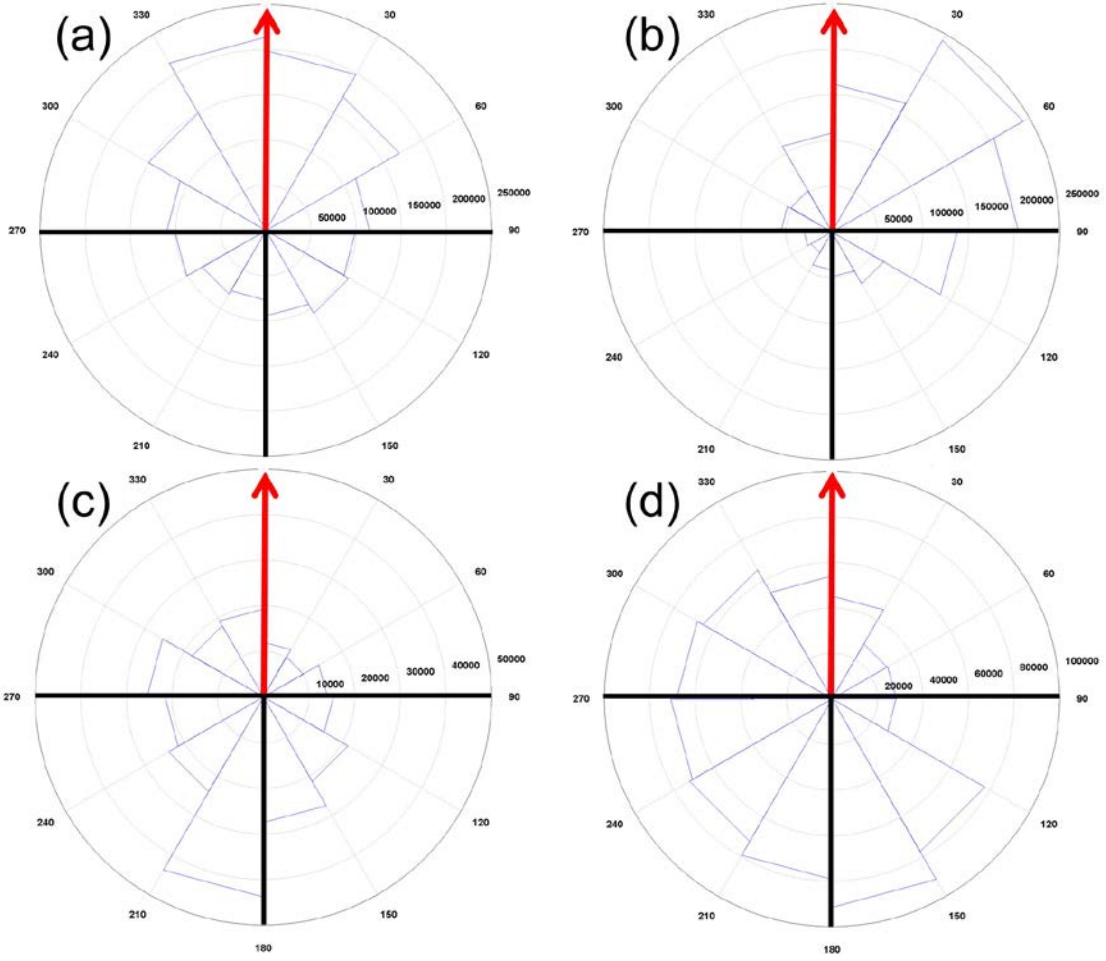

Figure 12. The azimuthal distribution of data in storm-relative coordinates for the (a) GOM, (b) ECN, (c) MDR, and (d) CRB subregions. Each blue box corresponds to a 30^{o} azimuthal bin. Thick red vectors indicate the universal storm heading; thick black lines identify quadrant boundaries.

To first order, the spatial properties of the unified dataset provide an early indication of the potential for regional and azimuthal conditioning. Additionally, they hint at the numerical limitations of this observational study. That is, the non-uniform spatial distributions of the Long-Term NOAA Dropsonde Hurricane Archive compromise the statistical confidence of results obtained for data-sparse regions. For these reasons, this thesis emphasizes the GOM, ECN, ECS, and CRB subregions when validating the regional variability hypothesis. While all quadrants were considered in the azimuthal variability hypothesis, caution was utilized when azimuthal conditioning was superimposed on regional conditioning.

C. ANALYSIS METHODS

1. Numerical Computing

All numerical computations were performed in MATLAB R2014a running on a 64bit version of Windows 7 Ultimate. The large number of observations considered by this study required the MATLAB Parallel Computing Toolbox to replace traditional “for loops” with so-called “parfor loops.” This parallel processing statement was responsible for a non-trivial reduction in numerical computation time and facilitated many aspects of the data conditioning scheme.

The Long-Term NOAA Dropsonde Hurricane Archive was combined with the HURDAT2 database to create a unified dataset in the MATLAB computing environment. This process provided a temporal and spatial reference for each NCAR GPS dropsonde by categorically matching all observations with their corresponding tropical cyclone. An array of structures was also generated to store the physical properties and storm metadata associated with each discrete observation. As previously identified, this master structure contained nearly 500 million pieces of data describing the canonical hurricane environment.

2. Quality Control

Once the unified dataset was ingested into MATLAB, three primary modes of quality control were applied. The first inspected the master structure to identify dropsondes with significant gaps in data. Any dropsonde that failed to record important physical properties, such as geopotential altitude, total wind speed, relative humidity, or storm-relative radius was removed from the dataset. Moreover, dropsondes with status labels (e.g., tropical storm or hurricane) that were inconsistent with the maximum sustained surface winds were deleted. When this mode of quality control was applied to all relevant properties, 2,398 dropsondes were eliminated from consideration.

The second mode of quality control was designed to remove statistical outliers. While there are several rigorous techniques for identifying and removing data that are too distant from the mean, mode, or median of an arbitrary dataset, the so-called 2-sigma approach was selected for this study. That is, any data point found beyond two standard deviations from the mean of its corresponding sample was classified as an outlier. In this way, 95.45% of the original sample was preserved with a smaller corresponding standard deviation. To minimize the inadvertent removal of meaningful vertical or radial variability, the 2-sigma approach was applied only to estimates of the storm-relative radius. These observations corresponded to dropsondes that were well outside of the 300 km radial domain considered by the Z11 study. To this end, 459 radial outliers were removed from the master structure.

The final mode of quality control compared new estimates of the storm-relative radius and azimuth, provided by EOL in December of 2013, to similar data generated by Ziemba (2013) with the HURDAT2 database. After a coordinate transformation was performed on the Long-Term NOAA Dropsonde Hurricane Archive, EOL and Ziemba (2013) solutions were compared in a storm-relative coordinate system for non-trivial azimuthal and radial discrepancies (Figure 13). Disparities between the two datasets are believed to be caused by minor differences in the method used to resolve tropical cyclone heading. Before quality control measures were employed, the mean absolute error (MAE) in azimuth (radius) was found to be 2.4 degrees (1.8 km); similarly, the root-mean-square error (RMSE) for azimuth (radius) was computed to be 13.7 degrees (12.7 km). Once suitable radial and azimuthal thresholds for error were established, 852 inconsistent data points were rejected from the unified dataset. As a result, the MAE of the remaining observations was reduced by a factor of two; the corresponding RMSE decreased by an order of magnitude, indicating a narrower error distribution for the final, quality controlled dataset. This thesis will use the EOL results to be consistent with other studies examining the Long-Term NOAA Dropsonde Hurricane Archive.

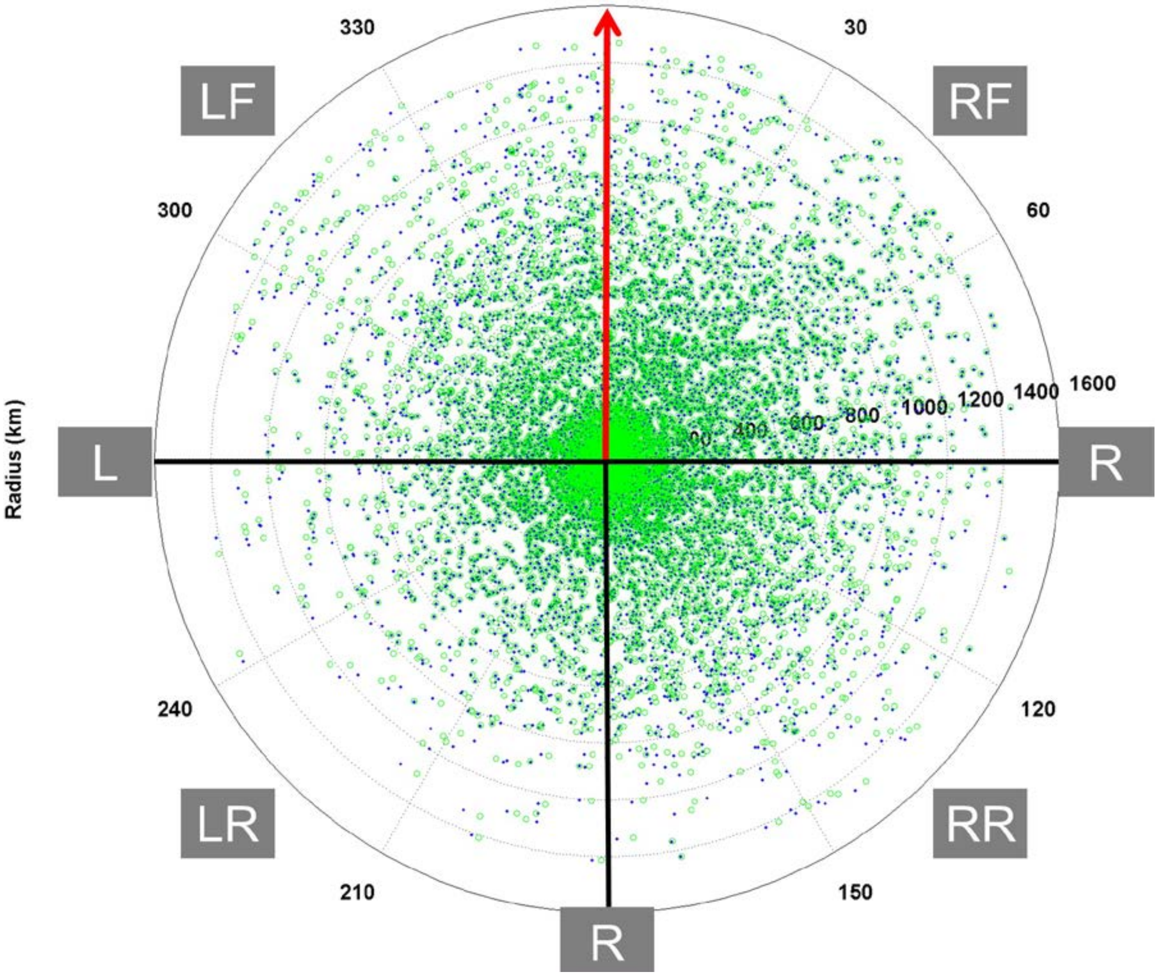

Figure 13. Distribution of quality controlled NCAR GPS dropsondes in storm-relative polar coordinates. Each inscribed concentric circle corresponds to a radial grid increment of 200 km. Each blue point indicates the EOL estimate for dropsonde position after a storm-relative coordinate transformation; each green circle represents the Ziemba (2013) estimate of dropsonde position. A thick red vector indicates the universal storm heading; thick black lines identify the boundaries between storm-relative quadrants.

3. Composite Analysis Technique

The composite analysis technique employed by Z11 served as the foundation for this observational study. Since the spatial averaging of physical properties necessarily obscures the underlying variability of the original data, care was taken to condition the array of structures in such a way that similar tropical cyclones formed the basis for comparisons of disparate elements of the unified dataset (Z11). In this way, the numerical smoothing inherent in the composite analysis technique was normalized by the physical characteristics of corresponding storms (Z11). In simple terms, hurricanes, tropical storms, and tropical depressions were separated in the conditioning process to more easily distinguish their unique dynamical and thermodynamical traits.

A key component of the composite analysis technique is the so-called binning of data (Figure 14). This process deconstructs the continuous radius-height space of a tropical cyclone with bins of variable size to produce a discretized vertical cross-section of the hurricane environment. Each bin physically separates a cluster of neighboring points taken from the original dataset and, with the aid of various bin-averaging schemes, assumes the statistical properties of the data they contain.

In subsequent computations, the center of each bin may be associated with the mean and variance of various physical properties of the atmosphere. While this is numerically convenient in the context of data visualization, it may conceal important characteristics of the original dataset (Z11). Moreover, the combination of data binning and smoothing, the latter of which is discussed in the following section, produces statistical uncertainty that is difficult to quantify in analytical or numerical terms.

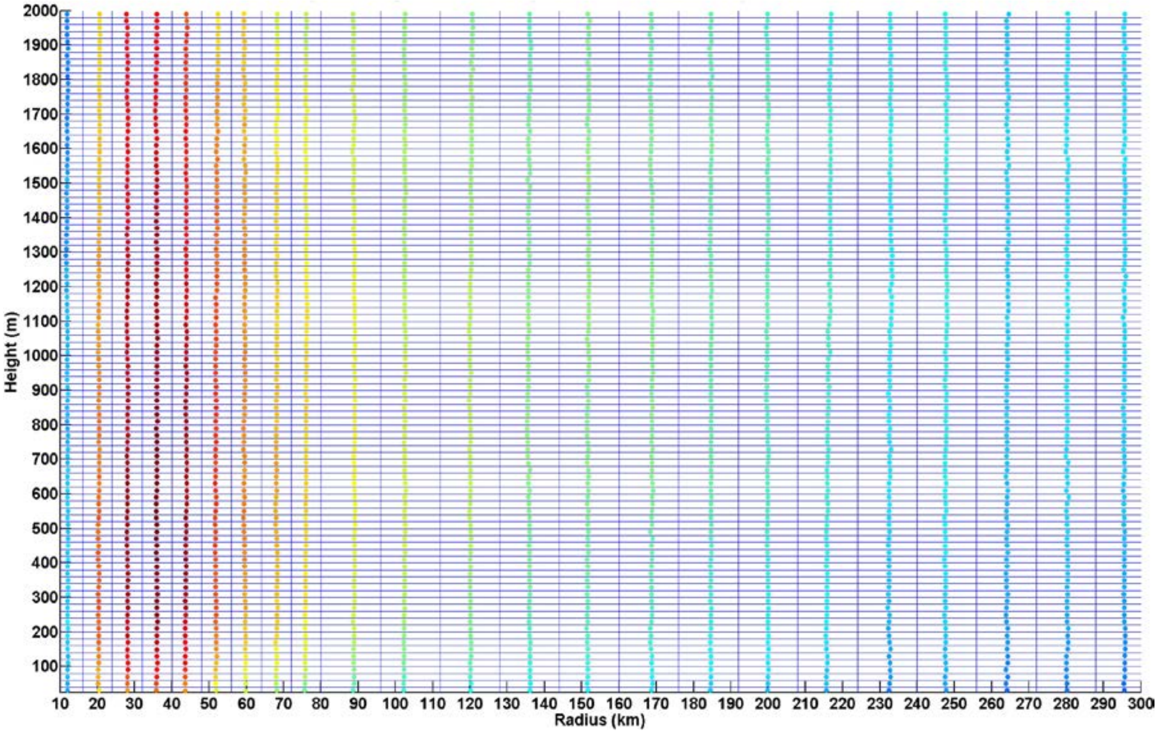

Figure 14. Visualization of the composite analysis technique applied to a discretized grid of non-uniform numerical bins. The blue lines identify bin boundaries selected by this study. Colored dots indicate the positions of mean physical quantities associated with each bin.

As a result, considerable effort was devoted to the selection of optimal bin dimensions. Starting from the values indicated by Z11, which were based on fractions of the radius of maximum wind (RMW), an effort was made to estimate the RMW for each observation in the master array of structures. As this information was not contained in the Long-Term NOAA Dropsonde Hurricane Archive or the HURDAT2 database, it was necessary to infer a suitable value from preliminary composite estimates of the total and tangential wind speeds. It should be noted that this discrepancy similarly prevented the normalization of the characteristic radius-height plots depicted in Z11. Nevertheless, a universal mean RMW of 40 km (Figure 15) was found to be consistent with the mean RMW identified by Z11.

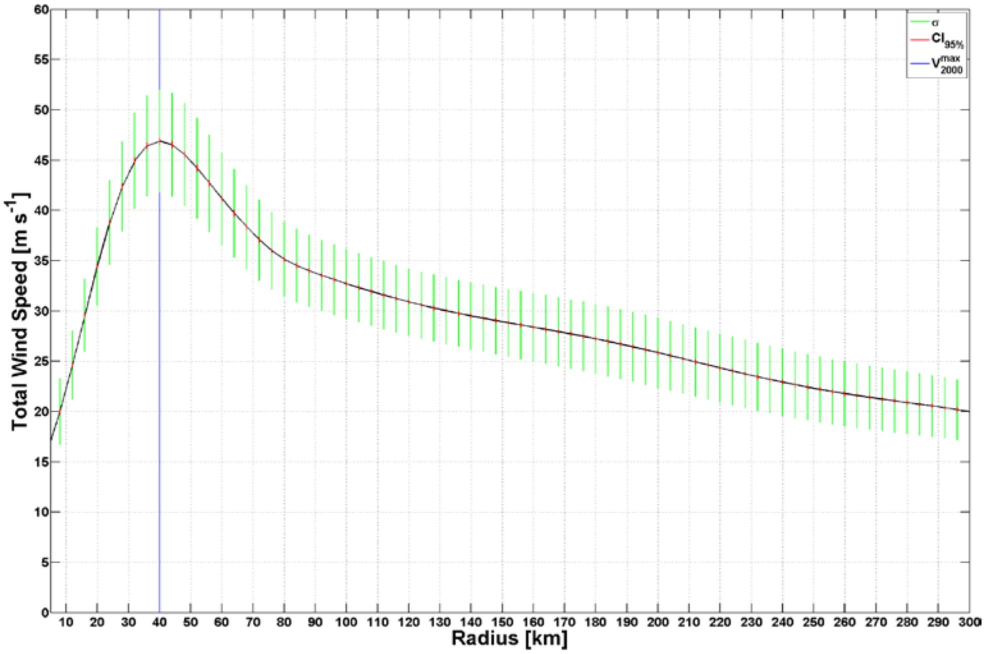

Figure 15. Composite analysis of the total wind speed vertically averaged from the surface to a height of 2000 m. The blue line indicates the radial position of the mean RMW. Green lines indicate the height of one standard deviation above and below the mean. Red lines indicate a 95% confidence interval for the standard error of the mean (SEM) based on a two-sided Student's t-distribution.

With basic data coherence established between Z11 and this study, and after considerable iteration, the boundary between the inner and outer core was placed at a radius of 80 km; that is, at twice the radius of the mean RMW: 40 km. Moreover, the final bin width was separated into two radial regimes that neatly coincided with Z11 values: 8 km (16 km) for the inner (outer) core. Taking the Z11 spacing as a starting point for bin heights, an initial value of 10 m was selected. However, the convolution of azimuthal and regional conditioning required larger bins to capture a statistically significant sample in the vertical dimension. Due to the non-uniform distribution of observations in the characteristic radius-height space of this study (Figure 16), increased vertical bin spacing was required to avoid anomalous composite analysis results. In particular, the enhanced vertical spacing attenuated erratic numerical smoothing behavior near the surface boundary. As a result, a final bin height of 20 m was chosen to optimize the tradeoff between resolution and uncertainty.

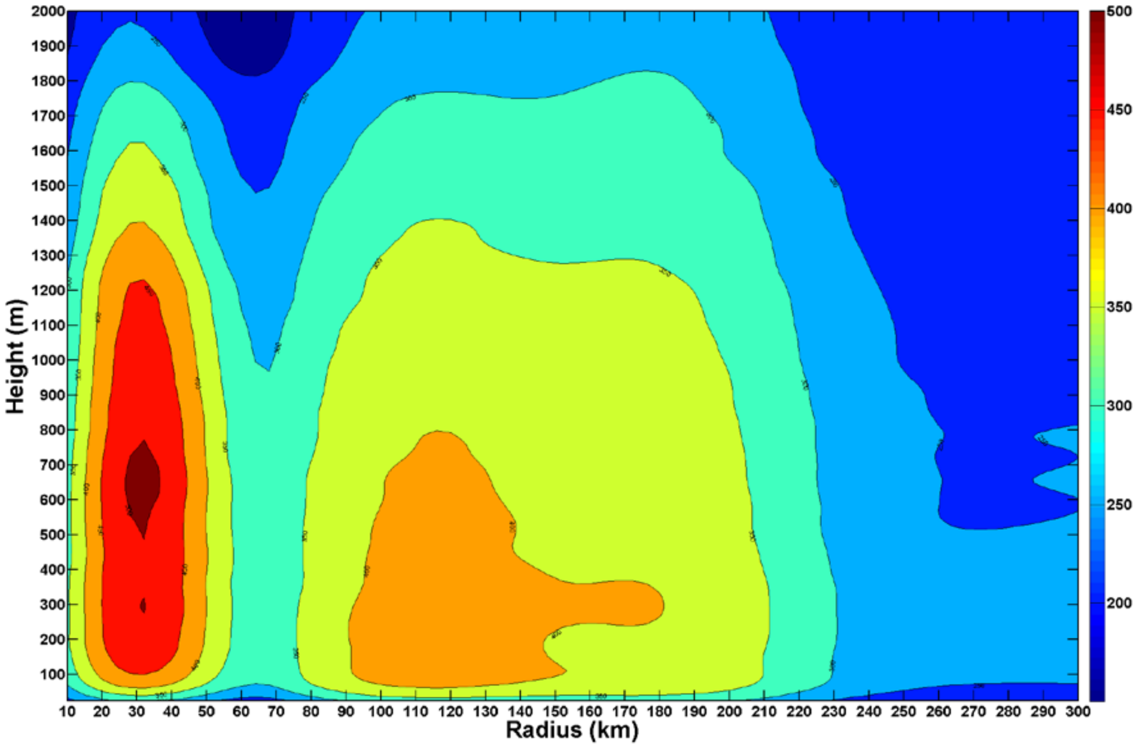

Figure 16. Composite analysis contour plot of the spatial distribution of data as a function of height and radius to the storm center. A radial bin spacing of 8 km (16 km) was used in the inner (outer) core; bins are separated by a vertical spacing of 20 m. Warmer contour colors indicate more data in each bin.

4. Data Smoothing

Two forms of numerical smoothing were applied in this thesis. Each utilized mathematical convolution to determine the moving average of an array or matrix. Through successive iterations, this process removes high frequency content from the binned data while preserving the bulk characteristics of the original series or image (MathWorks 2014a). For one-dimensional arrays, such as the height of maximum total or tangential wind speed, a standard 1-2-1 filter was selected (Figure 17a). For two-dimensional matrices, such as a filled contour plot of total wind speed, a modified 2-dimensional analog of the 1-2-1 filter (Figure 17c) was employed to simultaneously smooth the data horizontally, vertically, and diagonally.

$$\text{(a)}\ [1\ 2\ 1] \qquad \text{(b)} \begin{bmatrix} 0 & 1 & 0 \\ 1 & 2 & 1 \\ 0 & 1 & 0 \end{bmatrix} \qquad \text{(c)} \begin{bmatrix} 1 & 2 & 1 \\ 2 & 4 & 2 \\ 1 & 2 & 1 \end{bmatrix}$$

Figure 17. Representations of 1-2-1 convolution kernels used to smooth various composite analysis results. Kernel (a) was applied to all one-dimensional arrays; kernel (b) depicts a pure 1-2-1 filter extrapolated into two dimensions; kernel (c) is a custom modification to (b) that was applied to all two-dimensional matrices in this study.

In this way, each element of an array or matrix assumes the mean properties of its spatial neighbors; more specifically, each element is replaced by a linear combination of neighboring points whose coefficients are determined by the relative weights applied to each neighbor (Equation 3). Thus, a one-dimensional 1-2-1 filter provides an element with twice the importance of its nearest neighbors, so that its linear combination is disproportionally biased to reflect the original value of that element. Using the two-dimensional kernel in Figure 17c as an example, a point $y_{i,j}$ in an arbitrary composite analysis matrix would be smoothed in a linear combination as

$$16\, f_{i,j} = y_{i-1,j-1} + 2y_{i-1,j} + y_{i-1,j+1} + 2y_{i,j-1} + 4y_{i,j} + 2y_{i,j+1} + y_{i+1,j-1} + 2y_{i+1,j} + y_{i+1,j+1}, \quad (3)$$

where $f_{i,j}$ represents the smoothed value of point $y_{i,j}$ and the integer coefficients correspond to the elements of the specified convolution kernel. The sum of this kernel, which accounts for the multiplier of 16 to $f_{i,j}$, normalizes the linear combination to ensure the amplitude of the smoothed matrix is identical to the original. When this convolution process is moved across an arbitrary array or matrix, the moving average scheme is analytically realized.

High frequency content in digital imaging may produce noisy plots (Figure 18a) that obfuscate characteristic structures or meaningful variability in physical properties. By comparison, an image may be smoothed through successive applications of a convolution kernel to expose the presence of an important object or physical structure; in this case, a relative maximum in the total wind speed is revealed as the core of a boundary layer jet (Figure 18b). For these reasons, convolution smoothing was applied extensively throughout this study.

Each application of the filter acts on the cumulative results of the previous convolutions. For this study, most data structures were filtered five times; however, composite analysis results for boundary layer height, inflow layer depth, and virtual potential temperature lapse rate required an order of magnitude increase in the number of smoothing iterations.

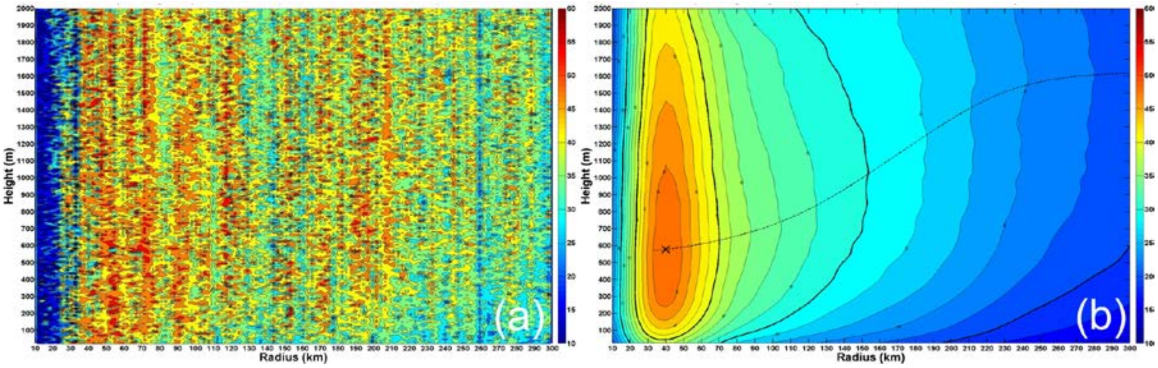

Figure 18. Comparison of an (a) unfiltered and (b) filtered composite analysis contour plot of total wind speed. The filtered image has been smoothed five times with a modified 1-2-1 moving average filter.

D. BOUNDARY LAYER HEIGHTS

Based on the methods outlined in S10, Z11, and D14, this thesis explicitly examined five definitions for hurricane boundary layer height. To further limit the scope of the spatial variability considered, the composite analysis plots of the characteristic radius-height space were chosen with a radial domain of 300 km and a vertical geopotential height range of 2000 m. In this way, the normalized radius-height representations from Z11 may be reasonably compared with the results produced by this study.

Two of the three dynamical boundary layer height estimates are focused on structural components of the primary hurricane circulation. In this way, the top of the hurricane boundary layer may be identified by the heights of the maximum total and tangential wind speeds, or h_{vmax} and h_{vtmax}, respectively (Table 3). Using the secondary hurricane circulation as a reference, the third dynamical definition specifies the height of the hurricane boundary layer in terms of the inflow layer depth (h_{infl}). Adopting the Z11 reference for consistency, this thesis defines the height of inflow layer in terms of the vertical decay of near-surface radial inflow; that is, the height at which the radial component of the total wind has fallen to 10% of its peak near-surface value.

Dynamical BLH Scales	**Variable/Definition**
Height of Maximum Total Wind Speed	h_{vmax}
Height of Maximum Tangential Wind Speed	h_{vtmax}
Inflow Layer Depth	h_{infl}

Table 3. Definition of dynamical boundary layer heights and their respective symbols.

This thesis also examines two thermodynamical definitions (Table 4) for boundary layer height following the methods used in Z11. While each relies on the identification of the mixed layer depth, a distinction is made in the physical properties used to diagnose vertical mixing in the atmosphere. The first method classifies the mixed layer depth in terms of the virtual potential temperature anomaly. In simple terms, the virtual potential temperature at the center of each bin is compared with the mean from the surface to a geopotential height of 150 m; when this difference exceeds 0.5 K, the mixed layer depth has been determined. The second thermodynamical method, by comparison, examines the lapse rate in the virtual potential temperature profile: 3 K km^{-1} establishes the top of the hurricane boundary layer.

Thermodynamical BLH Scales	**Variable/Definition**
Mixed Layer Depth: θ_v *anomaly*	$\theta_v - \overline{\theta_{v150}} = 0.5\ K$
Mixed Layer Depth: θ_v *lapse rate*	$\frac{d\theta_v}{dz} \geq 3\ K\ km^{-1}$

Table 4. Definition of thermodynamical boundary layer heights and their respective symbols.

While the Z11 investigation considered the bulk Richardson number in its summary of boundary layer variability, the radial behavior observed in this parameter was found to be incompatible with other definitions of boundary layer height (Z11). As a result, this thesis did not include the bulk Richardson number approach and focused on the radial variability of the remaining boundary layer height estimates.

IV. RESULTS

A. INTRODUCTION

The composite analysis results of this study are numerically expressed in filled two-dimensional contour plots of the boundary layer environment. In this way, the near-surface atmospheric properties of tropical cyclones are visualized in the characteristic radius-height space introduced by Z11. By comparison, boundary layer height scales are compared in traditional plots of radius-height space, where radial variability in the dynamical and thermodynamical estimates is emphasized within the context of two primary modes of data conditioning: regional and azimuthal. The corresponding research hypotheses are further examined through box plots to compare the radial distributions of each definition with relevant statistical properties.

With 6593 quality-controlled dropsondes, Figure 9 indicates that hurricanes represent 66% of the observations in the archive. As a result, and as a direct extension of Z11, which sought "to improve our understanding of the mean boundary layer structure in hurricanes in terms of the boundary layer height," this study focused exclusively on the boundary layer characteristics of hurricanes (Z11).

B. THE COMPOSITE HURRICANE

A composite analysis contour plot of total wind speed (Figure 19) defines the azimuthally and regionally averaged flow field inside of the hurricane boundary layer. Similar to the results obtained in Z11, a local maximum in total wind speed was found near a radius of 40 km and a geopotential height of 600 m. This region has been described as a boundary layer jet or "azimuthal jet" in related studies of the hurricane boundary layer (Z11). The core of this so-called boundary layer jet has a broad vertical extent from 250 m to geopotential heights above 1 km. By inspection only, the near-surface wind field has a significant vertical gradient that appears to be consistent with the canonical logarithmic profile of PBL flow (AMS 2014b). Also like Z11, the total wind speed contours deviate from the assumed logarithmic profile above the core of the boundary layer jet. That is, the flow field was qualitatively approximated by logarithmic decay at geopotential heights below 600 m.

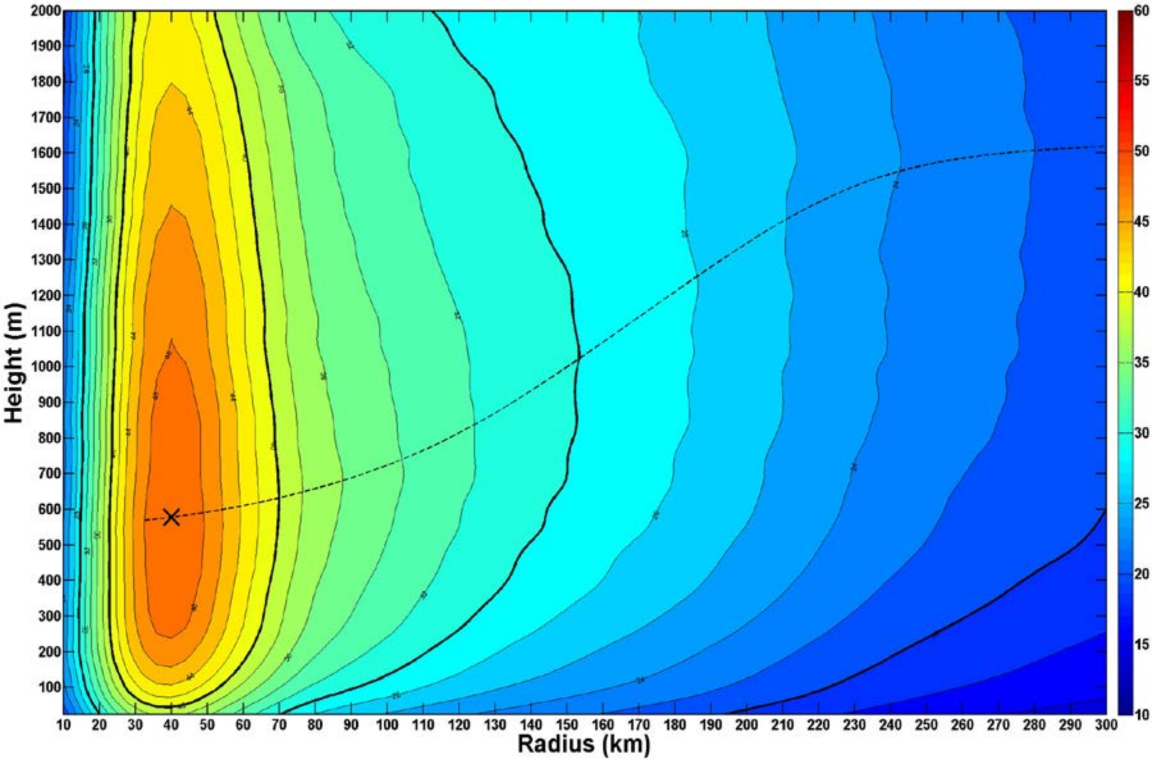

Figure 19. Composite analysis showing contours of total wind speed in 2 m s^{-1} increments. The black dashed line represents the height of the maximum total wind speed as a function of radius to the storm center. Thick black lines identify the 40, 30, and 20 m s^{-1} contours from left to right, respectively. A black "X" identifies the location of the absolute maximum total wind speed.

The radial variation of the height of the maximum total wind speed (h_{vmax}) is identified by the dashed vertical line in Figure 19. Representing the first dynamical estimate of boundary layer height, its smoothed inverse tangent appearance demonstrated a characteristic decrease in height with decreasing radius to the storm center. Similarly, the largest change in boundary layer height occurred near a radius of 150 km in the outer core of the composite hurricane.

Mueller et al. (2006) describes the dominance of the total wind field by the relative tangential winds. This suggests that the hurricane vortex is reasonably approximated by the tangential component of the total wind field. The composite analysis contour plot of relative tangential winds (Figure 20) was found to be consistent with this description, as it mirrored the structural characteristics of the total wind speed in Figure 19. Specifically, the boundary layer jet was again apparent as a contiguous region of enhanced winds between 250 m and 1200 m in the vertical. The decay of tangential winds below the core of the boundary layer jet, now elevated to a geopotential height of 650 m, was similarly evident. The height of the maximum tangential wind speed (h_{vtmax}), identified by the black dashed line, was found to be slightly higher than the equivalent line for total wind speed. When viewed as the second method of estimating the height of the hurricane boundary layer, the shape of this curve displayed an analogous decrease in height with decreasing radius.

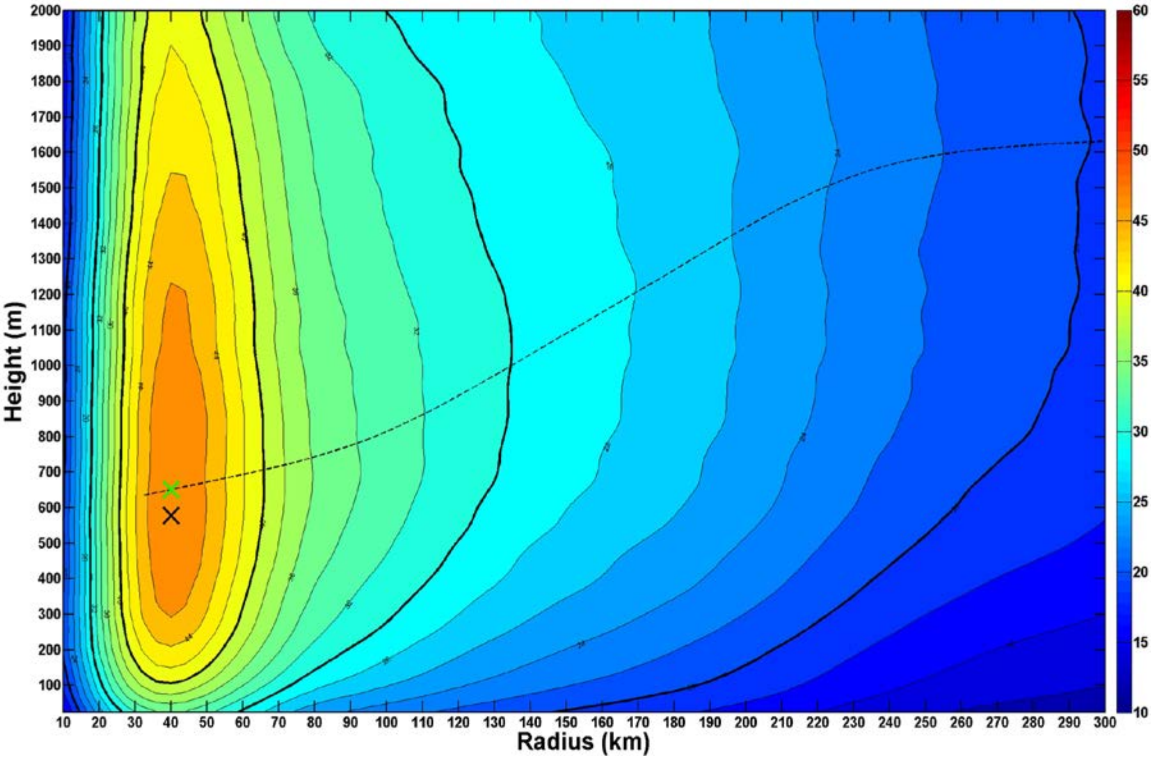

Figure 20. Composite analysis contour plot of relative tangential wind speed in 2 m s^{-1} increments. The black dashed line represents the height of the maximum tangential wind speed as a function of radius to the storm center. Thick black lines identify the 40, 30, and 20 m s^{-1} contours from left to right, respectively. A green (black) "X" identifies the location of the absolute maximum tangential (total) wind speed.

In their attempts to describe the wind field of an arbitrary tropical cyclone with infrared satellite imagery, Mueller et al. (2006) explored the modified Rankine vortex to model the flow structure of the canonical hurricane. The piecewise continuous function in the traditional Rankine vortex identifies an irrotational flow pattern in the free vortex region, where wind speed is inversely proportional to radius to the center of the storm, and rigid body motion for the forced vortex region inside of the radius of maximum tangential winds. However, this pattern is modified to allow for a modest departure from idealized irrotational flow in the free vortex region, so that the reduction in tangential wind speed with radius obeys an inverse power law relationship. This flow behavior is analytically expressed as

$$V\left(r\right)=\begin{cases} V_m\left(\dfrac{r}{R_m}\right), \mathrm{r} < \mathrm{R}_m \\ V_m\left(\dfrac{R_m}{r}\right)^x, \mathrm{r} > \mathrm{R}_m \end{cases}, \qquad (4)$$

where V is the tangential wind speed, V_m is the maximum tangential wind speed, R_m is the radius of maximum tangential wind speed, and x is a dimensionless parameter that describes the rate of free vortex decay (Mueller et al. 2006).

Previous attempts to model hurricane winds as a modified Rankine vortex have produced empirical estimates for the dimensionless size parameter x between 0.4 and 0.6. If a box plot of the geopotential height distribution of composite analysis tangential winds is compared to a modified Rankine vortex (Figure 21), these empirical results are reasonably confirmed. Each yellow box describes the statistical properties of the vertical distribution of relative tangential winds, so that the mean, median, and quartiles represent the magnitude of the primary circulation as a function of radius to the storm center. In specific terms, the mean and median of the vertical distribution of tangential winds at each discrete radius were found between the $x = 0.4$ and $x = 0.5$ curves. The $x = 0.5$ solution was particularly good between a radius of 40 km and 100 km, while the $x = 0.4$ curve was generally more accurate beyond 100 km. Similarly, the idealized rigid body flow of the forced vortex region, where winds are proportional to the radius, was well-described by the composite analysis tangential winds inside of 40 km. To this end, the modified Rankine vortex provides an adequate prediction of the composite analysis tangential wind field produced in this thesis.

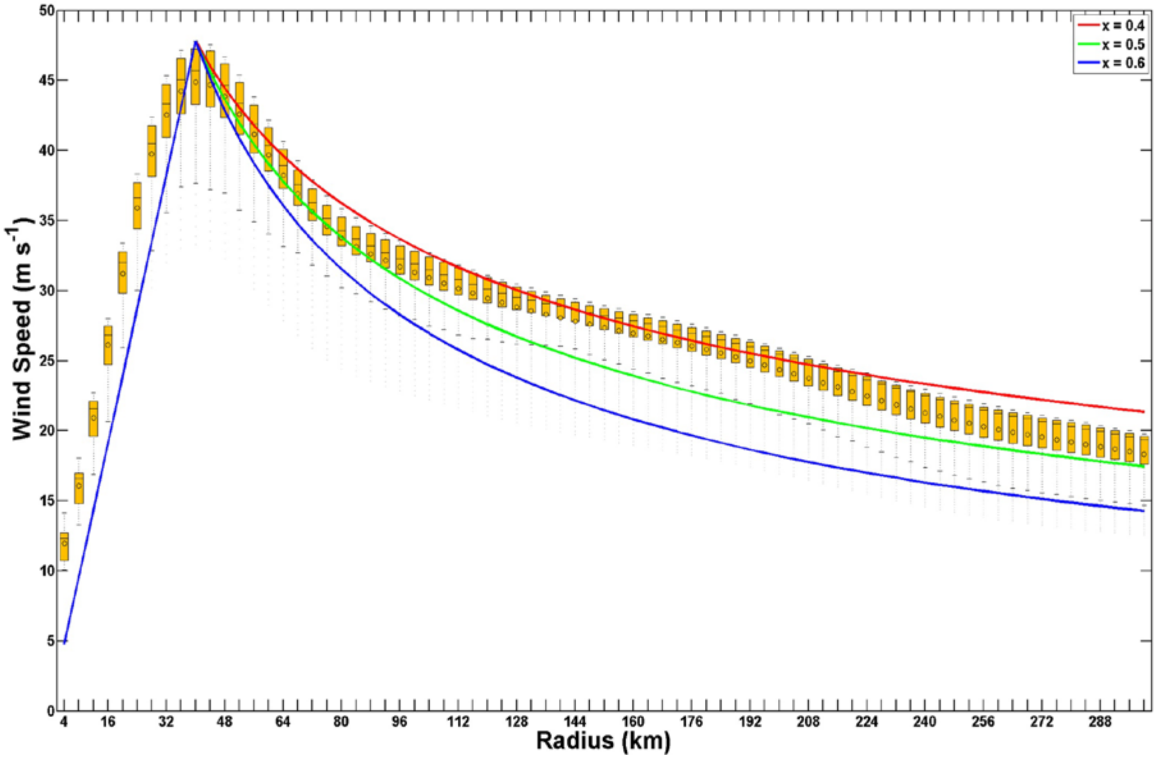

Figure 21. Composite analysis plot of relative tangential wind speed as a function of radius to the storm center. Orange box plots indicate the distribution of tangential winds in 4 km radial increments. The red, green, and blue lines identify modified Rankine vortex estimates of outer core tangential winds for dimensionless size parameters of 0.4, 0.5, and 0.6, respectively.

While smaller in magnitude than the tangential winds of the primary circulation, the relative radial winds associated with the secondary circulation are still important to the dynamical and thermodynamical properties of a hurricane. The composite analysis contour plot of relative radial winds (Figure 22) confirmed the presence of a lower magnitude wind field. Moreover, the flow was separated in distinct vertical regions of inflow at low levels and outflow above according to the sign of the radial winds. For this azimuthally and regionally averaged result, the boundary between the inflow and outflow was found in the inner core region at geopotential heights above 900m. In this way, the inflow region was larger and of higher magnitude within the composite analysis boundary layer, with an inflow layer depth (h_{infl}) that increased rapidly beyond a radius of 130 km. The core of this robust inflow layer was centered below 100 m at a radius of 70 km from the storm center.

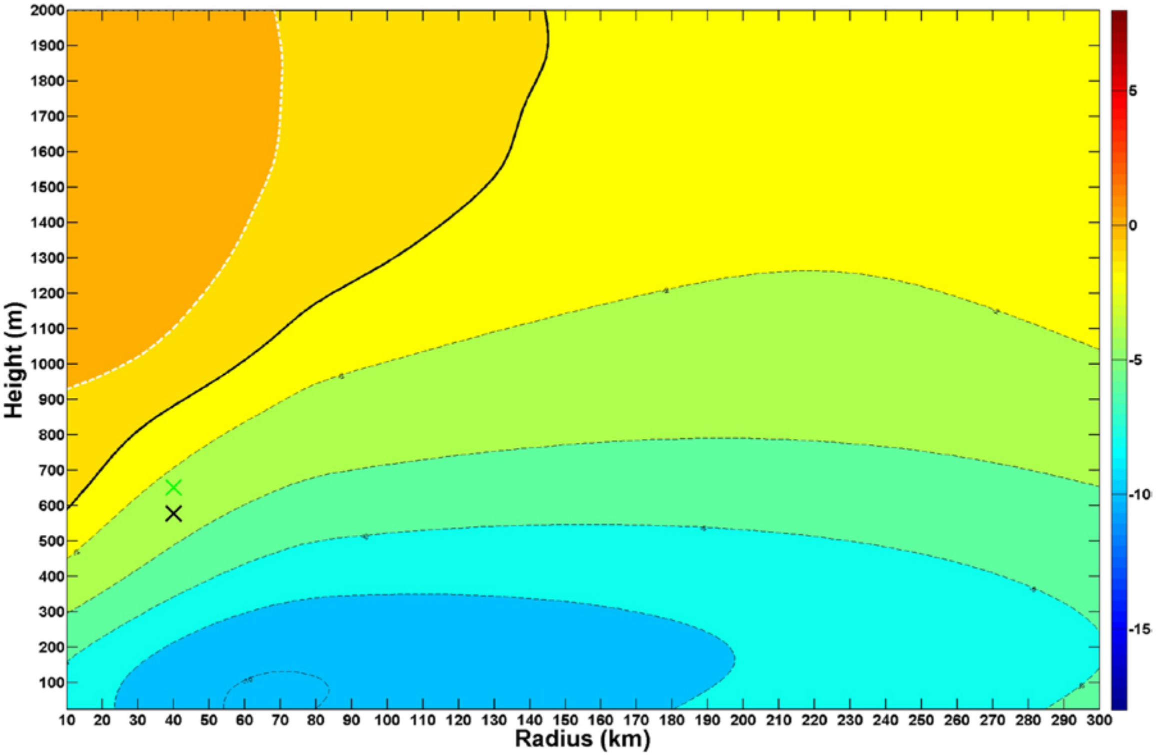

Figure 22. Composite analysis contour plot of the relative radial wind in 2 m s^{-1} increments. Negative values indicate inflow conditions. The solid black line represents the height of the inflow layer (h_{infl}) as a function of radius to the storm center. The white dashed line identifies the boundary between regions of inflow and outflow. A green (black) "X" identifies the location of the absolute maximum tangential (total) wind speed.

Congruent with the Z11 findings, the heights of the absolute maximum total and tangential wind speed, identified by the black and green "X", respectively, were found below h_{infl}. Moreover, the height of absolute maximum tangential wind speed corresponded to a radial velocity that was approximately 25% of the peak found within the inflow core. While demonstrating poor analytical behavior beyond r = 140 km, h_{infl} displayed a characteristic decrease in height with decreasing radius throughout much of the composite boundary layer. In contrast, Z11 results were comparatively well-behaved (i.e., no rapid increase in slope) and demonstrated a decrease in height with increasing radius for portions of the outer core region.

The composite analysis contour plot of virtual potential temperature (θ_v) revealed a characteristically warm region inside the inner core of the hurricane boundary layer (Figure 23). In particular, a pocket of warm air was found at radii less than the RMW and at geopotential heights above 1500 m. Moreover, an area of comparatively cold air and reduced vertical stratification was apparent below the 305 K θ_v contour near the center of the radius-height domain. These attributes are consistent with a well-mixed near-surface layer. An important trend in the radial distribution of θ_v was observed in the slope of θ_v contours on this radius-height plot. This result was consistent with the monotonically decreasing boundary layer radius-height relationship established thus far.

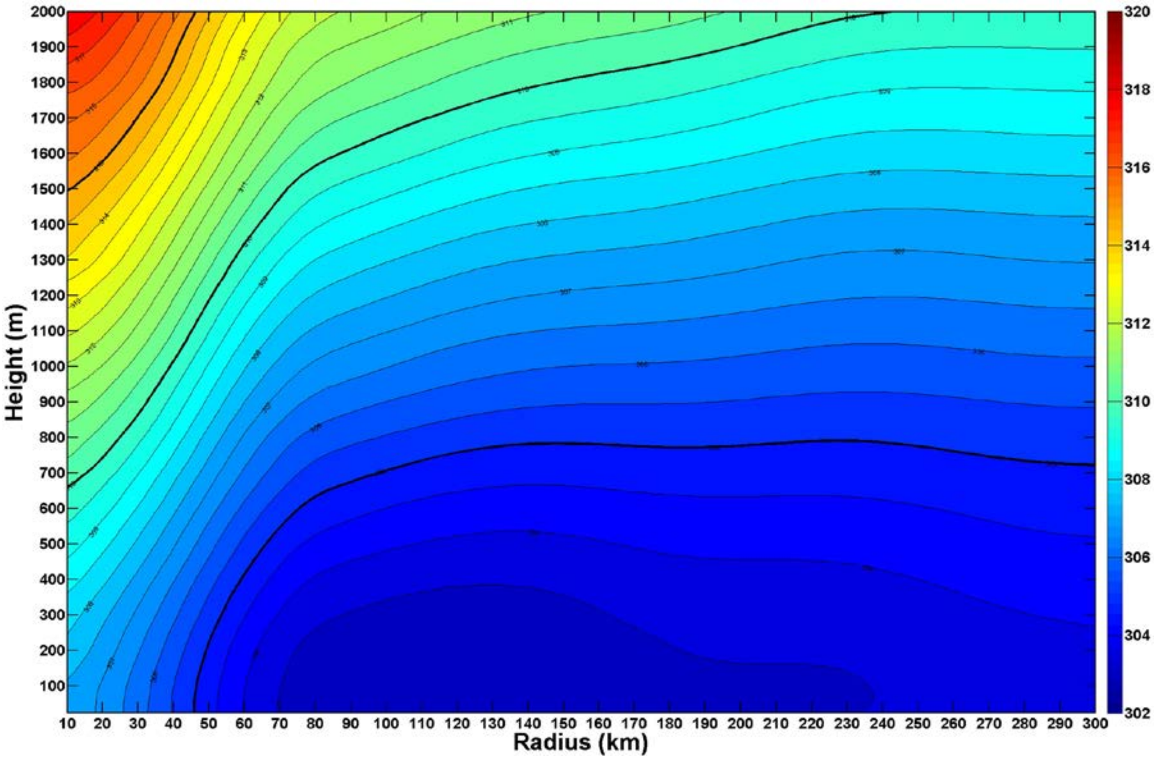

Figure 23. Composite analysis contour plot of virtual potential temperature (θ_v) in 0.5 K increments. Thick black lines identify the 315, 310, and 305 K contours from top-left to bottom-right, respectively. Warmer contour colors correspond to warmer θ_v regions.

The composite analysis contour plot of θ_v anomaly in Figure 24 provided the first thermodynamical method of estimating boundary layer height in this study. Representing the thermodynamic departure of the hurricane boundary layer from the mean θ_v in the lowest 150 m at each respective radius bin, it attempts to quantify the level of mixing present in the near-surface atmosphere. In this way, the mixed layer depth may be identified by the height of the 0.5 K contour as a function of radius, below which vertical stratification is assumed to be negligible. The slope of the mixed layer was also found to be small in comparison to the corresponding dynamical boundary layer height estimates. As described by Z11, the mixed layer was also quite shallow in the inner core region, with a mean geopotential height between 200 m and 300 m. The depth of the mixed layer in the outer core region was marginally higher, with a mean value between 300 m and 400 m; however, it also demonstrated a notable decay in slope beyond r = 200 km.

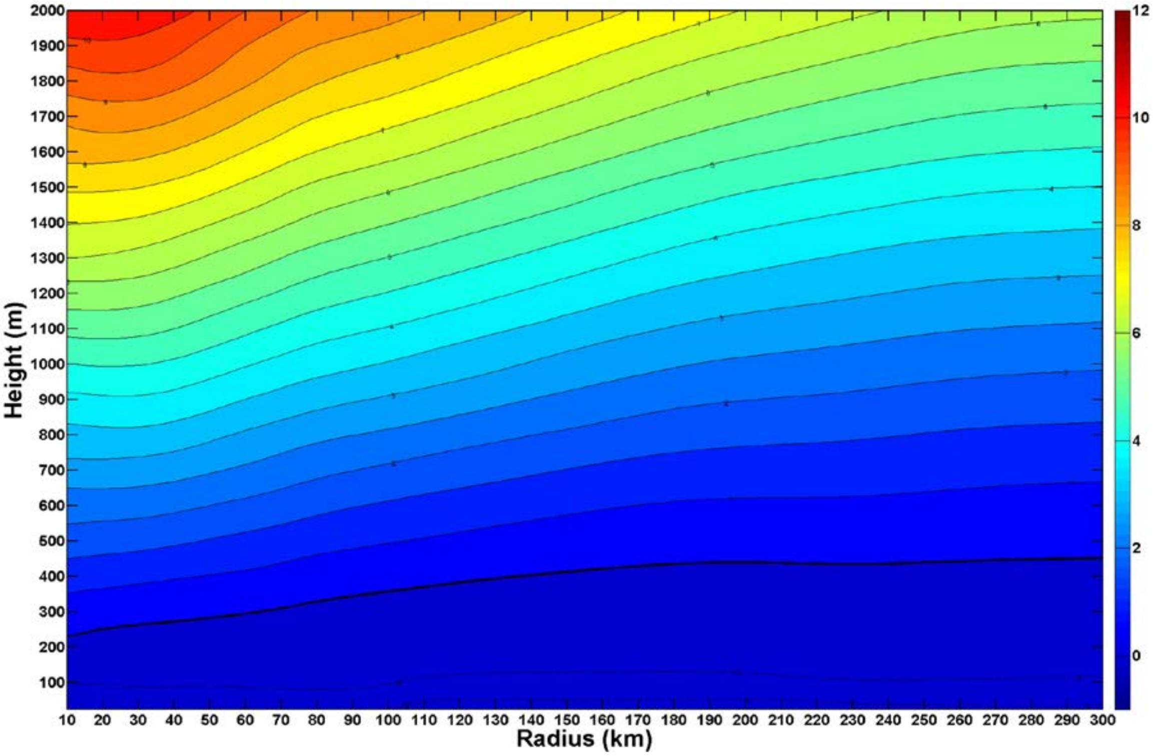

Figure 24. Composite analysis contour plot of virtual potential temperature anomaly in 0.5 K increments. The thick black line identifies the mixed layer depth based on temperature anomalies of 0.5 K or more. Warmer contour colors correspond to regions with larger θ_v anomalies.

By comparison, the composite analysis contour plot of θ_v lapse rate (Figure 25) demonstrated enhanced radial variability. Using the 3 K km^{-1} contour as a reference, the slope of the mixed layer depth was found to be notably larger. This correlated with a mixed layer depth that was shallower in the inner core region, sinking as low as 200 m near the RMW, and deeper in the out core region, exceeding 700 m beyond a radius of 270 km. Similar to the composite analysis contour plot of θ_v anomaly, and the results obtained by Z11, the contour plot of θ_v lapse rate produced a mixed layer that decreased in height with decreasing radius. Nevertheless, a meaningful distinction in boundary layer height estimates emerged: while generally deeper than the θ_v anomaly estimate, the composite analysis contour plot of θ_v lapse rate produced a comparatively shallow mixed layer that fell well below the mean geopotential heights of corresponding dynamical definitions.

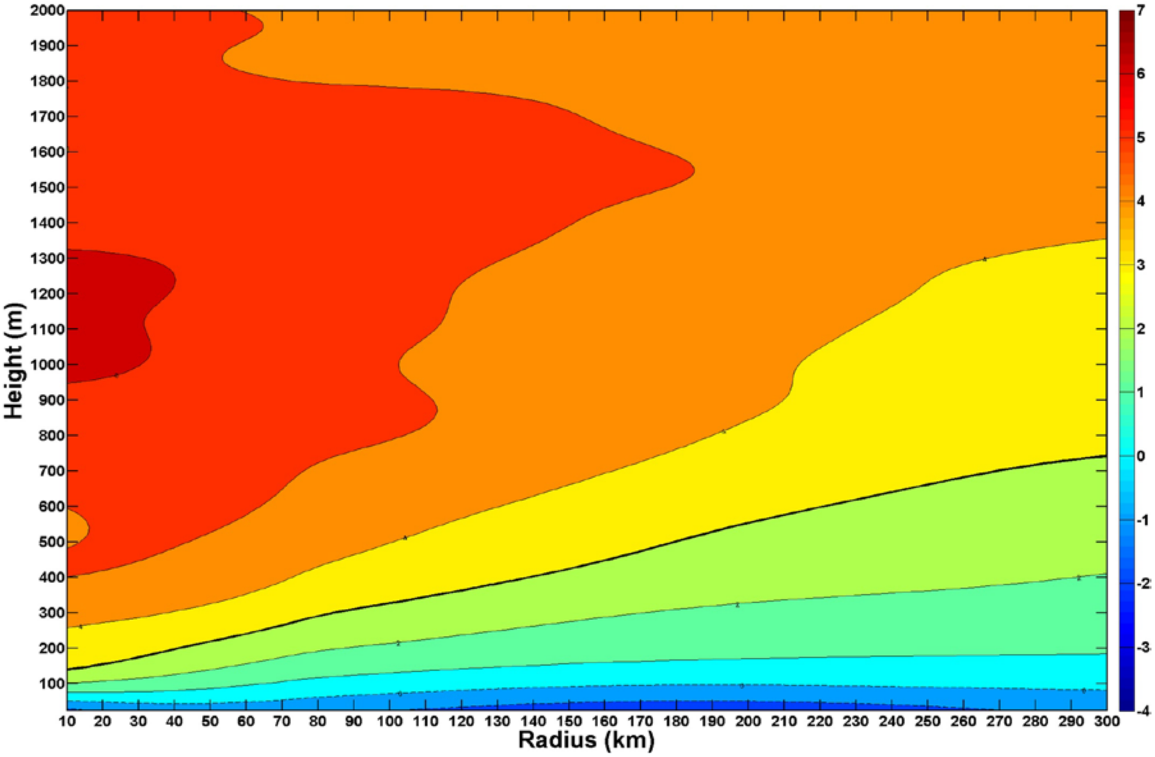

Figure 25. Composite analysis contour plot of virtual potential temperature lapse rate in 1 K increments. The thick black line identifies the mixed layer depth on the 3 K contour. Warmer contour colors correspond to regions with a larger θ_v lapse rate.

A summary of the composite analysis boundary layer height estimates (Figure 26) confirmed the aforementioned distinction between dynamical and thermodynamical definitions. Specifically, the three dynamical methods were found to have a mean geopotential height above 1 km. The two thermodynamical estimates, by comparison, had a mean geopotential height below 500 m. The maximum thermodynamical height estimate, which narrowly exceeded 700 m at *r* = 300 km, was only slightly higher than the minimum dynamical height of 575 m observed near the RMW. While each method demonstrated decreasing boundary layer height with decreasing radius, the radial variability demonstrated by the dynamical methods was notably larger. This was particularly true for h_{infl}, where the rapid increase in slope beyond *r* = 130 m complicated analytical comparisons in the outer core region and, more importantly, demonstrated the limitations of using h_{infl} to define boundary layer height in the hurricane environment.

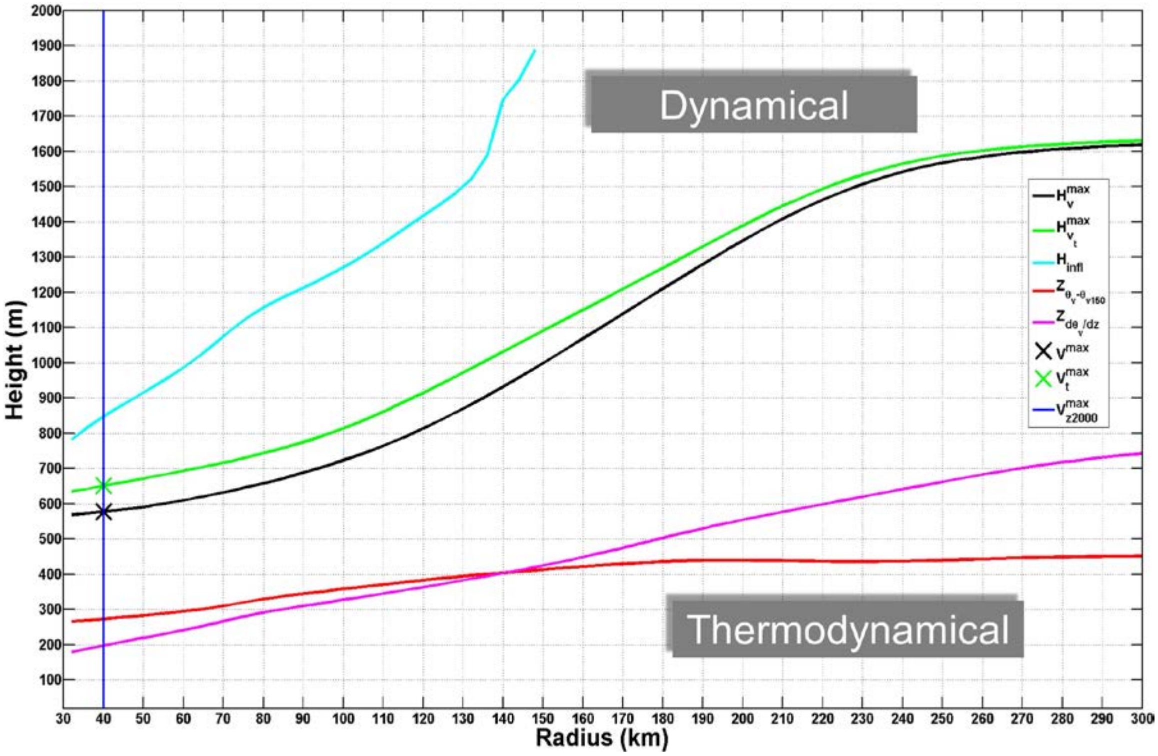

Figure 26. Composite analysis of hurricane boundary layer heights as defined in Figures 19-25. Line colors: black – h_{vmax}, green – h_{vtmax}, cyan – h_{infl}, red – θ_v anomaly, magenta – θ_v lapse rate. A green (black) "X" identifies the location of the absolute maximum tangential (total) wind speed. The thick blue line identifies the RMW.

These composite analysis results hint at a shallow mixed layer, particularly in the inner core region, that increases gradually with increasing radius from the storm center. The θ_v lapse rate produced a deeper mixed layer in the outer core region, where a maximum geopotential height disparity of nearly 300 m was observed relative to the θ_v anomaly. The differences in depth between h_{vmax} and h_{vtmax} are less than 100 m and decreased in the outer core region. However, the mean RMW estimates provided by the total and tangential wind fields were identical at 40 km.

The statistical properties of each boundary layer height definition were explored in greater detail with enhanced box plots (Figure 27). The median of each dynamical estimate was found to be well above the third quartiles of the thermodynamical estimates, emphasizing the distinction in height schemes originally identified in Z11. This height disparity was also observed in the azimuthally and regionally conditioned results.

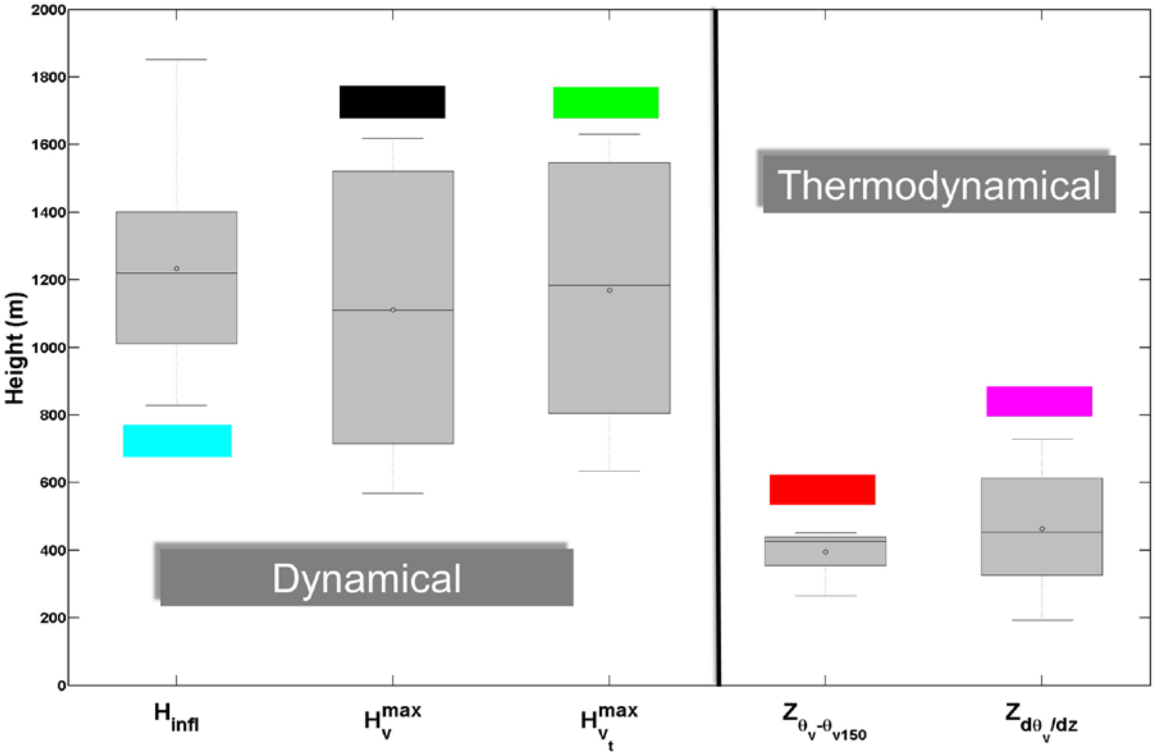

Figure 27. Composite analysis box plot comparisons of results from five boundary layer height definitions. Dynamical (thermodynamical) height estimates are identified on the left (right) side of the plot. Color-coded rectangles link each box plot with its equivalent curve in Figure 26.

The radial variability apparent in Figure 26 was quantified by the range and interquartile range (IQR) of each box plot in Figure 27. In particular, the dynamical height scales have characteristically large ranges, while h_{vmax} and h_{vtmax} have substantial IQRs. No clear skewness was present by simple inspection, and the rapid increase in h_{infl} slope was consistent with the long whisker above the third quartile. Finally, the box plots for θ_v anomaly and θ_v lapse rate were unique for their comparatively low medians and small IQRs, as indicated by the locations of the first and third quartiles and whiskers.

1. Azimuthal Boundary Layer Variability

By conditioning the unified dataset to express azimuthal modes of variability, the unique boundary layer characteristics of storm-relative quadrants and semicircles may be examined in more detail. Composite analysis contour plots of total wind speed were isolated for the left-front, right-front, left-rear, and right-rear quadrants (Figure 28) to investigate the distribution of winds around the canonical hurricane vortex. As expected, the enhanced intensity of the boundary layer jet was observed in the right-front and right-rear quadrants. The boundary layer jet in the right-front quadrant was particular large and potent, with a vertical extent that reached above a geopotential height of 1200 m and a peak intensity over 52 m s^{-1}. By comparison, the core of the boundary layer jet in left-rear quadrant barely exceeded a geopotential height of 900 m and a peak intensity of 44 m s^{-1}.

Using the black dashed line to identify the height of the maximum total wind speed (h_{vmax}), the quadrants in the right semicircle displayed a monotonically decreasing h_{vmax} with decreasing radius; however, the left semicircle quadrants demonstrated a characteristic decrease in h_{vmax} with increasing radius beyond r = 230 km. Similarly, the mean height and radial variability of the left semicircle h_{vmax} estimates were found to be consistent with one another. Breaking from this trend, the right-rear quadrant produced a unique h_{vmax} signature that was both shallow and flat when compared with the other three storm-relative quadrants. Moreover, the small amount of radial variability in the right-rear quadrant h_{vmax} was isolated between the inner-outer core boundary (i.e., at r = 80 km) and a radius of 150 km from the universal storm center.

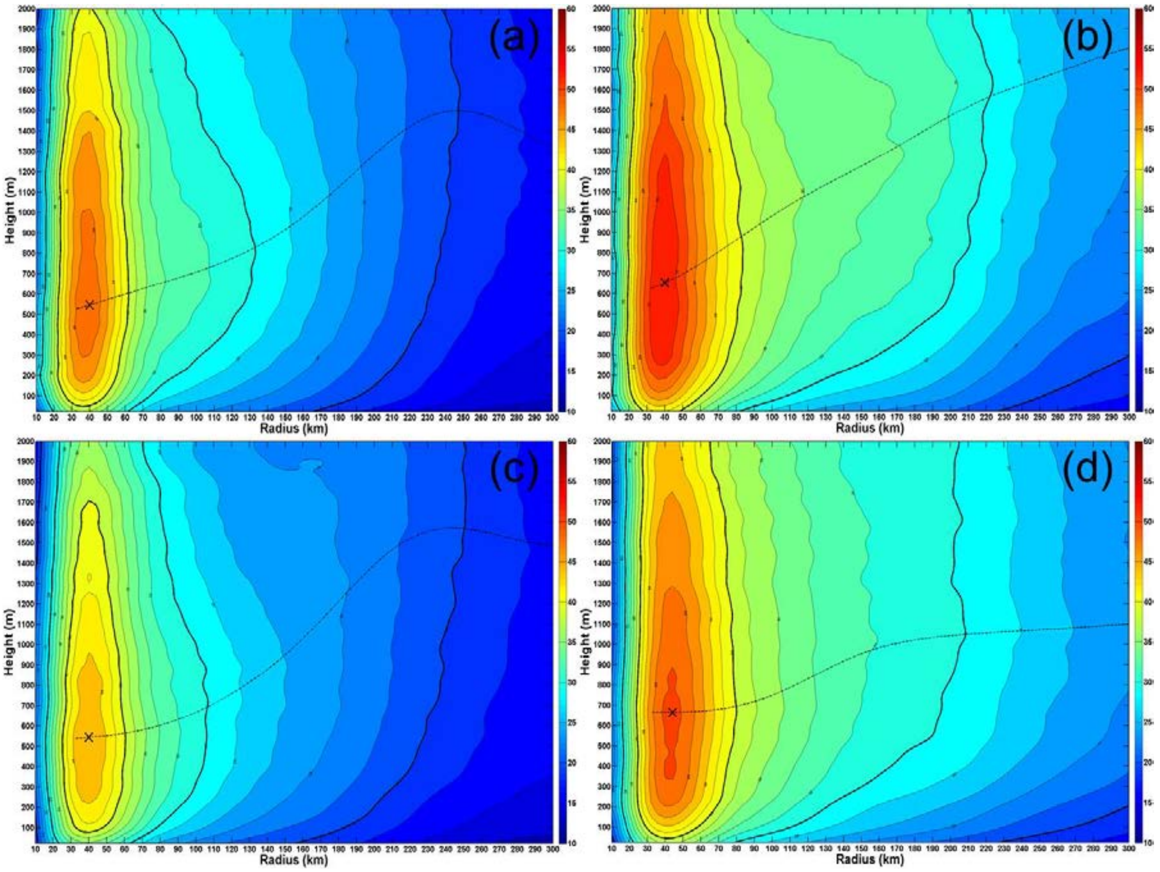

Figure 28. Composite analysis contour plots of the total wind speed in 2 m s^{-1} increments for the (a) left-front, (b) right-front, (c) left-rear, and (d) right-rear quadrants. Black dashed lines represent the height of the maximum total wind speed as a function of radius to the storm center. Thick black lines identify the 40, 30, and 20 m s^{-1} contours from left to right, respectively. A black "X" identifies the location of the absolute maximum total wind speed.

A similar examination of composite analysis contour plots of relative radial winds and, by extension, inflow layer depths (Figure 29) revealed new modes of azimuthal variability. The maximum boundary layer inflow occurred over the right quadrants centered near a geopotential height of 100 m. While the left-front quadrant exhibited a similar inflow structure, the magnitude of the peak near-surface inflow was smaller. The left-rear quadrant contained even less near-surface inflow and produced almost no boundary layer outflow beyond the inner core region. Reflecting the influence of comparatively robust areas of boundary layer outflow, the front semicircle quadrants produced h_{infl} contours that were analytically well-behaved over the entire domain of radial values. By comparison, the rear semicircle quadrants produced irregular h_{infl} contours with poorly defined or discontinuous areas of boundary layer outflow.

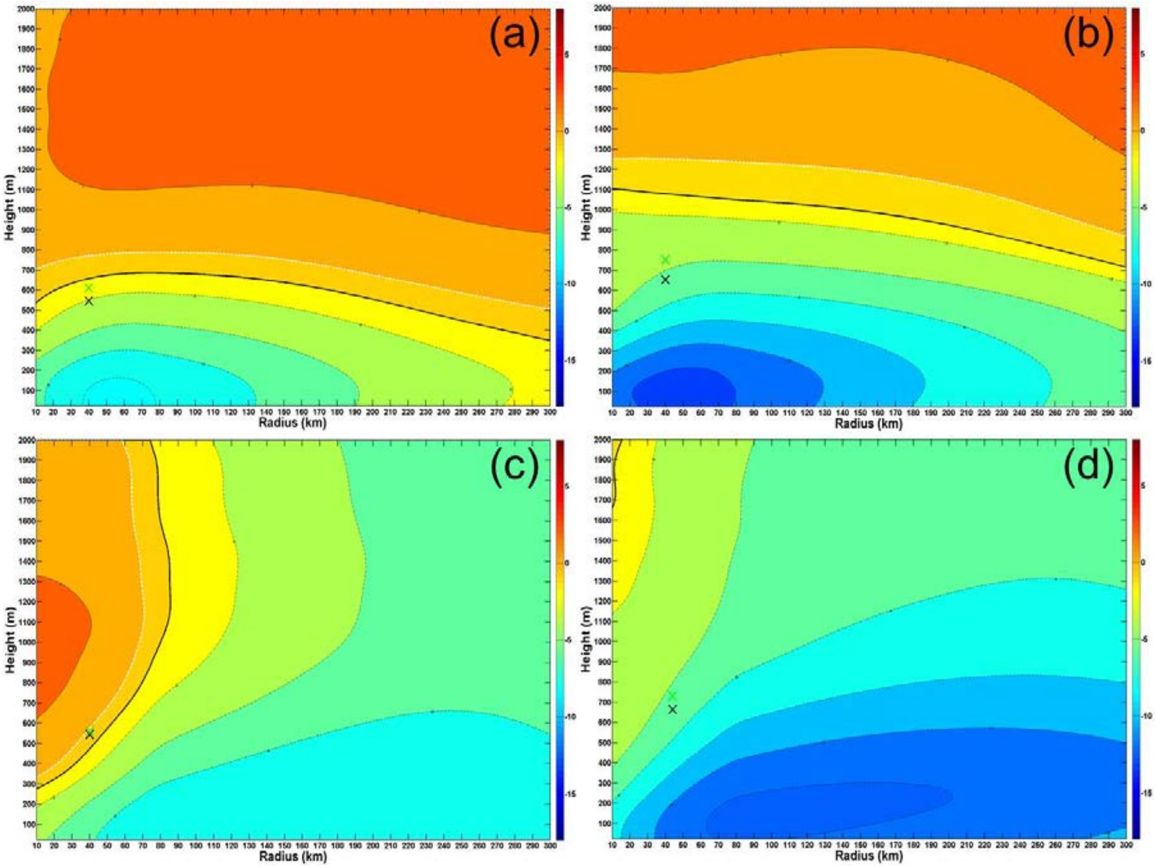

Figure 29. Composite analysis contour plots of the relative radial wind speed in 2 m s^{-1} increments for the (a) left-front, (b) right-front, (c) left-rear, and (d) right-rear quadrants. Thick black lines represent the height of the inflow layer (h_{infl}) as a function of radius to the storm center. White dashed lines identify the boundaries between areas of inflow and outflow. A green (black) "X" identifies the location of the absolute maximum tangential (total) wind speed.

As with the Z11 study, the azimuthally averaged results (Figure 22) produced inflow layer depths that were universally above the heights of the absolute maximum total and tangential wind speeds, as indicated by the black and green "X", respectively. However, the azimuthal conditioning in Figure 29 demonstrated that this relationship did not always hold. In particular, the inflow layer depth was found below the heights of the absolute maximum total and tangential wind speeds in the left-rear quadrant (Figure 29c).

Demonstrating additional disagreement with Z11, the maximum tangential wind speed in the left-front quadrant was not found at the height where inflow had decayed to 25% of its peak near-surface.

A similar analysis of virtual potential temperature (Figure 30) revealed only one major variation by quadrant. While all quadrants produced warm signatures for the inner core region, which is consistent with the thermodynamic properties of tropical cyclones, the right-front quadrant demonstrated an anomalous outward shift in the radial distribution of warmest virtual potential temperatures. This thesis was unable to determine the cause of the displacement or, similarly, distinguish its physical relevance.

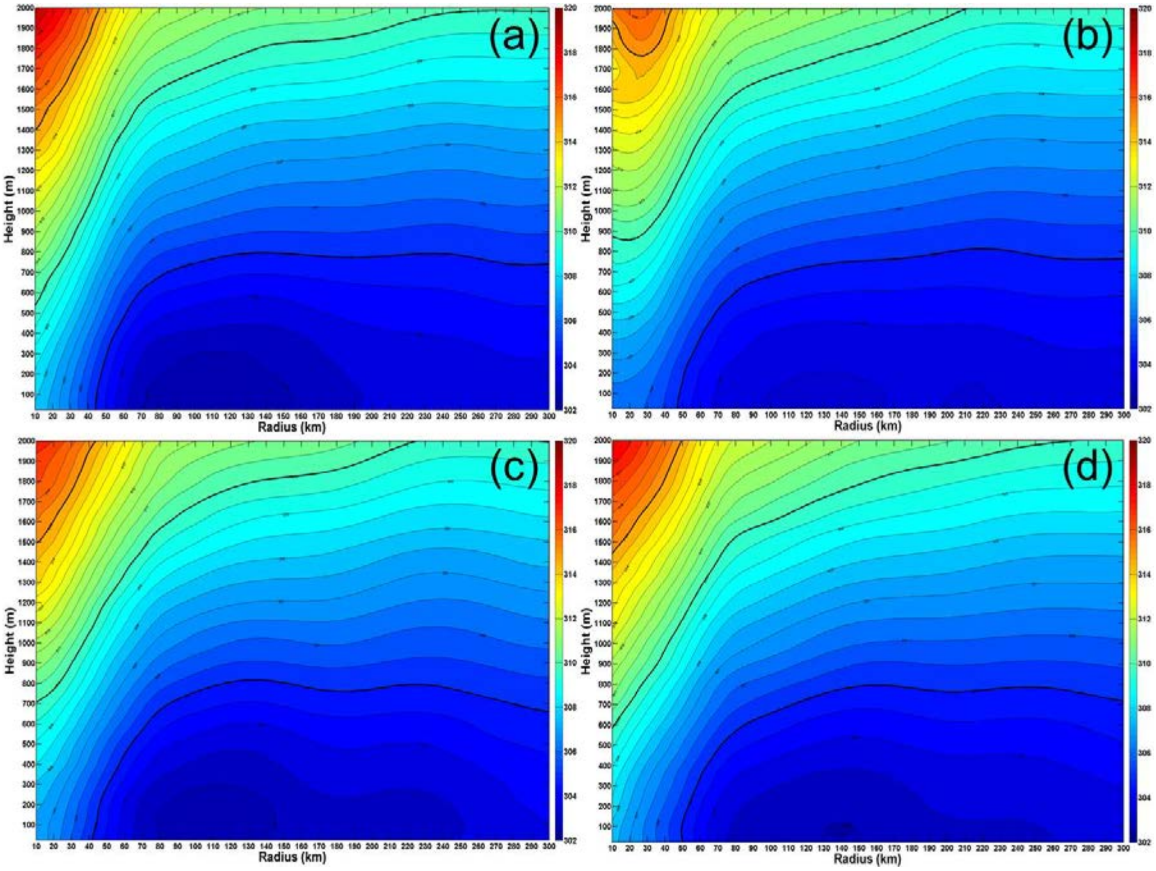

Figure 30. Composite analysis contour plots of virtual potential temperature in 0.5 K increments for the (a) front-left, (b) front-right, (c) rear-left, and (d) rear-right quadrants. Thick black lines identify the 315, 310, and 305 K contours from top-left to bottom-right, respectively. Warmer contour colors correspond to warmer θ_v areas.

A comparison of composite analysis boundary layer heights, as originally considered by Z11, produced meaningful results in the context of azimuthal conditioning (Figure 31). To begin, the thermodynamical estimates demonstrated no significant azimuthal variability. That is, the mixed layer was found to be nearly axisymmetric in its depth and slope, with only the aforementioned geopotential height disparities in the outer core region distinguishing the θ_v anomaly and θ_v lapse rate definitions. While inconsistent in the rear semicircle quadrants, h_{infl} was shallow enough to be found among the thermodynamical estimates in the outer core region. This was particularly true for the left-front quadrant, where h_{infl} was the most shallow estimate beyond r = 250 km.

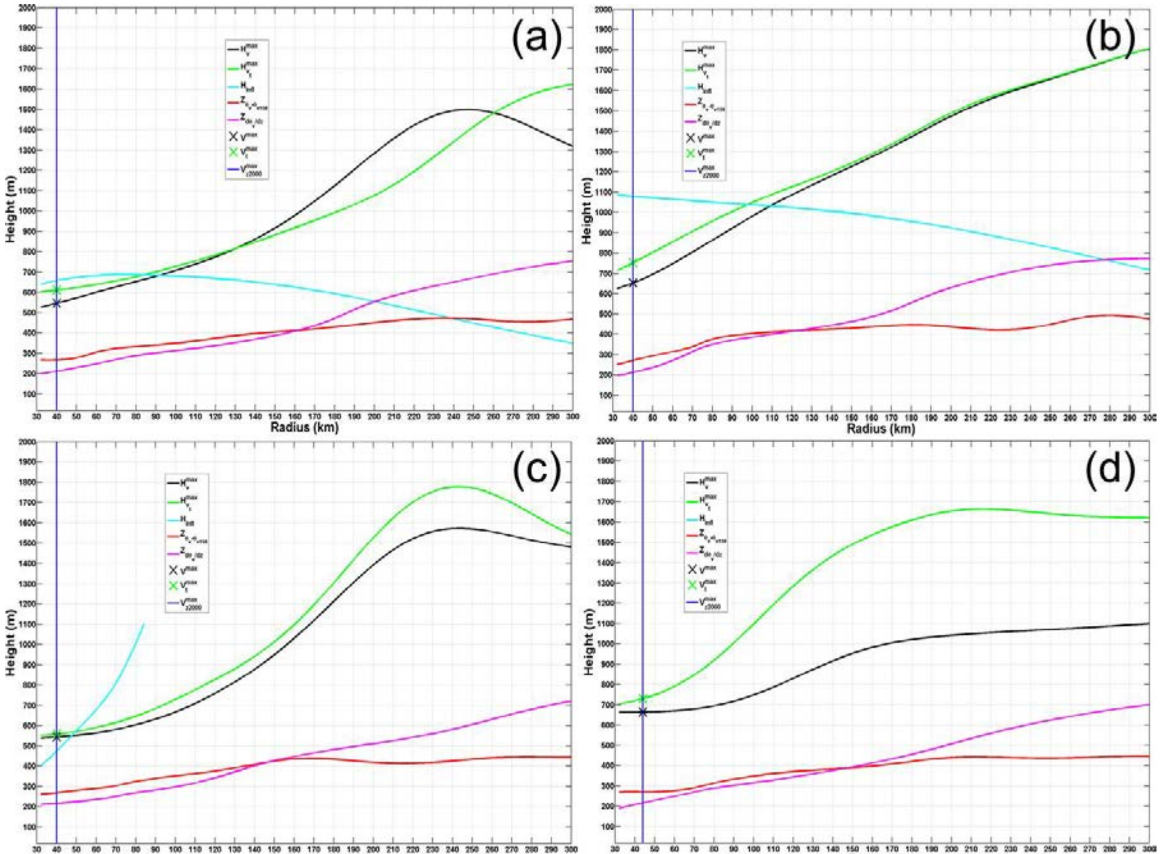

Figure 31. Composite analysis plot of hurricane boundary layer heights for the (a) front-left, (b) front-right, (c) rear-left, and (d) rear-right quadrants. Line colors: black – h_{vmax}, green – h_{vtmax}, cyan – h_{infl}, red – θ_v anomaly, magenta – θ_v lapse rate. A green (black) "X" identifies the location of the absolute maximum tangential (total) wind speed. A thick blue line identifies the RMW.

A closer examination of h_{vmax} and h_{vtmax} revealed a nearly axisymmetric distribution in the height of maximum total and tangential winds. The aforementioned left semicircle, outer core decrease in h_{vmax} and h_{vtmax} notwithstanding, the two boundary layer height estimates were generally identical throughout the hurricane vortex. However, the left-rear quadrant represented a key exception to this trend; the h_{vtmax} contour was well above the relatively flat h_{vmax} solution and was consistent with the h_{vmax} and h_{vtmax} estimates in other quadrants. Finally, this right-rear quadrant produced the only azimuthally conditioned mean RMW estimate larger than 40 km.

2. Boundary Layer Variability by Geographic Region

The unified data was also conditioned to express regional modes of hurricane boundary layer variability. In this way, this study sought out meaningful differences in the atmospheric properties of hurricanes found in various North Atlantic subregions. Removing the MDR, STL, and EPAC subregions from consideration due to small sample sizes, composite analysis contour plots of azimuthally averaged total wind speed were compared for the GOM, ECN, CRB, and ECS subregions (Figure 32). While the boundary layer jet is present in all four subregions, the GOM and ECS contained the largest and most intense core features. The magnitude of boundary layer jet winds in the ECS subregion was larger than any other subregion, with peak winds over 52 m s^{-1} and a maximum geopotential height near 1300 m. By comparison, maximum winds in storms over the ECN and CRB subregions struggled to exceed a peak intensity of 40 m s^{-1}or reach geopotential heights above 1 km.

The behavior of the h_{vmax} contours was similarly distributed, with the GOM and ECN estimates producing a characteristic decrease in boundary layer height with decreasing radius throughout the domain. Conversely, the ECN and CRB subregions depicted a local maximum boundary layer height in the outer core region near a geopotential altitude of 1700 m. Moreover, these outer core maximum boundary layer heights exceeded their corresponding values for the GOM and ECS subregions. Due to several iterations of numerical smoothing, the locations of the absolute maximum total wind speed were decoupled from their filled contour regions. After correcting for this artificial discrepancy, the geopotential height of each jet core was found between 500 m and 550 m.

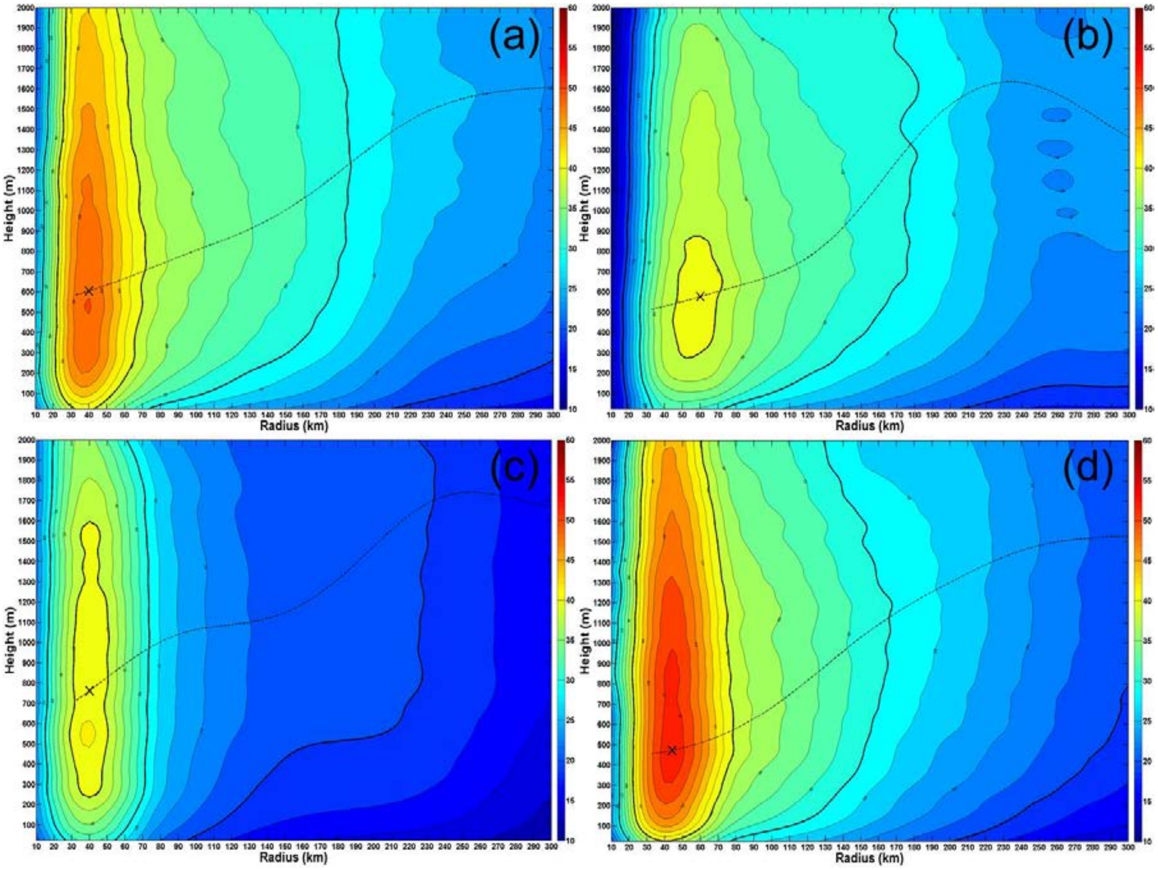

Figure 32. Composite analysis contour plots of the azimuthally averaged total wind speed in 2 m s^{-1} increments for the (a) GOM, (b) ECN, (c) CRB, and (d) ECS subregions. Black dashed lines represent the height of the maximum total wind speed as a function of radius to the storm center. Thick black lines identify the 40, 30, and 20 m s^{-1} contours from left to right, respectively. A black "X" identifies the location of the absolute maximum total wind speed.

The composite analysis contour plots of azimuthally averaged relative radial winds (Figure 33) depicted anomalous inflow layer depths for the GOM, CRB, and ECS subregions. Specifically, the h_{infl} contours for these subregions experienced rapid departures from the typical hurricane boundary layer height profile; that is, well-behaved, monotonically decreasing heights with decreasing radius. Nevertheless, the GOM and CRB subregions demonstrated elevated inflow layer depths throughout much of the outer core region. By comparison, the ECN subregion produced an inflow layer depth similar to the front semicircle quadrants in the azimuthal mode of conditioning.

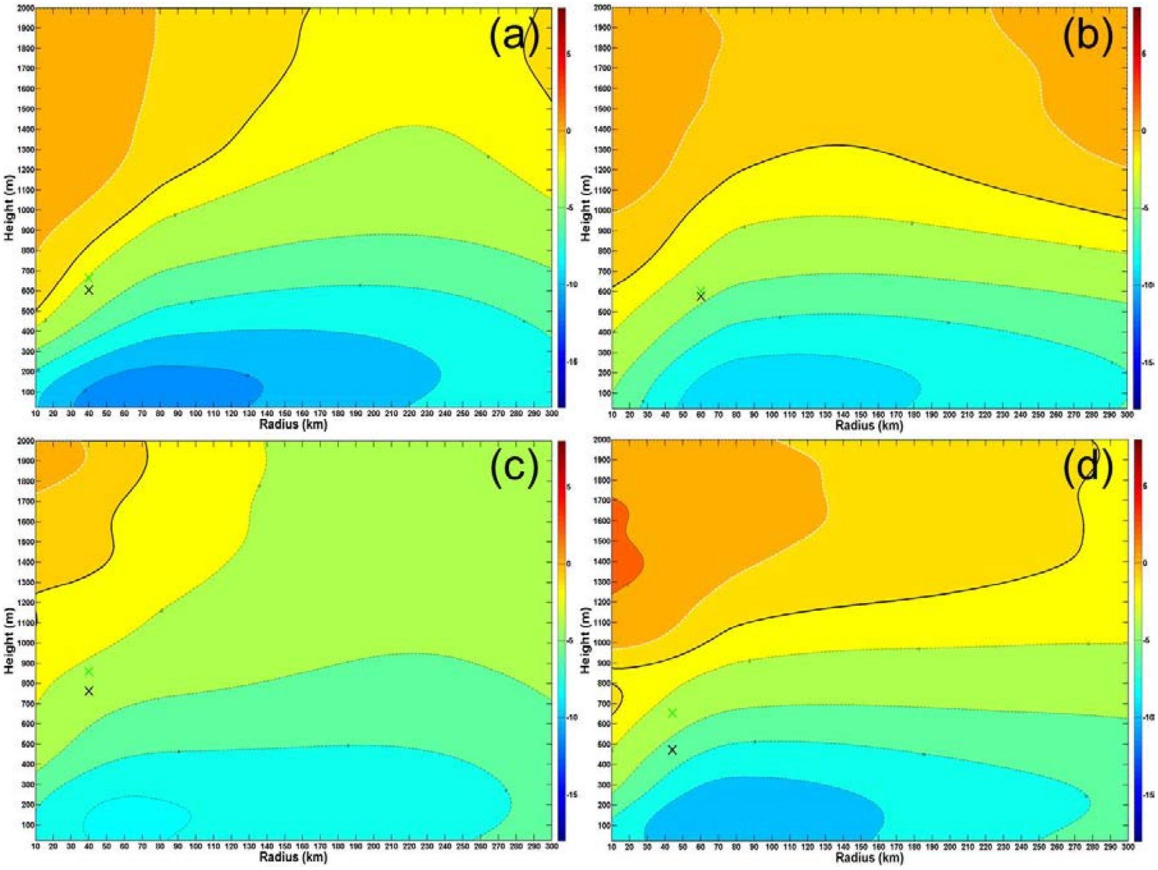

Figure 33. Composite analysis contour plots of the azimuthally averaged relative radial wind speed in 2 m s^{-1} increments for the (a) GOM, (b) ECN, (c) CRB, and (d) ECS subregions. Thick black lines represent the height of the inflow layer (h_{infl}) as a function of radius to the storm center. White dashed lines identify the boundaries between areas of inflow and outflow. A green (black) “X” identifies the location of the absolute maximum tangential (total) wind speed.

Similar to the azimuthal mode of variability, h_{infl} contours in Figure 33 did not necessarily follow the height ratio identified by Z11. That is, the height of the maximum tangential wind speed was not strictly coincident with the height at which the inflow had decayed to 25% of its peak near-surface value. While the heights of the maximum total and tangential wind speed were found below the inflow layer depth, relationships between peak core speed and inflow layer stratification were not sufficiently consistent to verify the Z11 findings in every subregion considered by this study.

Excluding irregularities in the inflow layer depth, the boundary layer height definitions examined in this study demonstrated no significant regional dependence (Figure 34). Similar to the azimuthal mode of conditioning, the two thermodynamical methods were nearly uniform in their radial variability. While the heights of the absolute maximum total and tangential wind speed did vary between the subregions, as indicated by the black and green "X", respectively, no discernable pattern was recognized. However, the location of the mean RMW did express meaningful regional dependence.

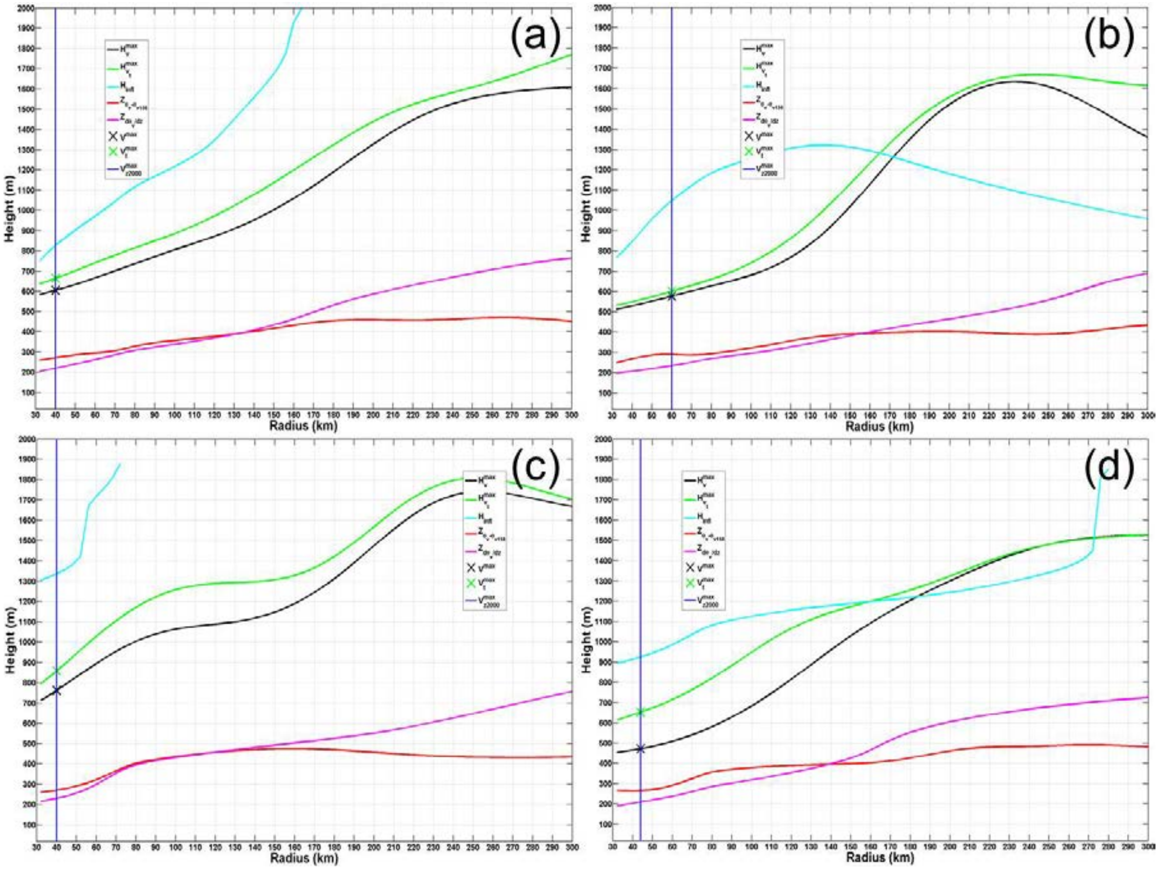

Figure 34. Composite analysis plot of azimuthally averaged hurricane boundary layer heights for the (a) GOM, (b) ECN, (c) CRB, and (d) ECS subregions. Line colors: black – h_{vmax}, green – h_{vtmax}, cyan – h_{infl}, red – θ_v anomaly, magenta – θ_v lapse rate. A green (black) "X" identifies the location of the absolute maximum tangential (total) wind speed. A thick blue line identifies the RMW.

While the GOM and CRB retained the global average of 40 km, the mean RMW for the ECN and ECS subregions were found at r = 60 km and r = 44 km, respectively. These same subregions produced the most reliable estimates for h_{infl}, with solutions in the inner core region that were largely consistent with the other two dynamical definitions.

C. BOUNDARY LAYER HEIGHT SCALES

Box plots provide an additional means of exploring the principal hypotheses of this study. To this end, Figure 35 depicts the radial variability of each boundary layer height definition conditioned by storm semicircle. The distinction between dynamical and thermodynamical definitions is readily apparent, with the second quartiles of the thermodynamical box plots well below the first quartiles of the dynamical box plots. Similarly, the thermodynamical ranges and IQRs were notably smaller than their thermodynamical counterparts.

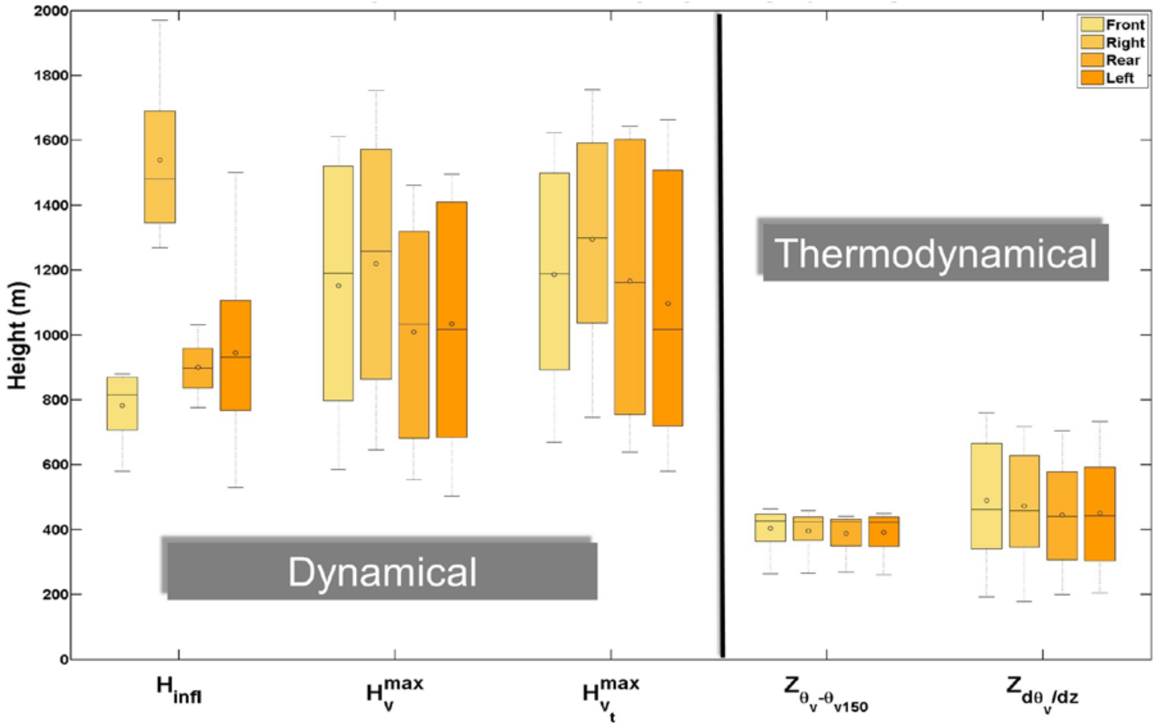

Figure 35. Composite analysis box plot comparisons of five boundary layer height definitions conditioned for azimuthal variability. Storm-relative semicircles are identified by an orange color gradient; color temperature increases in a clockwise sense starting with the front semicircle.

While the mean and median of each dynamical height estimate were highest for the right semicircle quadrants, the differences were small when compared to their corresponding IQRs. Moreover, the range and IQR of h_{vmax} and h_{vtmax} were nearly identical in each semicircle. These characteristics were also evident within each thermodynamical definition, so that each mixed layer depth estimate of boundary layer height exhibited an axisymmetric distribution. The analytical difficulties with inflow layer depth produced inconsistent box blot properties for h_{infl}. In particular, the IQRs of the front and rear semicircles were roughly half the size of the left and right semicircles. Moreover, the mean and median geopotential height of the right semicircle was twice as large as any other portion of the hurricane vortex.

If the results from Figure 35 are organized by quadrants (Figure 36), the variability in boundary layer height becomes clear. The inflow layer depth in the right-rear quadrant is poorly defined for geopotential heights below 2 km.

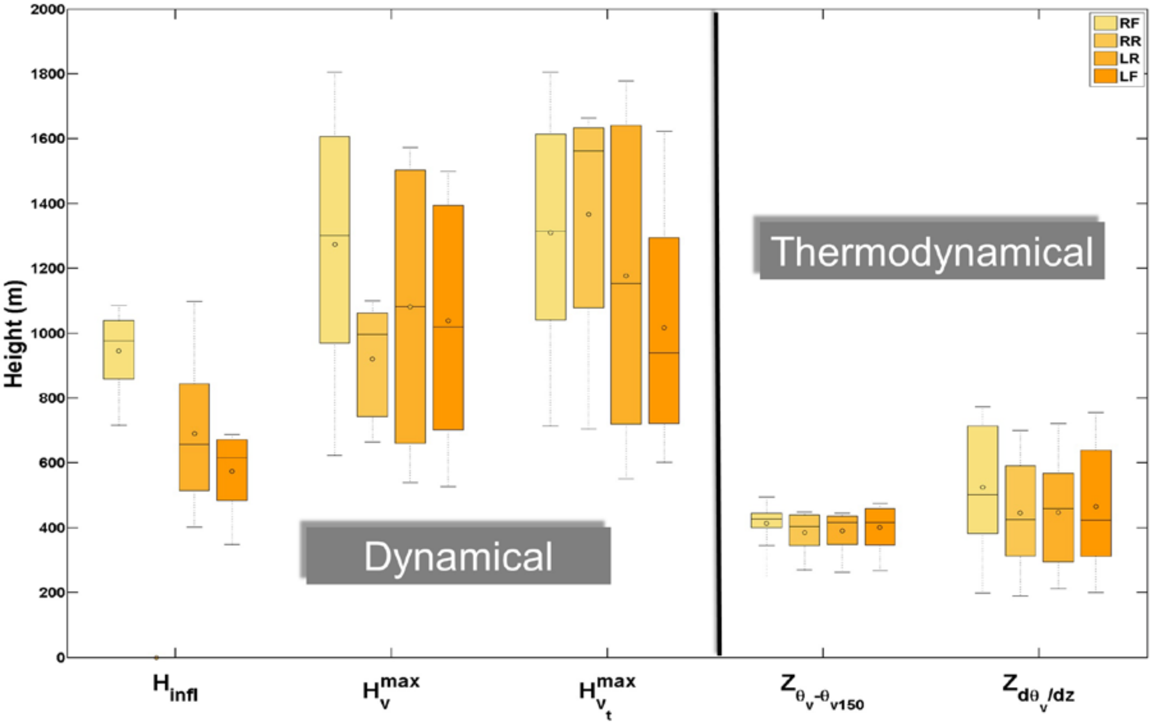

Figure 36. Composite analysis box plot comparisons of five boundary layer height definitions conditioned for azimuthal variability. Storm-relative quadrants are identified by an orange color gradient; color temperature increases clockwise starting with the right-front quadrant.

Thus, a combination of quadrants in the right semicircle produced an anomalous result with questionable physical relevance. The remaining results are consistent with semicircle conditioning in that a notable separation in dynamical and thermodynamical heights exists with distinct radial variability. The inflow layer depth, when defined, produces height estimates with marginal azimuthal dependence.

A similar examination of regional variability (Figure 37) confirms many of the trends identified in the azimuthal conditioning scheme. That is, a clear distinction emerges between the dynamical and thermodynamical heights scales considered by this study. The mean height and IQR for h_{vmax} and h_{vtmax} are significantly larger than the corresponding values generated by estimates of the mixed layer depth. By comparison, the boundary layer heights based on inflow layer depth exhibit mixed results. The radial dispersion of h_{infl} is more consistent with the thermodynamical definitions, while mean geopotential height is commensurate with other dynamical estimates.

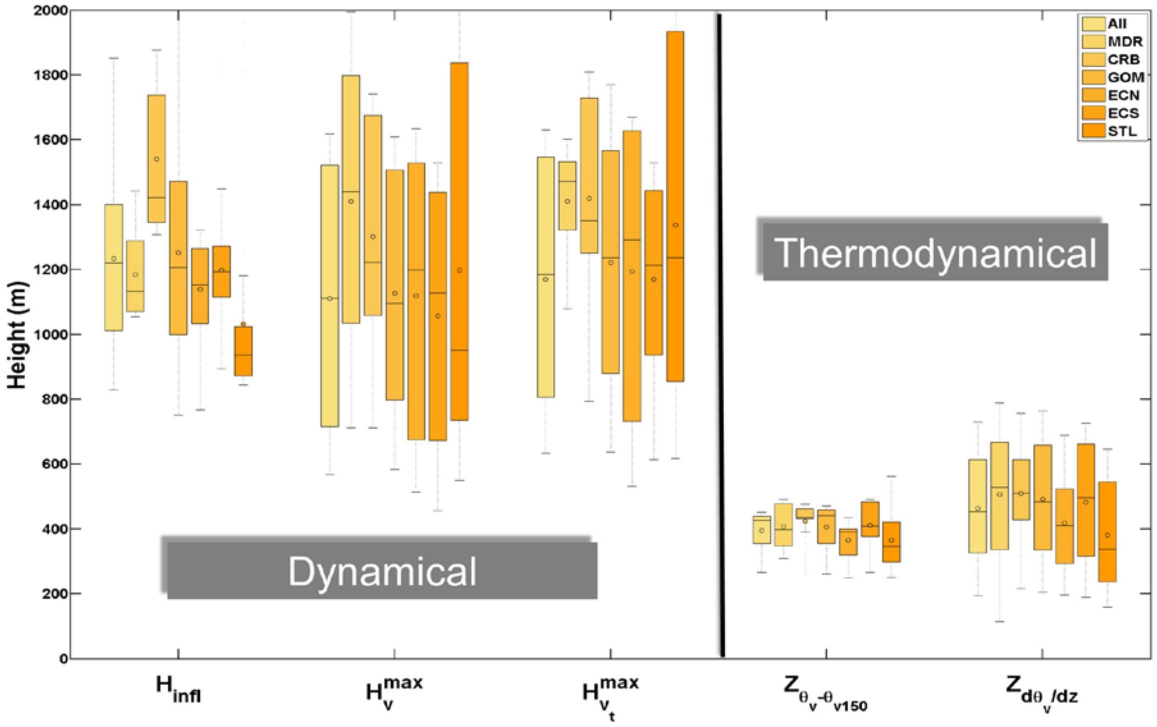

Figure 37. Composite analysis box plot comparisons of five boundary layer height definitions conditioned for regional variability. Subregions are identified by an orange color gradient; the color temperature increases in a clockwise fashion starting with the MDR.

Regardless, the geographic location of a storm did not appear to influence the azimuthally averaged characteristics of the boundary layer height estimates considered by this study. When isolated within their respective groups, each definition demonstrated consistent mean boundary layer geopotential heights and indistinguishable IQRs. Removing the data-sparse MDR and STL regions from consideration, a marginal depression in boundary layer heights was observed for the GOM, ECN, and ECS subregions. While small compared to their respective IQRs, this inclination was nevertheless examined within regional case studies for additional clarity.

D. REGIONAL CASE STUDIES

1. GOM versus ECN

The composite analysis contour plots of relative radial winds depict distinctly stronger near-surface inflow in the right-front and left-front quadrants of the GOM over that of the ECN subregion (Figure 38). The right-front quadrant maximum inflow exceeded 14 m s^{-1}. Moreover, the mean geopotential height of the right-front h_{infl} was higher for the GOM, with both subregions possessing the same characteristic local maximum. The GOM subregion exhibited this maximum near the mean RMW at r = 40 km, while the maximum h_{infl} over the ECN subregion was shifted to the outer core region and near r = 140 km. By contrast, the left-front quadrants for each subregion demonstrated different boundary layer slope characteristics. Specifically, the left-front quadrant of the ECN subregion depicted a monotonically increasing h_{infl} with decreasing radius to the storm center, which is atypical of established boundary layer height variability. The left-front quadrant of the GOM subregion produced a decreasing h_{infl} with decreasing radius in the inner core region, which is consistent with the findings in the right front-quadrants of both subregions.

A brief examination of the height of absolute maximum tangential winds, as identified by the green “X” in each contour plot, revealed the anomalous behavior of the GOM front semicircle. That is, the left-front and right-front quadrants of this subregion suggest that the inflow layer depth is below the corresponding maximum in tangential winds. While convolution smoothing of the h_{infl} and h_{vtmax} contours introduces non-trivial uncertainty, this observation, at the very least, represents a departure from the pattern identified by Z11. Specifically, these findings are identically inconsistent with the maximum tangential wind occurring at a height where the radial inflow has decayed to 25% of its peak near-surface value.

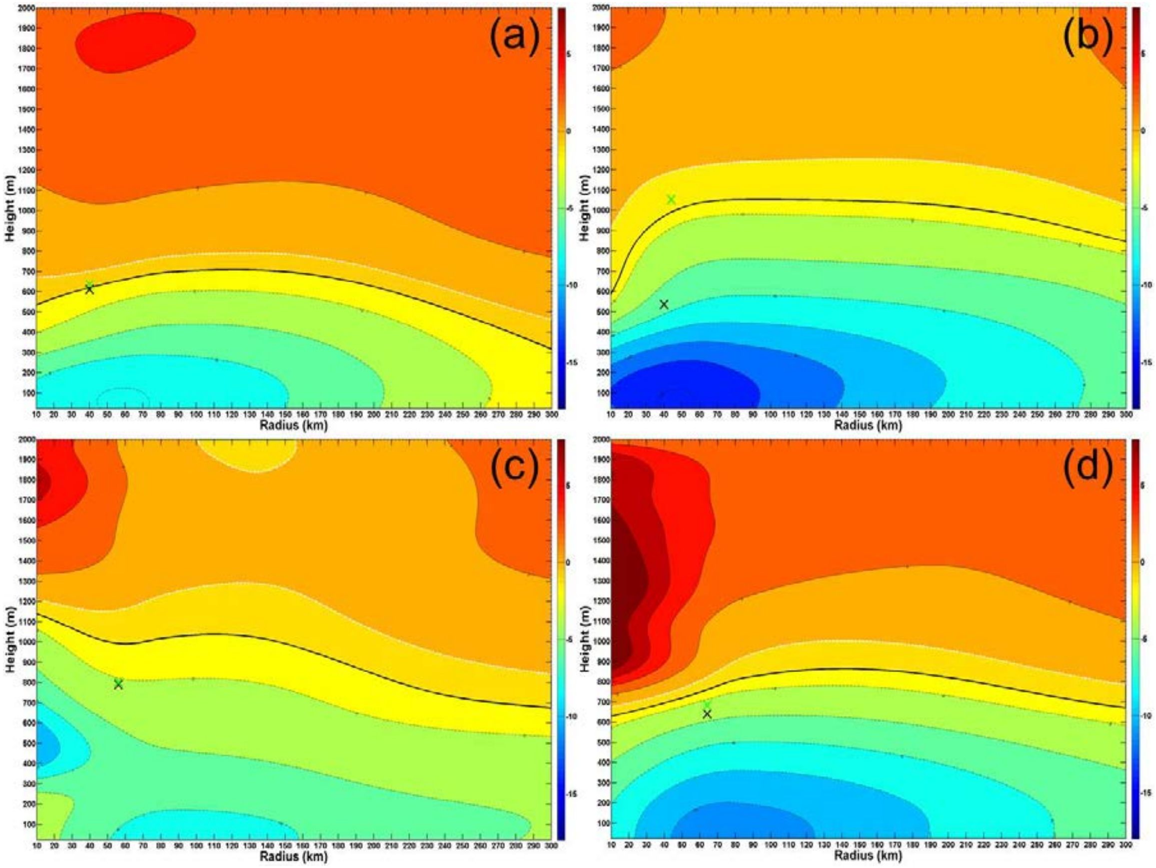

Figure 38. Composite analysis contour plots of the relative radial wind speed in 2 m s^{-1} increments for the (a) GOM left-front, (b) GOM right-front, (c) ECN left-front, and (d) ECN right-front quadrants. Thick black lines represent the height of the inflow layer (h_{infl}) as a function of radius to the storm center. White dashed lines identify the boundaries between areas of inflow and outflow. A green (black) "X" identifies the location of the absolute maximum tangential (total) wind speed.

The azimuthal distribution of radial wind differences between the GOM and ECN subregions is illustrated in Figure 39. Representing the signed difference between the two subregions, it suggests the GOM subregion contains significantly more near-surface inflow in the right semicircle quadrants. Similarly, the ECN subregion contained stronger outflow above the inflow over the right semicircle. Results are more inconclusive for the quadrants in the left semicircle. However, the GOM subregion appeared to contain more boundary layer outflow throughout the left-front quadrant, while this variability was limited to the inner core region for the left-rear quadrant.

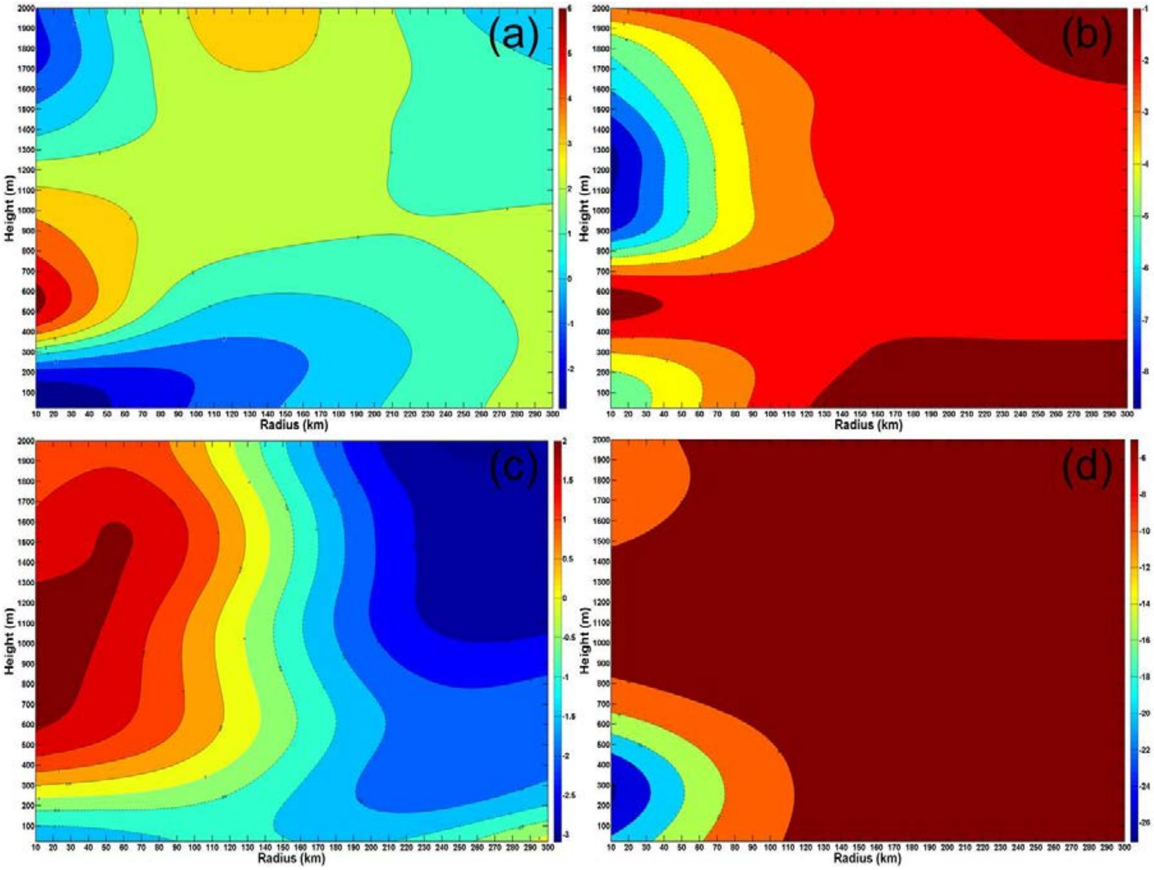

Figure 39. Composite analysis contour plots of the difference between GOM and ECN relative radial wind speeds in 2 m s^{-1} increments for the (a) left-front, (b) right-front, (c) left-rear, and (d) right-rear quadrants. Dashed contours correspond to inflow; solid contours indicate outflow.

The difference between GOM and ECN boundary layer height scales for each quadrant was compared in Figure 40. Ignoring small variations in the differences between these subregions, and also ignoring instances where the inflow layer height was poorly defined, GOM subregion boundary layer heights were typically higher than those of the ECN for the right semicircle and left-rear quadrants. In simple terms, each discrete boundary layer height difference was above the solid black lines more frequently than it was below. The left-front quadrant was incompatible with this trend, where the three dynamical height estimates were higher for the ECN subregion. Moreover, the height differences in the thermodynamical definitions were marginal between the subregions. The composite analysis results implicated the dynamical estimates in the bulk of the observed regional disparities.

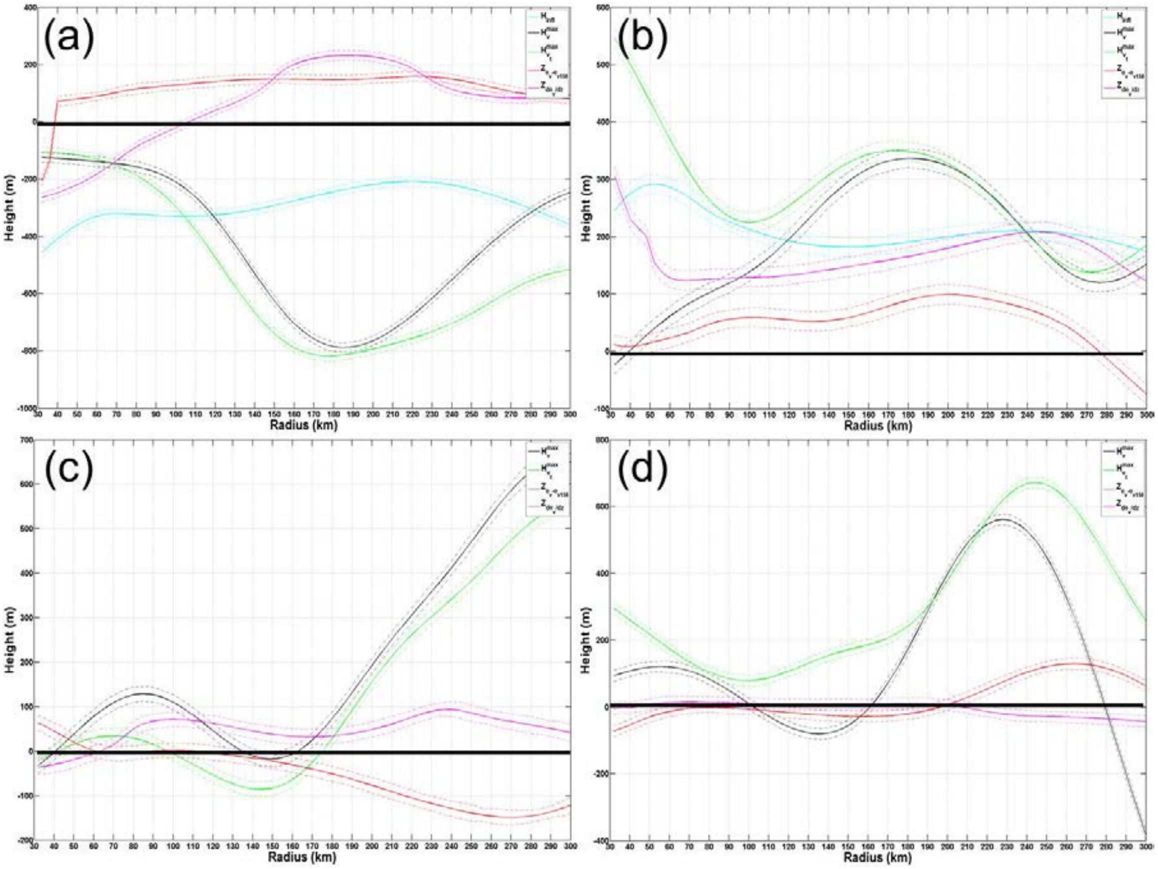

Figure 40. Composite analysis plot of hurricane boundary layer height differences between the GOM and ECN subregions for the (a) left-front, (b) right-front, (c) left-rear, and (d) right-rear quadrants. Line colors: black – h_{vmax}, green – h_{vtmax}, cyan – h_{infl}, red – θ_v anomaly, magenta – θ_v lapse rate. Solid black lines identify the boundaries between positive and negative differences.

2. ECN versus ECS

Duplicating the previous comparison, composite analysis contour plots of relative radial wind show the unique azimuthal characteristics of the ECN and ECS subregions

(Figure 41). The strength of the near-surface inflow is immediately apparent in the right semicircle results, with the ECS and GOM subregions containing similar peak values. The left-front quadrant of the ECN subregion exhibited an increasing h_{infl} with decreasing radius as does the right-front quadrant of the ECS subregion. Conversely, the local maximum in h_{infl} identified in left-front quadrant of the ECS subregion is found in the right-front quadrant of the ECN subregion. Their locations in the radius-height space are distinct, with the former located at a greater radius than the latter, but their general slope characteristics were nevertheless consistent.

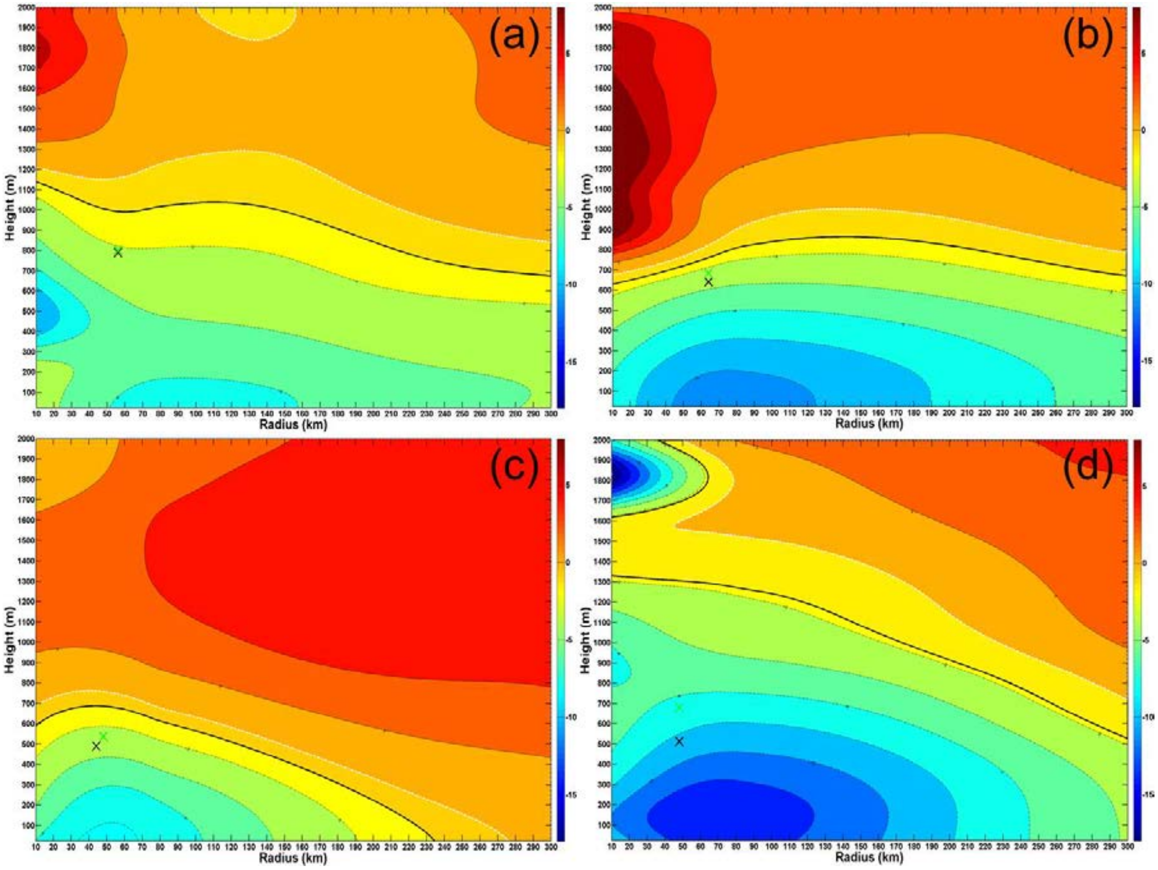

Figure 41. Composite analysis contour plots of the relative radial wind speed in 2 m s^{-1} increments for the (a) ECN left-front, (b) ECN right-front, (c) ECS left-front, and (d) ECS right-front quadrants. Thick black lines represent the height of the inflow layer (h_{infl}) as a function of radius to the storm center. White dashed lines identify the boundaries between areas of inflow and outflow. A green (black) “X” identifies the location of the absolute maximum tangential (total) wind speed.

An examination of the radial wind differences (Figure 42) revealed a neatly divided azimuthal distribution between the subregions. Specifically, the right semicircle differences were generally positive, which suggests that the ECS contains greater near surface inflow and greater boundary layer outflow aloft. Conversely, the left semicircle results were usually negative, which indicates the presence of enhanced near-surface ECN inflow and stronger ECS boundary layer outflow aloft.

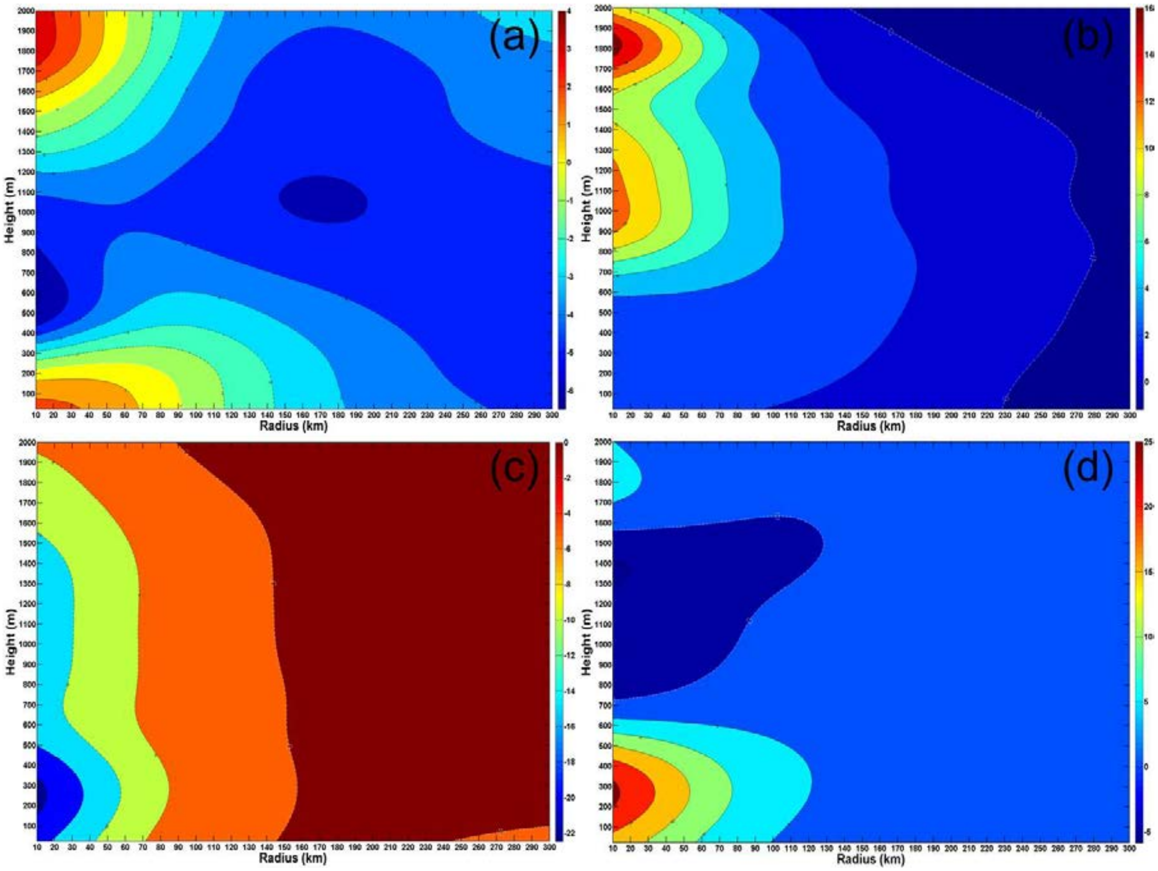

Figure 42. Composite analysis contour plots of the difference between ECN and ECS relative radial wind speeds in 2 m s^{-1} increments for the (a) left-front, (b) right-front, (c) left-rear, and (d) right-rear quadrants. Dashed contours correspond to inflow; solid contours indicate outflow.

Finally, the azimuthal distributions of boundary layer height differences depicted in Figure 43 were irregular and generally inconclusive. As observed in the GOM-ECN comparison, the thermodynamical definitions demonstrated no meaningful azimuthal variability. However, the dynamical definitions of boundary layer height did contain some specific differences. The left semicircle quadrants suggested higher boundary layer heights existed in the ECN subregion, while the right-front quadrant estimates of boundary layer height were typically higher for the ECS subregion. By comparison, the right-rear quadrant demonstrated no net bias for either region. Moreover, inflow layer depths were removed from the rear semicircle results due to anomalous behavior. Where available, the h_{infl} contours were in agreement with their dynamical counterparts.

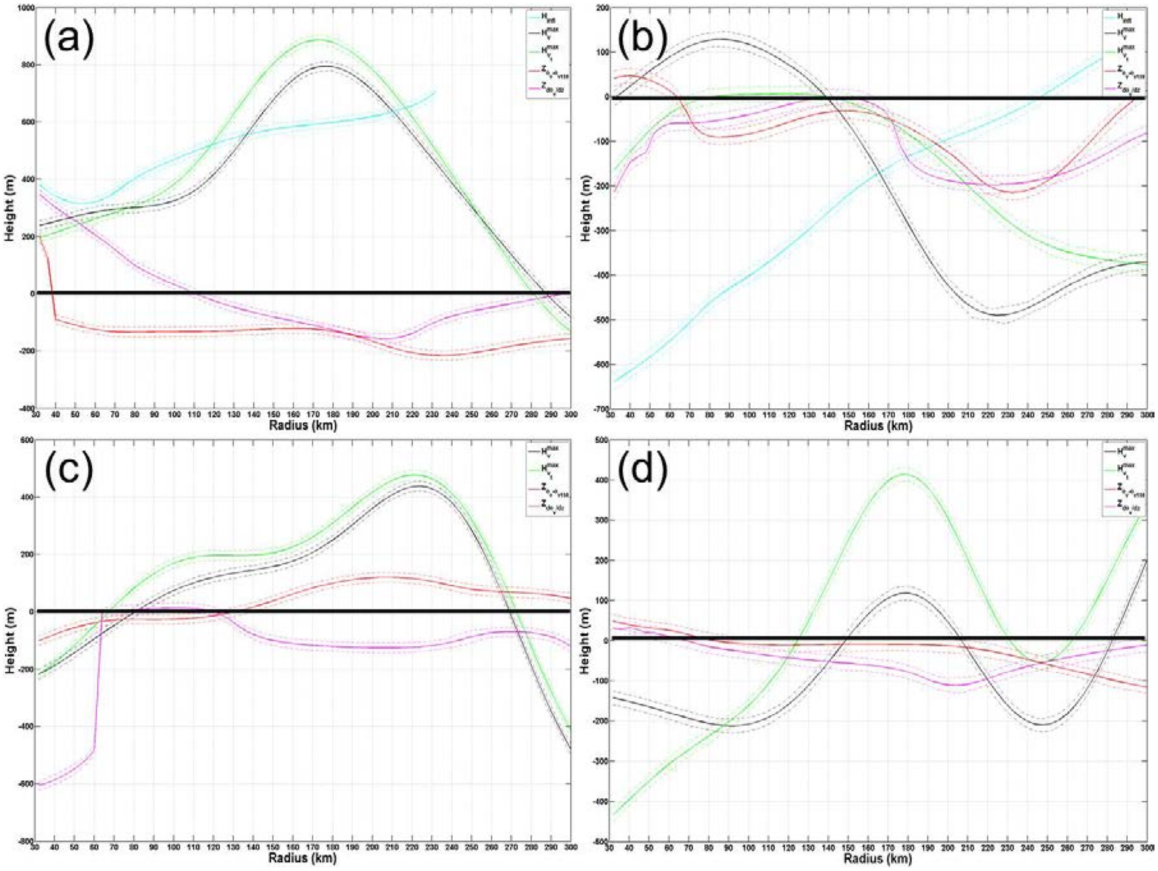

Figure 43. Composite analysis plot of hurricane boundary layer height differences between the ECN and ECS subregions for the (a) left-front, (b) right-front, (c) left-rear, and (d) right-rear quadrants. Line colors: black – h_{vmax}, green – h_{vtmax}, cyan – h_{infl}, red – θ_v anomaly, magenta – θ_v lapse rate. Solid black lines identify the boundaries between positive and negative differences.

V. DISCUSSION

A. SUMMARY AND CONCLUSIONS

The composite analysis findings of Z11 were focused on characteristic variability in competing definitions of hurricane boundary layer height and their corresponding dependence on hurricane intensity. This study extended the Z11 investigation to include a much more comprehensive dataset with an order of magnitude increase in the number of NCAR GPS dropsondes considered, rising from 794 hurricane observations to 6,593 in the final quality controlled data structure. The large dataset used in this study allows examination of boundary layer height variability in different azimuthal directions in the storm-relative coordinate system and in various geographic regions.

Several components of the Z11 analysis were confirmed by this research. The unique signature of a boundary layer jet was found in the new modes of conditioning, where some quadrants and subregions (e.g. the right-front quadrant or ECS subregion) contained core features with greater vertical extent and enhanced wind speeds. More importantly, the consistent bifurcation of dynamical and thermodynamical heights generated a non-trivial distinction between the two classes in estimating the vertical limit of turbulent transport in the hurricane atmosphere. In particular, the thermodynamical methods were found to have characteristically shallow boundary layer heights with distinctly flat slopes with respect to radius. In contrast, the height of the maximum total wind speed was generally found to exhibit the largest radial slopes, while the height of the maximum tangential wind speed was generally found to be at higher heights than the former. Finally, Z11 notes that “defining the boundary layer top as the inflow layer depth presents its own problems, in that real storms may have highly asymmetric inflow layers” (Z11). The non-uniform azimuthal distributions of relative radial winds and ill-behaved inflow layer depths validated this warning. While the front semicircle exhibited estimates of h_{infl} that were analytically tractable, their h_{infl} slopes were often found to be non-monotonic within the hurricane boundary layer. At the very least, the irregular h_{infl} behavior in the rear semicircle affected the physical interpretation of azimuthally averaged composite analysis results.

Some findings in this thesis were altogether new or diverged from the original Z11 study. A modified Rankine vortex with a dimensionless size parameter between $x = 0.4$ and $x = 0.5$ was found to closely match the statistical properties of the vertically averaged tangential wind field. In this way, the composite hurricane is shown to roughly approximate an idealized free vortex in the outer core region and a forced vortex inside of the RMW. Additionally, the clear distinction in boundary layer height estimates between dynamical and thermodynamical methods was found to be coupled with an identical bifurcation in the magnitude of their radial variability. The box plots in Figures 35-37 provide an excellent justification for this claim. While the inflow layer depth was found above the height of the absolute maximum tangential wind speed in azimuthally and regionally averaged results, this relationship did not always hold. In particular, the GOM subregion was noted to favor a reciprocal relationship. Moreover, the height of the absolute maximum tangential wind speed was, at best, only approximated by the height at which radial inflow had decayed to 25% of its peak near-surface value. In some modes of joint conditioning, this analytical relationship failed to match the observed vertical stratification of relative radial winds.

The hypothesis investigating the regional dependence of various estimates of boundary layer height was largely invalidated. That is, azimuthally averaged boundary layer height estimates failed to exhibit any meaningful regional variability. While the radial distributions of GOM, ECN, and ECS boundary layer heights demonstrated marginally shallower median values, these differences were small in comparison to their IQRs and ranges. A closer examination of these subregions revealed non-trivial distinctions in boundary layer properties when azimuthal dependence was superimposed upon the regional variability (e.g., enhanced near-surface GOM inflow for the right semicircle versus corresponding values for the ECN subregion), but no significant response was observed in the attendant boundary layer height estimates.

Results were mixed from the investigation of the second hypothesis that addressed the azimuthal dependence of hurricane boundary layer height estimates. While the thermodynamical definitions exhibited a nearly axisymmetric signature, the inflow layer depth was notably higher in the right-front quadrant. Moreover, h_{vmax} and h_{vtmax}

demonstrated a large, monotonic slope throughout the right-front quadrant of the hurricane boundary layer. By comparison, the right-rear quadrant exhibited an uncharacteristically shallow and radially flat estimate of h_{vmax}. The azimuthally conditioned box plots communicate a similar message, but they also hint at a slight increase in the height of the hurricane boundary layer for the right-front quadrant. When grouped by semicircles, the front and right sectors exhibited marginal, yet non-trivial increases in many of their boundary layer height estimates. The intersection between these two semicircles lies with the right-front quadrant, which further augments the claim that the height of the hurricane boundary layer may be enhanced in this sector.

B. RECOMMENDATIONS FOR FUTURE RESEARCH

While two new modes of data conditioning provided unique perspectives of the original Z11 study, additional comparisons are available. Specifically, western North Pacific typhoons would provide a meaningful contrast to the Atlantic hurricanes considered thus far. In this way, the unique boundary layer characteristics of tropical cyclones active in disparate ocean basins may be realized. Moreover, novel methods of defining the height of the boundary layer could be incorporated. In this regard, D14 provided an extensive summary of options from which new boundary layer height estimates and thresholds may be considered within the composite analysis framework. The inclusion of additional elements from air-sea interaction theory, such as the potential correlation between ocean heat content and boundary layer height, could also benefit research into the characteristics of the hurricane boundary layer. However, such an investigation would require the inclusion of collocated ocean data from airborne expendable bathythermographs (AXBTs).

While Z11 successfully incorporated the RMW into their normalized composite analysis contour plots, this study was unable to accomplish the same. Future efforts would benefit from the inclusion of this information. Finally, the role of uncertainty in the composite analysis technique deserves additional investigation. While this study attempted to quantify the uncertainty of boundary layer height estimates, the combination of bin averages and convolution smoothing may have obscured important statistical properties of the underlying data.

LIST OF REFERENCES

AMS, cited 2014a: Glossary of Meteorology: Bulk Richardson Number. [Available online at http://glossary.ametsoc.org/wiki/Bulk_richardson_number]. Accessed 09 June 2014.

AMS, cited 2014b: Glossary of Meteorology: Logarithmic Velocity Profile. [Available online at http://glossary.ametsoc.org/wiki/Logarithmic_velocity_profile]. Accessed 10 June 2014.

Anthes, R. A., and S. W. Chang, 1978: Response of the hurricane boundary layer to changes of sea surface temperature in a numerical model. *J. Atmos. Sci.*, 35, 1240–1255.

Bryan, G. H., R. Rotunno, 2009: Evaluation of an Analytical Model for the Maximum Intensity of Tropical Cyclones. *J. Atmos. Sci.*, 66, 3042–3060.

Emanuel K. A., 1986: An air-sea interaction theory for tropical cyclones. Part I: Steady-state maintenance. *J. Atmos. Sci.*, 43, 585–604.

Emanuel K. A., 2001: Contribution of tropical cyclones to meridional heat transport by the oceans. *J. Geophys. Res.*, 106, 14771–14781.

EOL, cited 2014: GPS Dropsonde. [Available online at https://www.eol.ucar.edu/content/gps-dropsonde]. Accessed 09 June 2014.

Fefferman, C. L., 2000: Existence and smoothness of the Navier-Stokes equation, Clay Millenium Problems (2000).

Frisius, T., D. Schönemann, and J. Vigh, 2013: The Impact of Gradient Wind Imbalance on Potential Intensity of Tropical Cyclones in an Unbalanced Slab Boundary Layer Model. *J. Atmos. Sci.*, 70, 1874–1890.

Garratt, J. R., 1992: The atmospheric boundary layer. Cambridge University Press, 336 pp.

Hock, T. F., and J. L. Franklin, 1999: The NCAR GPS Dropwindsonde. *Bull. Amer. Meteor. Soc.* 80, No. 3, 407-420.

Holton, J. R., 2004: An Introduction to Dynamic Meteorology, Fourth Edition. Academic Press, 535 pp.

Kepert, J. D., 2010: Deficiencies of Slab Models of the Hurricane Boundary Layer. 29th AMS Conference on Hurricanes and Tropical Meteorology, Tucson, Arizona, May 10 – 14, 2010. 9B3.

Landsea, C., J. Franklin, and J. Beven, 2014: HURDAT2 Format Description. [Available online at http://www.aoml.noaa.gov/hrd/hurdat/newhurdat-format.pdf]. Accessed 09 June 2014.

MathWorks, cited 2014: Smooth Contour Data with Convolution Filter. [Available online at http://www.mathworks.com/help/matlab/creating_plots/smooth-contour-data-with-convolution-filter.html]. Accessed 10 June 2014.

Moeng, C.-H., 1984: A Large Eddy-Simulation Model for the Study of Planetary Boundary Layer Turbulence. *J. Atmos. Sci.*, 41, 2052–2062.

Moss, M. S., and F. J. Merceret, 1976: A note on several low-layer features of Hurricane Eloise. *Mon. Wea. Rev.*, 104, 967-971.

Mueller, K. J., M. DeMaria, J. Knaff, J. P. Kossin, and T. H. Vonder Haar, 2006: Objective Estimation of Tropical Cyclone Wind Structure from Infrared Satellite Data. *Weather and Forecasting*, 21, 990-1005.

Murphy, A. H., 1993: What is a good forecast? An essay on the nature of goodness in weather forecasting. *Weather and Forecasting*, 8, 281-293.

NASA, cited 2003: Eye of Hurricane Isabel, Atlantic Ocean. [Available online at http://eol.jsc.nasa.gov/debrief/Iss007/dynamicFiles/ISS007-E-14745.htm]. Accessed 09 June 2014.

Nolan D. S., J. A. Zhang, and D. P. Stern, 2009a: Evaluation of planetary boundary layer parameterizations in tropical cyclones by comparison of in-situ observations and high-resolution simulations of Hurricane Isabel (2003). Part I: Initialization, maximum winds, and the outer core boundary layer. *Mon. Wea. Rev.*, 137, 3651-3674.

Nolan D. S., J.A. Zhang, and D. P. Stern, 2009b: Evaluation of planetary boundary layer parameterizations in tropical cyclones by comparison of in-situ observations and high-resolution simulations of Hurricane Isabel (2003). Part II: Inner core boundary layer and eyewall structure. *Mon. Wea. Rev.*, 137, 3675-3698.

Ooyama, Katsuyuki, 1969: Numerical Simulation of the Life Cycle of Tropical Cyclones. *J. Atmos. Sci.*, 26, 3–40.

Riehl, H., 1954: Tropical Meteorology. McGraw Hill, 392 pp.

Smith, R. K., and M. T. Montgomery, 2010: Hurricane boundary layer theory. *Q. J. R. Meteorol. Soc.*, 136A, 1665–1670.

Smith, R. K., and G. L. Thomsen, 2010: Dependence of tropical-cyclone intensification on the boundary layer representation in a numerical model. *Q. J. R. Meteorol. Soc.*, 136A, 1671–1685.

Smith, R. K., M. T. Montgomery, and S. Vogl, 2008: A critique of Emanuel's hurricane model and potential intensity theory. *Q. J. R. Meteorol. Soc.*, 134, 551–561.

Smith, R. K., M. T. Montgomery, and S. V. Nguyen, 2009: Tropical cyclone spin-up revisited. *Q. J. R. Meteorol. Soc.*, 135, 1321–1335.

Stull, R. B., 1988: An Introduction to Boundary Layer Meteorology. Kluwer Academics, 666 pp.

Troen, I., and L. Mahrt, 1986: A simple model of the atmospheric boundary layer: Sensitivity to surface evaporation. *Bound.-Layer Meteorol.*, 37, 129-148.

Young, K., J. Wang, and D. Behringer, 2013: Long-Term NOAA Dropsonde Hurricane Archive Quality Assurance Summary. [Available online at ftp://ftp.eol.ucar.edu/pub/temp/projects/dropsondes/Hurricane.Archive/dropsondes/NOAA/readme.NOAA%20Hurricane%20Dropsonde%20Archive-v2.pdf]. Accessed 09 June 2014.

Zeng, X., M.A. Bruke, M. Zhou, C. Fairall, N. A. Bond, and D. H. Lenschow, 2004: Marine atmospheric boundary layer height over the eastern Pacific: Data analysis and model evaluation. *J. Climate*, 17, 4159-4170.

Zhang, J. A., R. F. Rogers, D. S. Nolan, and F. D. Marks, 2011: On the Characteristic Height Scales of the Hurricane Boundary Layer. *Mon. Wea. Rev.*, 139, 2523–2535.

Ziemba, D. A., 2013: Ducting Conditions for Electromagnetic Wave Propagation in Tropical Disturbances from GPS Dropsonde Data. NPS Thesis.

THIS PAGE INTENTIONALLY LEFT BLANK

INITIAL DISTRIBUTION LIST

1. Defense Technical Information Center
   Ft. Belvoir, Virginia

2. Dudley Knox Library
   Naval Postgraduate School
   Monterey, California